ELSEVIER

Review

All-boron aromatic clusters as potential new inorganic ligands and building blocks in chemistry

Anastassia N. Alexandrova [a], Alexander I. Boldyrev [a,*], Hua-Jin Zhai [b,c], Lai-Sheng Wang [b,c,*]

[a] *Department of Chemistry and Biochemistry, Utah State University, Logan, UT 84322-0300, United States*
[b] *Department of Physics, Washington State University, 2710 University Drive, Richland, WA 99354, United States*
[c] *W.R. Wiley Environmental Molecular Sciences Laboratory and Chemical Sciences Division, Pacific Northwest National Laboratory, MS K8-88, P.O. Box 999, Richland, WA 99352, United States*

Contents

Abstract

Small boron clusters as individual species in the gas phase are reviewed. While the family of known boron compounds is rich and diverse, a large body of hitherto unknown chemistry of boron has been recently identified. Free boron clusters have been recently characterized using photoelectron spectroscopy and ab initio calculations, which have established the planar or quasi-planar shapes of small boron clusters for the first time. This has surprised the scientific community, as the chemistry of boron has been diversely featured by three-dimensional structures. The planarity of the species has been further elucidated on the basis of multiple aromaticity, multiple antiaromaticity, and conflicting aromaticity.

Although mostly observed in the gas phase, pure boron clusters are promising molecules for coordination chemistry as potential new ligands and for materials science as new building blocks. The use of pure boron species as novel ligands has commenced, suggesting many new chemistries are ahead of us.

© 2006 Elsevier B.V. All rights reserved.

Keywords: Boron clusters; Multiple aromaticity; Multiple antiaromaticity; Conflicting aromaticity; Photoelectron spectroscopy

1. Introduction

Boron compounds have been known to humankind since ancient times, when it was used to prepare hard glasses and glazes [1]. Nowadays the use of boron compounds ranges from hard materials and semiconductors to antitumor medicines, and its importance cannot be overestimated. Neighboring carbon in the periodic table, boron has one electron less than valence orbitals, and that makes a huge difference in determining the chemistry of boron. Although boron has a rich and diverse chemistry, it differs substantially from that of carbon [1,2].

## 1.1. Boranes and carboranes

Boron compounds played essential roles in advancing chemical bonding models. A few milestones in the history of contemporary boron chemistry should be pointed out. In 1912 Stock reported his pioneering work on boranes [3], which led to the identification of the neutral boron hydrides with formulas B_2H_6, B_4H_{10}, B_5H_9, B_5H_{11}, and B_6H_{10}. These compounds were characterized as toxic, air-, and water-sensitive gases, or volatile liquids. A larger compound, $B_{10}H_{14}$, was isolated as a volatile solid. Although the structures of the boranes were established then, the chemical bonding within them remained unclear, as the stoichiometry of the species contradicted the postulates of valence theory. Even the reason for the rapid dimerization of BH_3 into B_2H_6 was a puzzle. The structure of B_2H_6 with bridging H-atoms was proposed in 1921 by Dilthey [4]. However, it was not considered seriously until the 1940s, when infrared spectroscopy data [5–7] supported the structure. Later, electron diffraction [8] and low-temperature X-ray diffraction [9] also confirmed the bridged structure for the diborane. The chemical bonding in boranes was first considered by Pitzer, who proposed the concept of a "protonated double bond" [10].

Further, Lipscomb and co-workers [11] put forward the concept of three-center two-electron (3c-2e) bonding, which, in the case of the B_2H_6 diborane, consisted of two 3c-2e B–H–B bonds involving the bridging hydrogen atoms. Lipscomb also explained the structure of all known boron hydrides, in which the bridging B–H–B bond appeared to be the key structural unit [9]. In the 3c-2e bonding three atoms supply three orbitals, one on each atom. These atomic orbitals interact to form one bonding and two antibonding orbitals. The two available electrons may thus fill the bonding orbital to form a 3c-2e bond. In the n-atomic species, there are n atomic orbitals, and only $n/3$ bonding molecular orbitals, which can be occupied by $2n/3$ electrons. Thus, the reason for certain boranes to exhibit special stability was elucidated. In principle, Lipscomb's concept of the 3c-2e bond, along with aromaticity, is one of the ways of describing electron deficient bonding, even though aromaticity is more common in chemistry and, in a way, more clear. The work of Lipscomb on the chemical bonding of the boranes eventually led to his winning of the Nobel Prize and opened the gateway to understanding the chemistry of boron.

Allard in 1932 [12], and Pauling and Weinbaum in 1934 [13] showed the existence of regular octahedra of boron atoms in several metal hexaborides of the general formula MB_6. These early works represented the first experimental demonstration of closed boron polyhedra in a chemical structure. A subsequent related work by Longuet-Higgins and Roberts [14] used molecular orbital theory to show that the $[B_6]^{2-}$ unit has a closed-shell electronic arrangement of high stability. Longuet-Higgins and Roberts [15] also used a similar approach to study the B_{12} icosahedron, a dominant structural unit of various allotropes of boron [16]. Their work indicated that the B_{12} icosahedron has 13 skeletal bonding orbitals and 12 outward pointing external orbitals. They concluded that a borane, $B_{12}H_{12}$, would be stable only as a dianion, $B_{12}H_{12}^{2-}$, as well as a series of stable cage-like borane dianions of the general formula, $B_nH_n^{2-}$. The conclusion was supported by experimental data provided by Hawthorne and Pitochelli, who synthesized salts of the borane anion, $B_{12}H_{12}^{2-}$ [17,18]. From X-ray diffraction experiments, the structure of the $B_{12}H_{12}^{2-}$ anion was indeed shown to be icosahedral [19] and another $B_{10}H_{10}^{2-}$ anion was shown to be a bicapped square antiprism [20]. Further experiments [21–23] indicated the existence of other deltahedral boranes, $B_{11}H_{11}^{2-}$, $B_9H_9^{2-}$, $B_8H_8^{2-}$, $B_7H_7^{2-}$, and $B_6H_6^{2-}$.

Different rules were developed for the number of atoms, bonds, electrons, and orbitals in stable boranes [24–28]. Dixon et al. made the first attempt to describe boranes in terms of resonance of Kekule-type structures with alternating 2c-2e and 3c-2e bonds [29]. In 1971 Williams [30] recognized the *closo-*, *nido-*, and *arachno-*structural motifs in the chemistry of deltahedral boranes. The most spherical deltahedra have a formula B_nH_{n+2} (or $B_nH_n^{2-}$). The loss of a vertex from this *closo-*form results in the B_nH_{n+4} ($B_nH_{n+2}^{2-}$) *nido-*structure. The *arachno-*structure, B_nH_{n+6} ($B_nH_{n+4}^{2-}$), can be formed by the removal of yet another vertex from the deltahedron. Wade [31] recognized that this structural relationship could be associated with the number of skeletal electrons in a borane. Namely, he understood that *closo-*, and the *nido-* and *arachno-*shapes, have the same number of skeletal electrons: $2n+2$. These species have the same number of molecular orbitals belonging to the boron skeleton: *closo-*boranes have to have $n+1$ MOs, *nido-*boranes have to have $n+2$ MOs, and *arachno-*boranes have to have $n+3$ MOs. This set of rules is known as Wade's rules for boranes and carboranes. Gellespie et al. also proposed another scheme, in which skeletal electron pairs ($2n$ electrons) remained localized on each vertex, whereas two electrons participated in the delocalized bonding over the spherically symmetric polyhedron [32]. Furthermore, the relative stabilities of deltahedral boranes form a series [33]:

$$B_{12}H_{12}^{2-} > B_{10}H_{10}^{2-} > B_{11}H_{11}^{2-}$$
$$> B_9H_9^{2-} \sim B_8H_8^{2-} \sim B_6H_6^{2-} > B_7H_7^{2-}$$
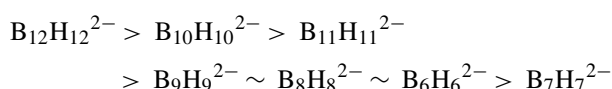
In 1959 Lipscomb et al. [34] proposed the term "superaromaticity" to explain the 3D aromaticity of $B_{12}H_{12}^{2-}$. Chen and King recently reviewed [35] the introduction of 3D aromaticity in chemistry. Explicitly, the idea of aromaticity of deltahedral boranes was put forward by Aihara [36], and by King and Rouvray [37] in 1978. Carboranes of the formula $C_2B_{n-2}H_n$ also exhibit deltahedral topology, and the chemical bonding
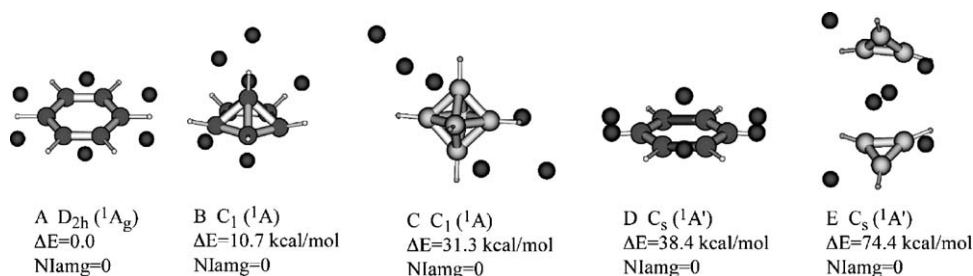
Fig. 1. (A–E) Lowest-energy isomers of the $Li_6B_6H_6$ salt molecule at the B3LYP/6-311++G** level of theory. (Reprinted with permission from Ref. [41]. Copyright 2004 American Chemical Society.)

within them can be described in the same manner [38]. The only difference in the borane-carborane-electronic relationship is that $C_2B_3H_5$, being an electronic analog of $B_5H_5^{2-}$, is a known compound, while $B_5H_5^{2-}$ itself has not been synthesized. The three-dimensional aromaticity in boranes, $B_nH_n^{2-}$, closo-monocarborane anions, $CB_{n-1}H_n^-$, and closo-dicarboranes, $C_2B_{n-2}H_n$ was also computationally studied by Schleyer and Najafian [39], who used the NICS index values as criteria of aromaticity. The authors showed the general trend in such systems: the stability increases with increasing verteces from 5 to 12. The comparison of the chemistry of boron and carbon on the example of boron and carbon hydrides was also discussed by Jemmis and Jayasree [40].

In 2003, Boldyrev and co-workers theoretically predicted the new family of planar aromatic highly charged boranes, such as $B_6H_6^{6-}$ stabilized by six Li^+ cations surrounding the species (structure A, Fig. 1) [41].

Importantly, the planar B_6-fragment has been previously known to be the building block of the MgB_2 solid, which is a recently discovered high-temperature superconductor [42]. An extended analysis of the chemical bonding in the lowest energy

planar and nonplanar isomers involving $B_6H_6^{6-}$ has been performed [41b]. Salts like $Li_6B_6H_6$ with the $B_6H_6^{6-}$ benzene-like analog are still a theoretical prediction, but Fehlner and co-workers [43] recently reported synthesis and crystal structures of remarkable triple-decker $(Cp^*ReH_2)B_5Cl_5$ and $(Cp^*)_2B_6H_4Cl_2$ compounds containing planar B_5Cl_5 and $B_6H_4Cl_2$ structural fragments, respectively (Fig. 2).

It is believed that the planar B_5Cl_5 and $B_6H_4Cl_2$ structural fragments in Fehlner's compounds acquire six electrons from the Re atoms formally and thus become six π-electron aromatic compounds similar to the predicted $B_5H_5^{6-}$ and $B_6H_6^{6-}$ building blocks in the $Li_6B_5H_5$ and $Li_6B_6H_6$ salt molecules.

Beyond boranes and carboranes a very rich family of metallocarboranes has been synthesized and characterized [1,2,38,43–47]. One of the exciting new applications of these species was a demonstration of rotary motion of a carborane cage ligand (7,8-dicarbollide) around a nickel axle controlled by electrical or light energy, thus moving us closer to inorganic nanomachines [45]. Boron atoms can also be incorporated into transition metal clusters [44–47] further extending the rich boron chemistry.
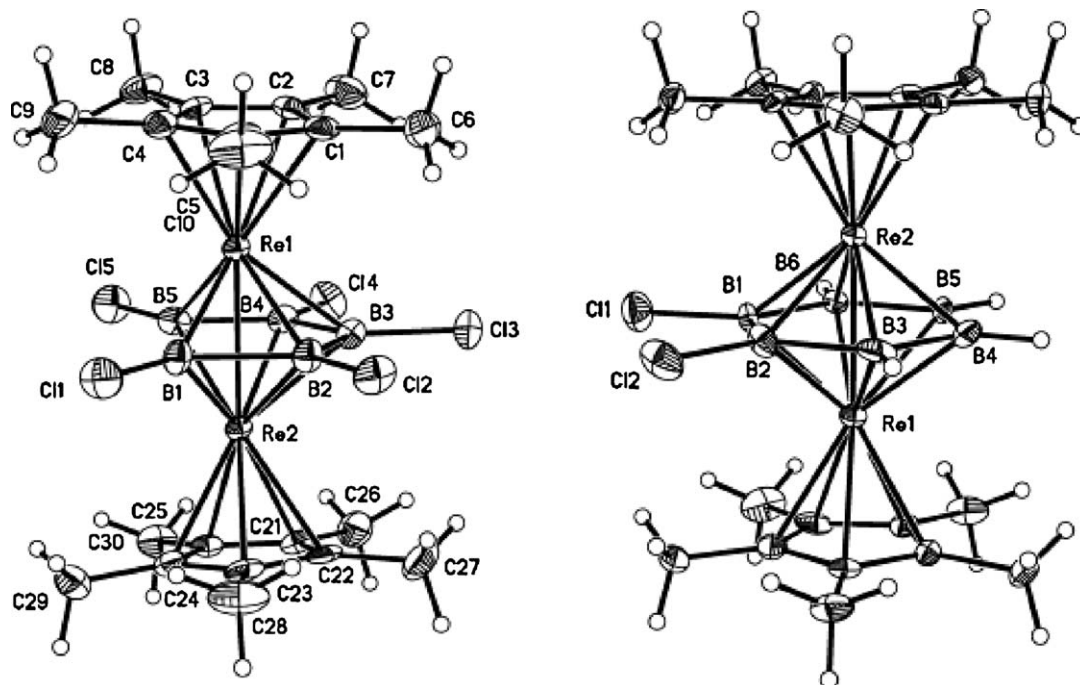
Fig. 2. Molecular structures of: $(Cp^*ReH)_2B_5Cl_5$ and $(Cp^*Re)_2B_6H_4Cl_2$. (Reprinted with permission from Ref. [43a]. Copyright 2004 American Chemical Society.)

1.2. Bare boron clusters

Experimental studies of bare boron clusters have been surprisingly limited despite its proximity to carbon in the periodic table and the extensive research effort on carbon clusters and the fullerenes ([48–52] and references therein). Until very recently the only experimental studies on boron clusters were carried out by Anderson and co-workers in the late 1980s [53–55]. These authors produced boron cluster cations using laser vaporization and studied their chemical reactivity and fragmentation properties [53–59]. Their observation of the prominent B_{13}^+ peak in mass spectra stimulated further computational efforts [60–64]. In 1992, La Placa et al. reported a mass spectrum of bare boron clusters consisting of 2–52 atoms, generated by laser vaporization of a boron nitride target in an effort to produce BN clusters [65]. Little information regarding the structural and electronic properties of boron clusters can be drawn from the mass-spectrometry-based studies. And there have been no spectroscopic studies until very recently.

Starting from 2001, we have conducted extensive photoelectron spectroscopy (PES) studies on a series of boron cluster anions, B_n^- ($n = 3$–20), which were combined with state-of-the-art computational studies to elucidate the structural and electronic properties and chemical bonding in the species [66–72]. These works established for the first time experimentally planarity or quasi-planarity in small boron clusters for as large as 20 atoms. Among our findings are the observation and characterization of the hepta- and octa-coordinated pure boron molecular wheels in B_8 and B_9 [70], the observation of an unusually large HOMO–LUMO gap in B_{12} [71], and the discovery that the planarity or quasi-planarity of boron clusters can be explained on the basis of multiple σ- and π-aromaticity, multiple σ- and π-antiaromaticity, and conflicting aromaticity (simultaneous presence of σ-aromaticity and π-antiaromaticity or σ-antiaromaticity and π-aromaticity) [66–72]. We also found that the π-aromaticity in small boron clusters up to $n = 15$ seems to follow the Hückel's rules, analogous to hydrocarbons [71]. We showed that the B_{20} neutral cluster appears to possess a ring-like 3D ground state geometry although both planar and 3D structures are nearly isoenergetic for the B_{20}^- anion [72]. The B_{20} neutral therefore represents the planar-to-tubular transition in small boron clusters and may be viewed as the embryo of the thinnest single-walled boron nanotubes with a diameter as small as 5.2 Å [72]. Very recently, several other experimental efforts have also appeared on boron clusters [73–77].

In spite of the enormous variety of boron chemical compounds and their great influence on developing modern chemical bonding theory, bare boron clusters as ligands in chemical compounds are still absent. Given the fact that our recent spectroscopic and theoretical studies have shown that isolated boron clusters have planar geometries and exhibit aromatic and antiaromatic electronic properties analogous to hydrocarbons, it is believed that bare boron clusters could potentially be new ligands or building blocks of new solids. It is worth mentioning that a planar aromatic cyclopentadien anion $C_5H_5^-$ is one of the most common ligands in coordination chemistry. In this review we summarize theoretical and spectroscopic studies of isolated all-boron clusters with the hope that the latest experimental and theoretical understanding may stimulate further investigations leading to novel coordination compounds containing the planar all-boron clusters as ligands or new building blocks.

2. Methodology

2.1. Theoretical methods

One of the major challenges in any cluster theoretical study is to find reliably the global minimum structure. Different theoretical studies sometimes predict different "global minimum" structures because of human bias. A number of methods have been developed to search for global minimum structures, which are designed to exclude human bias, such as the Car–Parrinello method, molecular dynamics methods with density functional theory for energy calculations, Monte Carlo annealing methods, and genetic algorithms for global minimum searches. We recently developed a new genetic algorithm method for the search for global minima, called ab initio gradient embedded genetic algorithm (GEGA). The GEGA program was written by Alexandrova and described in details in Refs. [78,79]. The hybrid method, known as B3LYP [80–82], with relatively small basis set, 3-21G, is usually employed throughout the execution of the GEGA. For large clusters, we also use the semiempirical PM3 method.

Briefly, within the GEGA procedure, the initial geometries of individuals (structures) in a population (set of structures) are randomly generated and further optimized to the nearest local minima on the potential energy surface, using the Gaussian 03 package [83]. If a saddle point is encountered the normal mode of the first imaginary frequency is followed until a local minimum is found. The population, composed of the thus selected good individuals (structures with the lowest energies), undergoes breeding and mutations. During the "mating process" some of the geometric features of good individuals in the population ("parents") are combined and passed to new individuals ("children"). Parents are local minimum structures obtained either during the initial or subsequent iterations. Children are new structures made out of two parent structures. Probabilities to be bred (to produce child structures) are assigned to parents according to the best-fit criterion (i.e., the lowest energy). Based on the probabilities, couples of parents are randomly selected. The geometries of the parents are cut by a random cutting plane (*XY*, *XZ*, or *YZ*), and the thus obtained halves ("genes") are then recombined either in a simple or in a head-to-tail manner to form a "child" (a new structure). The number of atoms in the newly generated geometry is checked, and the new structure is optimized to the nearest local minimum.

Fig. 3A shows a typical breeding procedure using the B_9^- cluster as an example. In this case, the YZ plane is chosen as the cutting plane and recombination of the halves occurs in a simple manner, i.e., the part of geometry of parent structure 1 taken from the left of the cutting plane is recombined with the part of geometry of parent structure 2 taken from the right of the cutting plane. The number of atoms in the newly generated geometry is checked, and the child structure is optimized to the nearest local
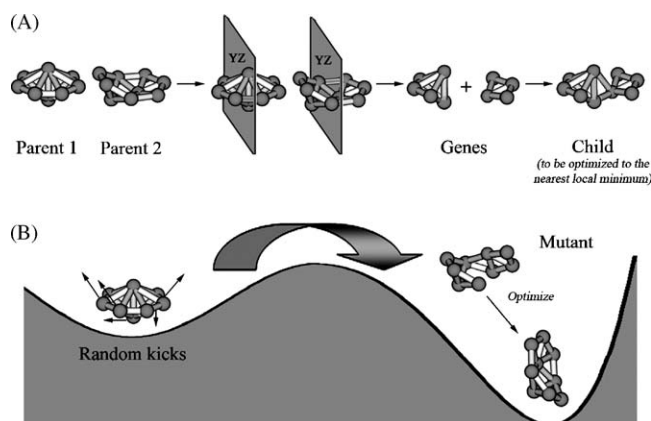
Fig. 3. Illustration of the GEGA procedure. (A) Breeding, when *XY* plane is randomly chosen, geometries of two selected parents are cut by *XY*, and parts of parents are recombined in a simple manner; the obtained child is then optimized to the nearest minimum. (B) Mutations, when the random number of kicks is introduced to distort the structure strongly enough to cross the barrier on the potential energy surface, and the obtained mutant is then optimized to the local minimum.

minimum. If the number of atoms is incorrect, the cutting plane is shifted so that the child structure has the correct number of atoms. After the number of individuals in the population is doubled within the breeding process, the best-fit group is selected and convergence of the algorithm is checked. The GEGA is considered converged if the current lowest energy species (global minimum or at least very stable local minimum) remains for 20 iterations. If the convergence is not yet met, the highest energy species in the population undergo mutations. The mutation rate is set to 33.33%. Mutations are shifts of random atoms of a species in random directions, with the purpose of changing the initial geometry so as to push the structure out of the current local minimum to another well on the potential energy surface (Fig. 3B). Mutants (structures obtained from mutations) are optimized to the nearest local minima. After that the algorithm proceeds with the new cycle of breeding. All low-lying isomers are detected and stored throughout the execution and they are reported to the user at the end of the run. A few runs of GEGA are done on the system in order to confirm the found global minimum structure.

The geometry and vibrational frequencies of the thus identified global minimum, as well as low-lying isomers, are further refined at higher levels of theory. The B3LYP and the coupled-cluster CCSD(T) [84–86] methods with the polarized split-valence basis sets (6-311+G*) [87–89] are usually used for this purpose. Final relative energies for the few lowest structures are calculated at the CCSD(T)/6-311+G(2df) level of theory using the CCSD(T)/6-311+G* geometry. We also run calculations for the global minimum structure at the CASSCF(*X,Y*)/6-311+G* [90,91] (*X* is a number of active electrons and *Y* is a number of active orbitals) level of theory, in order to test the applicability of theoretical methods such as MPn, CCSD(T), and others which are based on the one-electron approximation.

The next step is to calculate the ab initio vertical detachment energies (VDEs), which will facilitate comparison with the experimental PES data. For small systems (three to nine atoms) we use three levels of theory for calculating the VDEs: U(R)CCSD(T)/6-311+G(2df), the outer valence Green Function method (OVGF/6-311+G(2df)) [92–95] at the CCSD(T)/6-311+G* geometries, as well as the time-dependent DFT method [96,97] (TD-B3LYP/6-311+G(2df)) at the B3LYP/6-311+G* geometries. Core electrons were frozen in treating the electron correlation at the CCSD(T) and OVGF levels of theory. For the large boron clusters (>9 atoms), we used primarily the TD-B3LYP/6-311+G* level of theory to calculate the VDEs.

Natural Bond Order (NBO) analysis [98] was employed to examine the detailed chemical bonding. Molecular orbitals (MOs) were calculated at the HF/6-311+G* level of theory. B3LYP, HF, and CCSD(T) calculations were performed using Gaussian 2003 and NWChem [99] programs. Molecular orbitals pictures were made using the MOLDEN 3.4 program [100].

2.2. Photoelectron spectroscopy

The photoelectron spectroscopic studies were carried out using a magnetic-bottle time-of-flight PES apparatus equipped with a laser vaporization supersonic cluster source [101,102]. Details of this apparatus have been reported elsewhere, and Fig. 4 shows a schematic view of it.

The B$_n^-$ cluster anions were produced by laser vaporization of an isotopically enriched ^{10}B disk target in the presence of a helium carrier gas. The cluster anions were mass analyzed using a time-of-flight mass spectrometer and the cluster of interest was mass selected and decelerated before being photodetached. A variety of detachment laser photon energies have been used in the current experiments (532 nm, 355 nm, 266 nm, and 193 nm). Photoemitted electrons are collected by the magnetic-bottle at nearly 100% efficiency and analyzed in a 3.5 m long electron time-of-flight tube. The photoelectron time-of-flight spectra are calibrated using the known spectra of Rh$^-$ or Au$^-$ and converted to kinetic energy (KE) spectra. The reported binding energy (BE) spectra are obtained by subtracting the KE spectra from the photon energy ($h\nu$) using Einstein's photoelectric equation: $BE = h\nu - KE$. High photon energy spectra are partic-
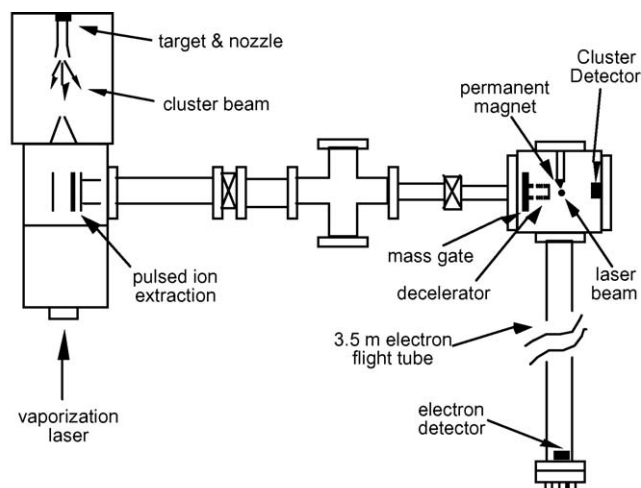

Fig. 4. Schematic view of the laser vaporization magnetic-bottled time-of-flight photoelectron spectroscopy apparatus.

ularly important because they reveal more electronic transitions, which are essential to facilitate comparisons with theoretical predictions. Low photon energies in general yield better-resolved spectra for the ground state transitions, allowing more accurate determination of adiabatic detachment energies (ADEs) of the neutral species and vibrational resolution in favorable cases. The resolution of our apparatus is $\Delta KE/KE \sim 2.5\%$, i.e., ~ 25 meV for 1 eV electrons.

It should be pointed out that although it was not difficult to observe mass spectra with a wide size range of B_n^- clusters by laser vaporization, it turned out to be rather challenging to obtain high quality PES data, primarily due to the low photodetachment cross-sections of these light clusters and the difficulty obtaining cold cluster anions. The key to the current progress was the use of a large waiting-room nozzle, which could more efficiently cool cluster anions [103–105]. The temperature effects were further controlled by tuning the firing timing of the vaporization laser relative to the carrier gas and selecting clusters that have a longer residence time in the nozzle for photodetachment. These efforts have allowed us to obtain well-resolved PES data for B_n^- clusters at different photodetachment energies.

As an example, Fig. 5 shows the dramatic temperature effects observed in the B_{20}^- species at three different detachment photon energies. Clearly, only the "cold" spectra (top panel) yielded the rich and well-resolved PES features, which represent the electronic fingerprint of the underlying clusters. As many as nine definitive spectral features (X–H) were readily resolved in the cold spectrum of B_{20}^- at 193 nm, which were otherwise smeared out in the "hot" spectra even under the same instrumental resolution. The well-defined and well-resolved PES spectra have been used to compare with theoretical calculations, allowing the structural and electronic properties, isomers, and chemical

bonding of small boron clusters to be determined and understood [66–72].

3. Pure-boron clusters

3.1. The diatomic B_2 molecule

The diatomic B_2 molecule provides the first example of unusual chemical bonding in boron species. It is known [106,107] that B_2 has a $^3\Sigma_g^-$ ground electronic state with the $1\sigma_g^2 1\sigma_u^2 1\pi_u^2 2\sigma_g^0$ electronic configuration. This electronic configuration contradicts the conventional chemical bonding picture, because the $1\pi_u$ bonding orbital is occupied before the $2\sigma_g$ bonding orbital is occupied. The first two σ-MOs, $1\sigma_g^2$ and $1\sigma_u^2$, are pairs of bonding and antibonding orbitals formed primarily by the 2s-AOs (with rather small s–p hybridization) and do not contribute to bonding significantly. Thus, most of the ~ 70 kcal/mol bonding energy in B_2 comes primarily from chemical bonding of the $1\pi_u^2$ orbital. Earlier occupation of the $1\pi_u$-MO is inconsistent with the general conception of how chemical bonding should occur in molecules. According to the conventional chemical bond model, a covalent bond is formed when a portion of an atomic orbital of one atom overlaps a portion of an atomic orbital of another atom. In a σ-bond, an orbital overlap occurs along the axis joining two nuclei. In a π-bond an orbital overlap is formed by parallel p-orbitals. Because of the lesser degree of the orbital overlaps forming π-bond, compared with those forming σ-orbitals, π-bonds are generally weaker than σ-bonds, and, therefore, σ-orbitals should be occupied before π-orbitals. The conventional chemical bonding model was initially developed for organic molecules, where this prediction holds rather well. However, for electropositive and electron deficient
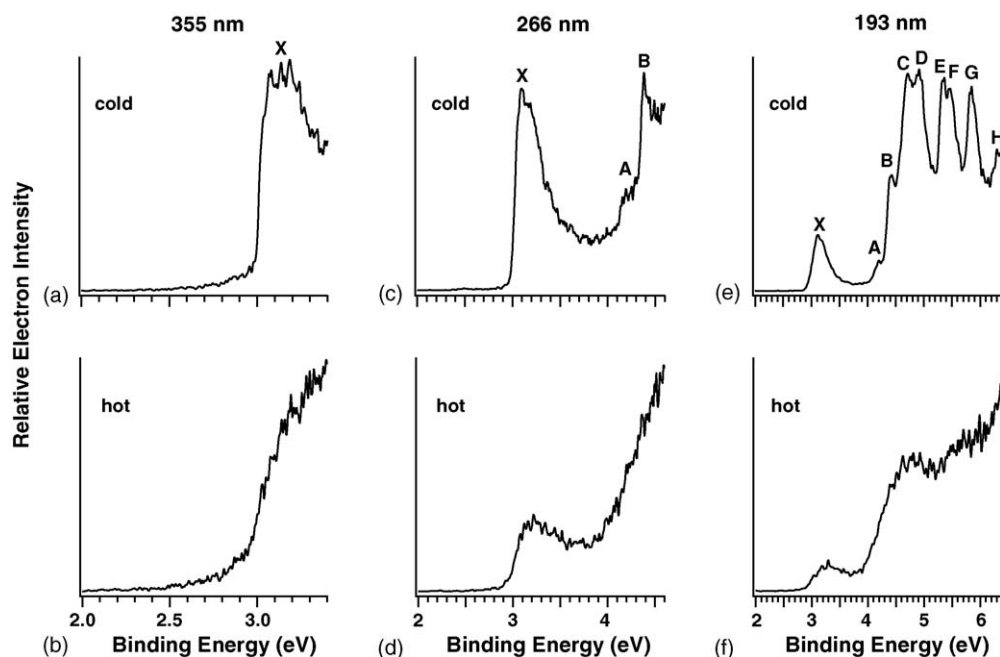
Fig. 5. Photoelectron spectra of B_{20}^- at different source conditions to demonstrate the significant temperature effects on the photoelectron spectra. Top panel, cold clusters; bottom panel, hot clusters. Note that hot clusters result in broad spectra, smearing out the spectral features even under high instrumental resolution. (a, c, and e) Cold and (b, d, and f) hot.

atoms, such as B, it does not work well, not only for the diatomic B_2 molecule, but also for larger clusters, as we will show below.

Low-lying excited states for B_2, B_2^+, B_2^{2+}, and B_2^- from Bruna and Wright [108] are summarized in Fig. 6. B_2^+ is shown to have conventional bonding with the ground electronic state $^2\Sigma_g^+$ ($1\sigma_g^2 1\sigma_u^2 2\sigma_g^1 1\pi_u^0$). However, one can see that the $2^1\Sigma_g^+$ state of B_2 with the $1\sigma_g^2 1\sigma_u^2 2\sigma_g^2 1\pi_u^0$ electronic configuration is about 1.46 eV higher than the $^3\Sigma_g^-$ ground state. We believe that the reason why B_2 and other diatomic molecules composed of electropositive atoms have unconventional ground electronic
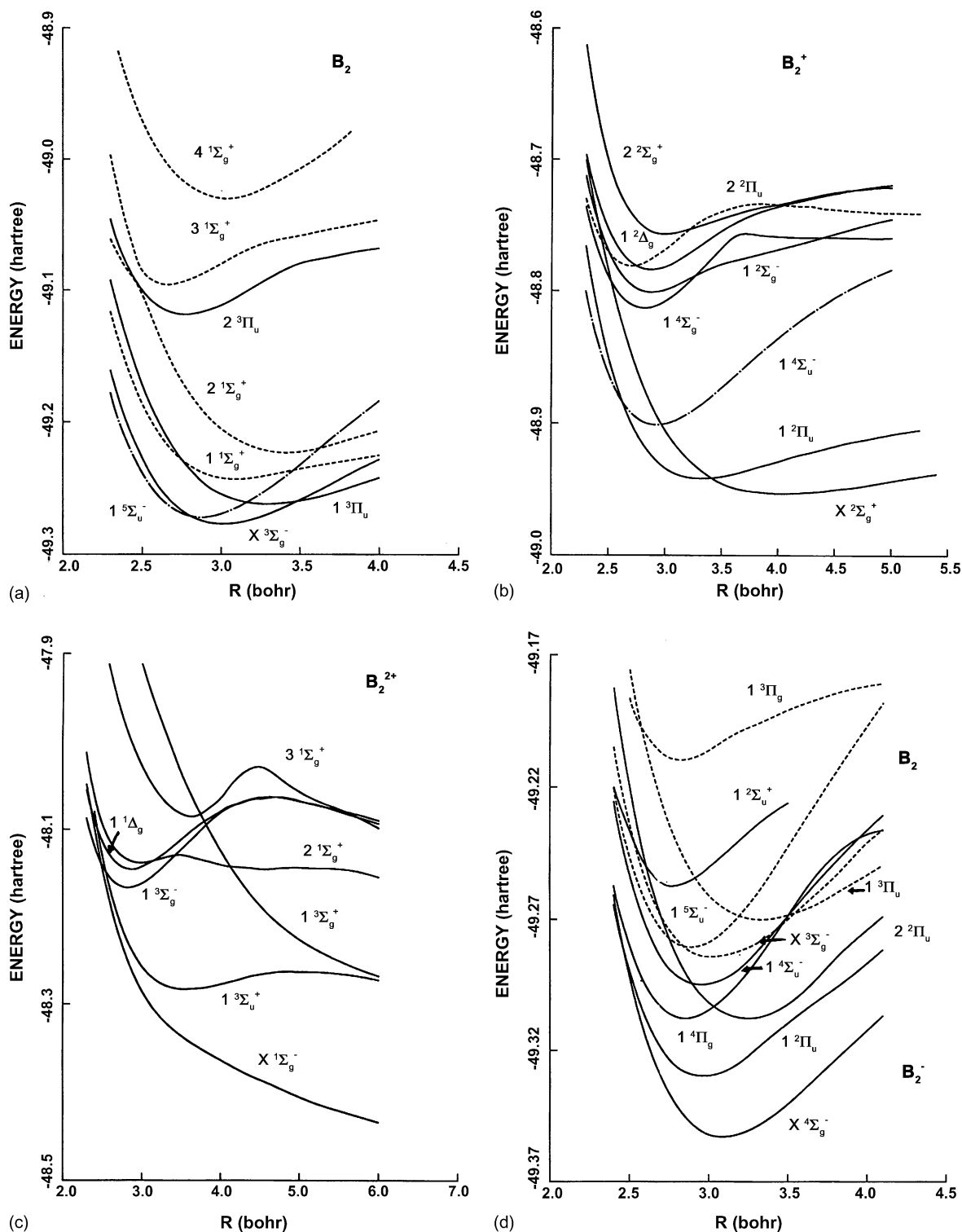
Fig. 6. Low-lying states of: (a) B_2, (b) B_2^+, (c) B_2^{2+}, and (d) B_2^-. (Reprinted with permission from Ref. [108]. Copyright 1990 Elsevier.)

Table 1
Molecular properties of the B_3 (D_{3h}, $^2A_1'$) cluster

	B3LYP/6-311+G*[a]	UCCSD(T)/6-311+G*[a,b]	CASSCF/DZP[c]	CASSCF-MRCISD/aug-cc-pvTZ[d]	Experiment
E_{total} (a.u.)	−74.298272	−74.065078	−73.906715	[e]	
R_e(B–B) (Å)	1.548	1.586	1.587	1.5706	1.60377(106)[f]
ω_1(a$_1'$) (cm^{-1})	1223	1165	1214	[e]	1020(50)[a]
ω_2(e$'$) (cm^{-1})	934	871	869	[e]	

[a] Ref. [66].

[b] E_{total} = −74.091367 au at RCCSD(T)/6-311+G(2df)//RCCSD(T)/6-311+G*.

[c] Ref. [110].

[d] Aug-cc-pvTZ basis set was augmented by two s and one p functions at the bond centers (Refs. [75,76]).

[e] Property was not calculated at this level of theory.

[f] R_0(B–B), B = 1.19064(157) cm^{-1} and C = 0.59532(79) cm^{-1} (Ref. [76]).

states with π-orbitals being occupied before σ-orbitals is due to the low valence atomic charges. B_2 simply cannot favorably support six σ valence electrons. As we will show below this factor is crucial for understanding the unusual planar shape of all-boron clusters.

3.2. Triatomic clusters: B_3, B_3^+, and B_3^-

3.2.1. B_3

The first ab initio study on B_3 is dated 1981, when Whiteside performed unrestricted Hartree–Fock and UMP4 calculations on clusters of beryllium and boron [109]. Since then, the triatomic boron cluster has received a significant attention in the literature [53,54,60–62,66,75–77,109–130].

There is a consensus in the literature that the neutral B_3 is a D_{3h} $^2A_1'$ ($1a_1'^2 1e'^4 1a_2''^2 2a_1'^1$) triangular radical species in its ground electronic state. Molecular properties of the global minimum B_3 structure computed at various levels of theory and experimentally determined are given in Table 1 [66].

The B_3 valence MOs are shown in Fig. 7.

The HOMO ($2a_1'$) of B_3 is a σ-MO, formed by the radial overlap of the 2p-atomic orbitals on boron atoms, as schematically illustrated in Fig. 7. The HOMO is a completely delocalized orbital with single occupation in neutral B_3, giving rise to a three-center one-electron (3c-1e) bond. The HOMO-1 ($1a_2''$) is a π-MO, formed by the out-of-plane overlap of $2p_z$-AOs from the three B atoms. We localized the remaining set of valence MOs (1e$'$-HOMO-2 and $1a_1'$-HOMO-3) into three 2-center 2-electron (2c-2e) B–B bonds with the occupation numbers (ON) 1.89e using NBO analysis at the RHF/6-311+G* level of theory in the putative B_3^{3+} cation ($1a_1'^2 1e'^4$ electronic configuration) at the geometry of the neutral B_3 cluster [130]. The strong s–p hybridization in the B_3^{3+} cation (occupation numbers are $2s^{0.96} 2p^{1.03}$) is responsible for bonding character of the lowest three valence MOs (correction to our statement in the Ref. [66]). The two electrons in the fully delocalized π HOMO-1 make B_3 π-aromatic, obeying the $4n + 2$ Hückel's rule for $n = 0$. Although not technically obeying the $4n + 2$ Hückel's rule for aromaticity, B_3 is also partially σ-aromatic derived from the single occupation of the fully σ-delocalized HOMO.

The second lowest-energy state D_{3h} $^2A_2''$ with the $1a_1'^2 1e'^4 1a_2''^1 2a_1'^2$ electronic configuration arises from the one

electron excitation from HOMO-1 to HOMO. The D_{3h} $^2A_2''$ species was theoretically predicted to be 0.66 eV higher in energy than the global minimum (CCSD(T)/6-311+G(2df) level of theory) [66] and that number reasonably agrees with the experimental value of 0.74 eV [66]. An extensive ab initio study of alternative structures of B_3 in different spectroscopic states has been carried out by Hernandez and Simons [110]. The overview of the theoretically identified spectroscopic states of the triangular, distorted, and linear species is shown in Fig. 8.

No species with stable geometries were found to have symmetry lower than C_{2v}. The ZPE-corrected barriers between the minima were also calculated [110].

A spectroscopic study of B_3 has been performed by Maier and co-workers [75,76]. They assigned two bands with origins at 736 nm and 458 nm to the $X^2A_1' \rightarrow 1^2E'$ and $X^2A_1' \rightarrow 2^2E'$ transitions, respectively, on the basis of their ab initio calcula-
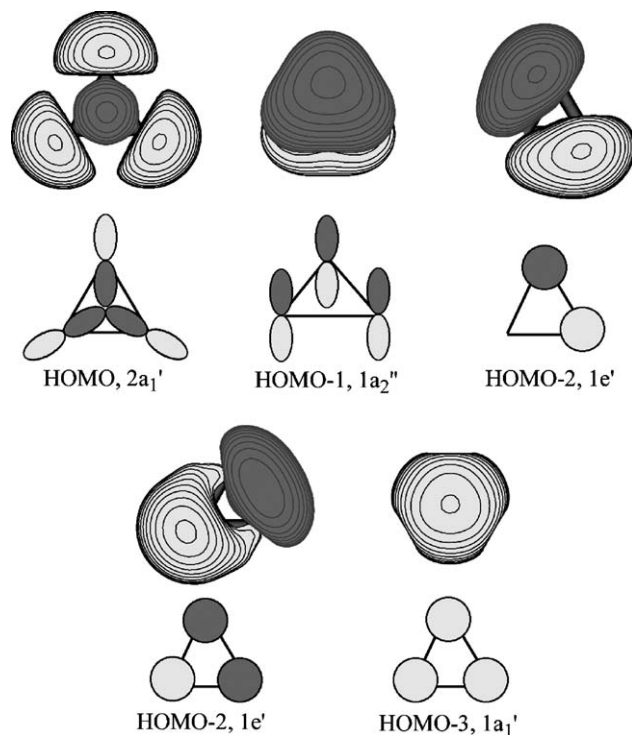

Fig. 7. Molecular orbital picture of the B_3 (D_{3h} $^2A_1'$) cluster. The order of the orbitals given in accordance with R(U)OVGF/6-311+G(2df) calculations.
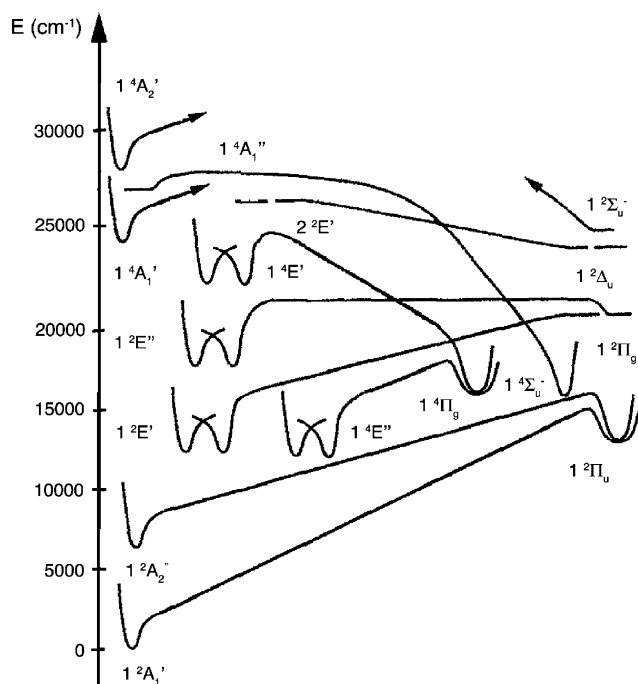
Fig. 8. Low-lying states in B_3. Curves represent states that have been geometrically optimized. The horizontal lines represent states for which energies are known but whose geometries have not been optimized. (Reprinted with permission from Ref. [110]. Copyright 1991 American Institute of Physics.)

tions. The two low-lying $1^2E'$ and $2^2E'$ states were assigned as originating from the ground electronic state through the $2a_1'$-HOMO $\rightarrow$ $2e'$-LUMO and $1e'$-HOMO-1 $\rightarrow$ $2a_1'$-HOMO excitations, respectively, though with the substantial mixing between the two. The complex vibrational structure in the $1^2E'$ state was interpreted on the basis of the strong Jahn–Teller distortion. The $2^2E'$ state undergoes only a relatively weak Jahn–Teller distortion and shows a short progression with an observed frequency of $981(10)$ cm^{-1} which compares favorably with the theoretical frequency of 973 cm^{-1}. The calculated positions for the $1^2E'$ and $2^2E'$ band origins at the CASSCF-MRCISD/aug-cc-pvTZ (augmented by 2s1p bond functions) level of theory were found to be $T_{00} = 12,829$ cm^{-1} and $22,272$ cm^{-1} which are in reasonable agreement with the experimentally observed $13,587$ cm^{-1} and $21,828$ cm^{-1}, respectively [75,76].

The atomization energy for the B_3 cluster in the ground state was first calculated by Martin et al. [115] to be 193 kcal/mol and 189 kcal/mol at the G1 and modified G1 levels of theory, respectively. Our value at the CCSD(T)/6-311+G(2df)/CCSD(T)/6-311+G*+ZPE level of theory is 185 kcal/mol [131].

An experimental electron resonance spectrum of B_3 was recorded by Weltner and co-workers [111] and a follow-up theoretical study (MC-SCF) on the isotropic and anisotropic components of the hyperfine coupling tensor of B_3 was carried out [117]. The authors of the theoretical work concluded that in noble gas matrices B_3 rotates rapidly around its C_3-axis, and the hyperfine coupling predicted theoretically is completely averaged out by such free rotation. Reis et al. performed DFT calculations on dipole polarizabilities and hyperpolarizabilities of boron clusters [118].

Linear B_3 excited isomers were first identified by Pellegatti et al. [119] in their CI-calculations and have been later further studied by Hernandes and Simons [113] and Cao et al. [120]. All linear isomers are significantly higher in energy than the global minimum structure.

The hydrogenation of B_3 has been studied by Hernandez and Simons [113]. Two stable B_3H, and three stable and one metastable B_3H_2 species have been identified. The hydrogen atom abstraction ($B_3 + H_2 \rightarrow B_3H + H$) was found to be endothermic and less favorable than the $B_3 + H_2 \rightarrow B_3H_2$ reaction. B_3H_x ($x = 0$–3) have been observed by mass spectrometry and alternative structures and their stabilities have been studied via MO calculations [114].

3.2.2. B_3^+

The closed-shell cationic B_3^+ cluster was predicted computationally to have a D_{3h} symmetry with the $^1A_1'$ ($1a_1'^2 1e'^4 1a_2''^2$) ground electronic state. It originates from B_3 by removing an electron from the singly occupied HOMO [116,120,122–128]. Theoretical molecular parameters of the ground state of B_3^+ are presented in Table 2 [131].

Other spectroscopic states of the triangular structure and the linear isomers of B_3^+ were found to be higher in energy. The atomization energy for B_3^+ ($B_3^+(^1A_1') \rightarrow 2B(^2P) + B^+(^1S)$) at the CCSD(T)/6-311+G(2df)//CCSD(T)/6-311+G*+ZPE level is 151 kcal/mol [131]. Positively charged boron clusters B_n^+ ($n = 2$–6) were studied by Garcia-Molina et al. [126]. The authors analyzed theoretically the effect of stopping power due to the geometric structures of pure-boron cationic clusters incident on an amorphous carbon target. The stopping power was found to increase with increasing cluster size.

The molecular orbital picture of the global minimum of B_3^+ is very similar to that of the neutral B_3 cluster (Fig. 7). The completely bonding fully delocalized π-MO ($1a_2''$) is now the HOMO, which is doubly occupied. The cation thus remains π-aromatic according to the $4n + 2$ Hückel's rule, but it is not a σ-aromatic species anymore. The cation still has three 2c-2e B–B bonds.

3.2.3. B_3^- and its photoelectron spectra

The anionic B_n^- clusters have received considerably less attention than the neutral and cationic species. However, anionic clusters are especially important for the contemporary inorganic chemistry, since potentially they can be used as new inorganic ligands, for example, by coordination to cationic metal atoms. Only a limited number of experimental and theoretical studies have been done on the anionic B_3^- cluster [66,75,120,130]. The anionic B_3^- species has D_{3h} symmetry with $1a_1'^2 1e'^4 1a_2''^2 1a_1'^2$ closed-shell electronic configuration. Molecular properties of the B_3^- cluster are given in Table 2 [66].

Kuznetsov and Boldyrev [130] predicted the vertical one-electron detachment energies for B_3^-. Zhai et al. obtained the first PES spectra of B_3^- at various photon energies, as shown in Fig. 9 [66].

All features (except peak B) of the spectra correspond to the previously predicted VDEs [130]. However, the peak B with

Table 2
Molecular properties of B_3^- (D_{3h}, $^1A_1'$) and B_3^+ (D_{3h}, $^1A_1'$) [66,130,131]

	B3LYP/6-311+G*	MP2/6-311+G*	RCCSD(T)/6-311+G*	RCCSD(T)/6-311+G(2df)[a]	CASMRCI/6-311+G(2df)[b]
B_3^-					
E_{total} (a.u.)	−74.397068	−74.13300	−74.164651	−74.196742	−74.166109
R(B–B) (Å)	1.542	1.568	1.576	[c]	1.552
$\omega_1(a_1')$ (cm^{-1})	1239	1284	1190	[c]	[c]
$\omega_2(e')$ (cm^{-1})	959	936	897	[c]	[c]
B_3^+					
E_{total} (a.u.)	−73.936143	−73.669332	−73.712635		
R(B–B) (Å)	1.564	1.620	1.617	[c]	
$\omega_1(a_1')$ (cm^{-1})	1188	1040	1077	[c]	
$\omega_2(e')$ (cm^{-1})	990	897	900	[c]	

[a] Energy calculated at the CCSD(T)/6-311+G* geometry.
[b] The active space for the CAS-MRCI calculations was constructed the following way: rhf;occ,5,1,2,0;closed,5,1,2,0;core,2,0,1,0;wf,16,1,0;multi/ci;occ,8,1,4,0; closed,3,0,1,0;core,2,0,1,0;wf,16, 1,0.
[c] Properties were not calculated at this level of theory.

relatively weak intensity was not predicted before. This feature was identified as a shake-up process, i.e., a two-electron transition on the basis of accurate ab initio calculations [66]. The full assignment of the spectral features on the basis of various levels of theory is presented in Table 3.

Our assignment of the B peak in the B_3^- photoelectron spectra to the B_3 final $1^2E'$ ($1a_1'^2 1e'^4 1a_2''^2 2a_1'^0 2e'^1$) shake-up state agrees with the subsequent interpretation of the spectroscopic spectra of B_3 by Maier and co-workers [75,76].

Maier and co-workers [75,76] recently conducted near infrared studies of B_3^- in a neon matrix. They observed a band with origin at 467 nm which they assigned to the $X^1A_1' \rightarrow {}^1E'$ electronic transition of the cyclic anion on the basis of their ab initio calculations.

The atomization energy for B_3^- ($B_3^-(^1A_1') \rightarrow 2B(^2P) + B^-(^3P)$) at the CCSD(T)/6-311+G(2df)//CCSD(T)/6-311+G*+ZPE level is 249 kcal/mol, clearly indicating an enhanced stability compared to B_3^+ and B_3 [131].

The molecular orbital picture of the anionic B_3^- species is almost identical to that of the neutral cluster (Fig. 7). The σ-radial HOMO ($2a_1'$) is now doubly occupied. Consequently, the cluster possesses two electrons in the σ-radial MOs and could be considered as σ-aromatic. Thus, B_3^- is doubly (σ- and π-) aromatic, and that is consistent with its enhanced stability. The double aromaticity in B_3^- has also been confirmed by calcula-

tions of nucleus-independent chemical shift (NICS), which was introduced by Schleyer and co-workers as probe of aromaticity [132]. According to our calculations [133], the NICS value (at B3LYP/6-311+G*) is −73.6 ppm at the center and −22.6 ppm 1.0 Å above the center of B_3^-. The substantial reduction in the NICS value from the center of cluster to 1.0 Å above the center is a clear indication of double aromaticity, because at the center both the σ-aromatic HOMO and π-aromatic HOMO-1 contribute to the NICS value, while 1.0 Å above the center of the cluster, the contribution to NICS comes primarily from the π-aromatic HOMO-1. These numbers can be compared to NICS of prototypical aromatic molecule of benzene NICS(0) = −8.9 ppm and NICS(1.0) = −10.2 ppm (both at B3LYP/6-311+G*) [132b]. The B_3^- anion has also three 2c-2e B–B bonds, as in B_3^+ and B_3.

Kuznetsov and Boldyrev theoretically predicted [130] that B_3^- could be a part of a gas-phase salt molecule Na$^+$B$_3^-$. They have shown that in the most stable C_{3v} ($^1A_1$) structure of NaB$_3$ the Na$^+$ cation is coordinated to the B_3^- anion in a half-sandwich manner. The geometric parameters and harmonic frequencies of B_3^- being a part of Na$^+$B$_3^-$ (R(B–B) = 1.576 Å, $\omega_1(a_1)$ = 1186 cm^{-1}, $\omega_2(e)$ = 895 cm^{-1}) are almost identical to those of the isolated B_3^- (R(B–B) = 1.576 Å, $\omega_1(a_1)$ = 1190 cm^{-1}, and $\omega_2(e)$ = 897 cm^{-1}, all at CCSD(T)/6-311+G*). The bonding between Na and B_3 was found to be quite ionic: Q(Na) = +0.88e and Q(B$_3^-$) = −0.88e (NBO charges at

Table 3
Comparison of experimental and calculated VDEs (in eV) for B_3^- [66]

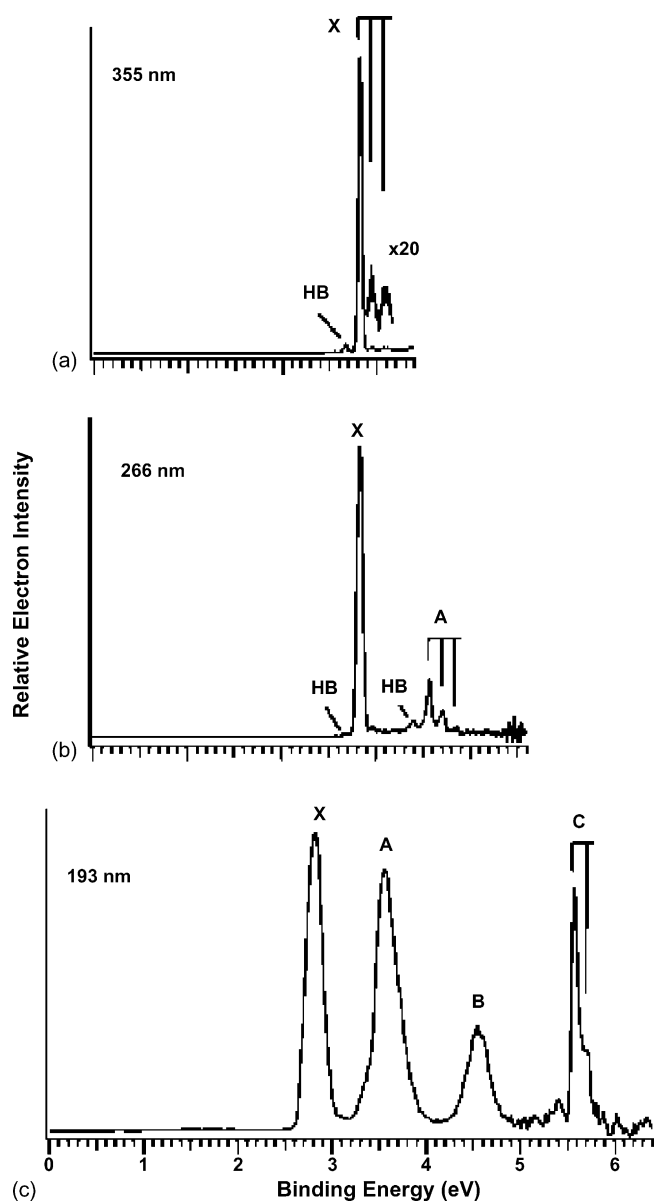| Experimental spectrum		Theoretical spectrum			
Band	VDE	Final state	VDE		
			ROVGF/6-311+G(2df)[a]	ADC(3)/6-311+G(2df)	RCCSD(T)/6-311+G(2df)
X	2.82 ± 0.02	$^2A_1'$, $1a_1'^2 1e'^4 1a_2''^2 2a_1'^1 2e'^0$	2.72 (0.87)	2.68 (0.84)	2.88
A	3.56 ± 0.03	$^2A_2''$, $1a_1'^2 1e'^4 1a_2''^1 2a_1'^2 2e'^0$	3.57 (0.88)	3.57 (0.87)	3.54
B	4.55 ± 0.03	$^2E'$, $1a_1'^2 1e'^4 1a_2''^2 2a_1'^0 2e'^1$			4.70
		$^4E''$, $1a_1'^2 1e'^4 1a_2''^2 2a_1'^1 2e'^1$			4.82
C	5.58 ± 0.03	$^2E'$, $1a_1'^2 1e'^3 1a_2''^2 2a_1'^2 2e'^0$	5.31 (0.83)	5.43 (0.69)	

[a] Data from Ref. [130].

Fig. 9. Photoelectron spectra of B_3^- at: (a) 355 nm (3.496 eV), (b) 266 nm (4.661 eV), and (c) 193 nm (6.424 eV). HB stands for hot band transitions. The vertical lines indicate resolved vibrational structures. (Reprinted with permission from Ref. [66]. Copyright 2003 American Chemical Society.)

$MP2/6-311+G^*$). This first example of a salt molecule shows that B_3^- could be a new inorganic ligand in coordinational chemistry.

3.3. Tetraatomic clusters: B_4, B_4^+, B_4^-, B_4^{2-}

3.3.1. B_4

The neutral B_4 cluster was considered carefully by Martin et al., who used several levels of theory (HF/6-31G*, MP2/6-31G*, MP2/6-311G*, and QCISD(T)/6-311G*) for the geometry optimization [134]. They predicted the D_{2h} ^1A_g rhombus global minimum structure. We recently performed the GEGA search [135] and confirmed this global minimum structure, which is shown in Fig. 10 with other low-lying isomers.

We ran the GEGA search for the global minimum structure separately for the singlet and the triplet structures. Furthermore, since the structures generated in GEGA are random, the symmetry of B_4 is usually C_1, or it can be C_s or $D_{\infty h}$ for deliberately generated planar and linear structures. Thus, although the most stable species obtained is effectively D_{2h}, in fact, it does not possess any symmetry from the GEGA run. The symmetry was identified and imposed manually during the calculations at higher levels of theory so that the ground spectroscopic state could be properly determined.

There was a report [139] indicating that the global minimum of B_4 has a C_{2h} symmetry. Also, Kato and Tanaka pointed out that at the HF level the triplet C_{2h} (^3B_u) is the lowest energy structure, but at the MP4 level the rhombus D_{2h} (^1A_g) becomes more stable [140]. However, today there is a consensus in the literature that the global minimum of B_4 is the D_{2h} (^1A_g) rhombus (Table 4) with the $1a_g^2 1b_{1u}^2 1b_{2u}^2 1b_{3g}^2 1b_{3u}^2 2a_g^2$ electronic configuration [60,62,66,116,118,122,124,125,134–138,140].

The geometric distortion toward rhombus structure is rather modest. The barrier on the potential energy surface along the coordinate of internal transformation $D_{2h} \rightarrow D_{4h} \rightarrow D_{2h}$ is quite low (0.7 kcal/mol at CCSD(T)/aug-cc-pvQZ//CCSD(T)/aug-cc-pvTZ, according to Maier and co-workers [141], and 0.8 kcal/mol at CCSD(T)/6-311+G* according to our study [66]), leading to the splitting of vibrational transitions of B_4. These results agree with another computational study by Reis and Papadopoulos [136], who, using many sophisticated methods (CCSD(T)/CASSCF, MPn, and BD(T)), calculated dipole polarizability and second hyperpolarizability of the B_4 rhombus D_{2h} (^1A_g) structure.

Maier and co-workers calculated vertical and adiabatic excitation energies and transition moments between the global minimum and the excited states using a variety of theoretical methods. The lowest energy excited state of B_4 was found to be the $^1B_{1g}$ state, whose vertical excitation energy was found to be ~3.0 eV and adiabatic excitation energy ~2.1 eV) [141].

Fig. 11a displays the molecular orbital pictures of the D_{2h} (^1A_g) B_4 cluster.

The lowest four MOs (HOMO-2 to HOMO-5) can be localized, as has been shown by NBO analysis, into four classical 2c-2e B–B bonds [66]. The strong s–p hybridization on both the boron atoms: $2s^{0.95}2p^{1.14}$ and $2s^{1.04}2p^{0.83}$ (from HOMO-2 to HOMO-5), is responsible for the formation of the four classical bonds. The remaining two MOs are fully delocalized, and participate in the global bonding in the cluster. The HOMO-1 ($1b_{3u}$) is a completely bonding π-molecular orbital formed by the out-of-plane overlap of $2p_z$-AOs on the B atoms. The two electrons populating this MO make the cluster π-aromatic according to the $4n + 2$ Hückel's rule. The HOMO is a σ-radial molecular orbital, just as the HOMO in B_3 and B_3^-, formed by the radial overlap of 2p-AOs. The system thus can be characterized as σ-aromatic as well, i.e., B_4 is also doubly aromatic.

There is nothing in the MO picture of B_4 (Fig. 10) indicating the distortion from the perfect square structure. The rhombus distortion comes from the second-order (or "pseudo") Jahn–Teller effect, as discussed by Martin et al. [134]. Because of this nature of the distortion, the barrier for "squareness" is rather small, as

Fig. 10. Alternative structures of B_4 identified by GEGA (B3LYP/3-21G level of initial computation), and refined at the B3LYP/6-311+G* level of theory. (Reprinted with permission from Ref. [66]. Copyright 2003 American Chemical Society.)

discussed above, and even at moderate temperature the B_4 cluster has effectively a square structure.

The rhombus shape of the neutral B_4 unit has been predicted to be a part of the experimentally observed $B_4(CO)_2$ carbonyl complex [142]. The two CO-ligands are coordinated to B-atoms of the rhombus opposing each other. The species was reported to be a diradical, and the HOMO–LUMO gap in the closed-shell D_{2h} (^1A_g) cluster was computationally shown to be very small. The energies of the open-shell singlet ($^1B_{2g}$) and triplet ($^3B_{2g}$) states were predicted to be very close, with the open-shell singlet being lower by 1.1 kcal/mol at the (U)CCSD(T)/6-31G* level [142].

Table 4
Molecular properties of B_4

	B3LYP/6-311+G^{*a}	MP2/6-311+G^{*b}	MP2/cc-pvTZ^c	MP4/cc-pvTZ^c	CCSD(T)/6-311+G^{*a,d}	CCSD(T)/aug-cc-pvQZ^e
E_{total} (a.u.)	−99.15755	−98.79592	−98.8423	−98.8898	−98.83944	−98.91001
$R(B_1-B_2)$ (Å)	1.523	1.557	1.546	1.557	1.558	1.539
$\angle B_2-B_1-B_3$ (°)	76.5	73.8	74.2	72.9	75.4	75.8
$\omega_1(a_g)$ (cm^{-1})	1183	1113	1123	f	1112	f
$\omega_2(a_g)$ (cm^{-1})	332	426	400	f	336	f
$\omega_3(b_{3g})$ (cm^{-1})	1268	1156	1177	f	1173	f
$\omega_4(b_{1u})$ (cm^{-1})	1267	1244	1257	f	1201	f
$\omega_5(b_{2u})$ (cm^{-1})	1059	968	990	f	966	f
$\omega_6(b_{3u})$ (cm^{-1})	320	326	329	f	287	f

[a] Refs. [66,137].
[b] Ref. [137].
[c] Ref. [136].
[d] Ref. [66]. E_{total} = −98.881103 a.u. at RCCSD(T)/6-311+G(2df)/CCSD(T)/6-311+G*.
[e] Ref. [141].
[f] This property was not reported.
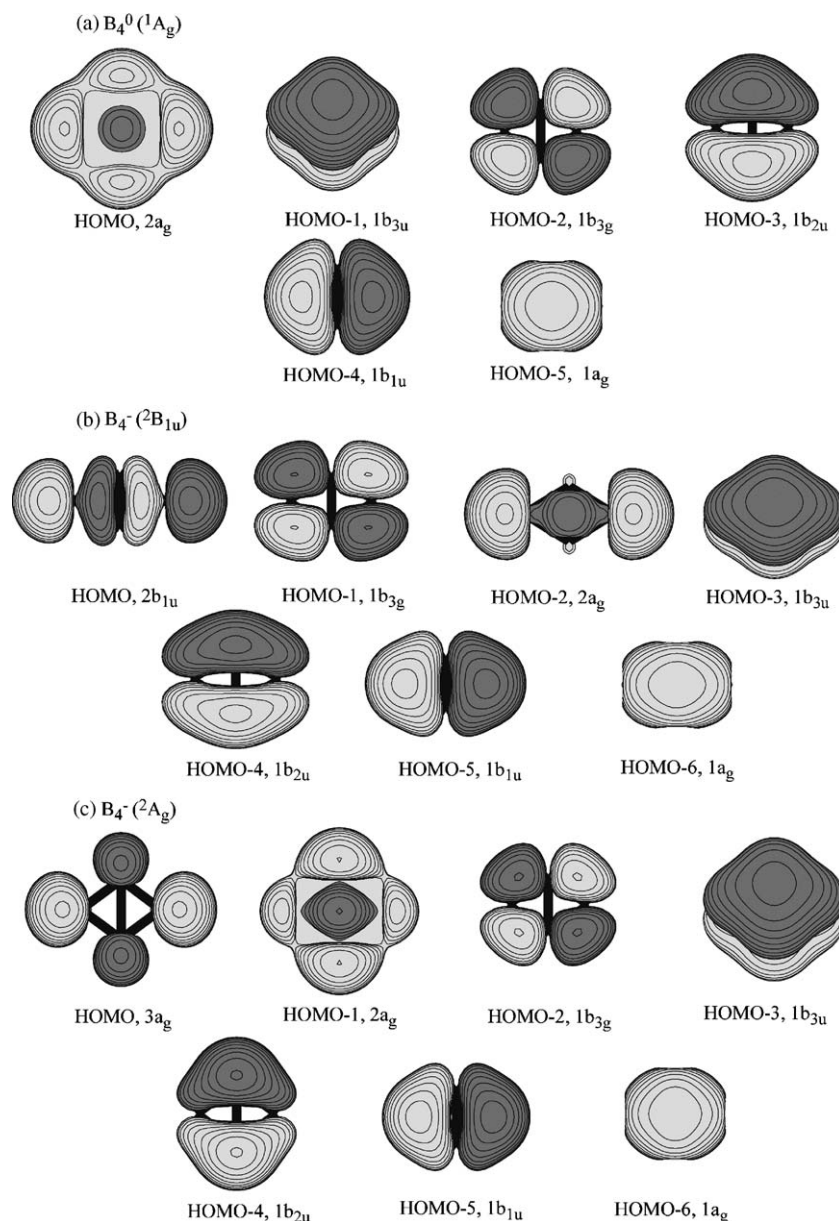
Fig. 11. Molecular orbital pictures of: (a) B_4^0 (D_{2h}, ^1A_g); (b) B_4^- (D_{2h}, $^2B_{1u}$); (c) B_4^- (D_{2h}, ^2A_g). The order of the orbitals given in accordance with R(U)OVGF/6-311+G(2df) calculations. (Reprinted with permission from Ref. [66]. Copyright 2003 American Chemical Society.)

The atomization energy for B_4 at the CCSD(T)/6-311+G(2df)//CCSD(T)/6-311+G*+ZPE level is 303 kcal/mol [131].

3.3.2. B_4^+

The cationic B_4^+ cluster was also reported to have the D_{2h} ^2A_g ($1a_g^2 1b_{1u}^2 1b_{2u}^2 1b_{3g}^2 1b_{3u}^2 2a_g^1$) rhombus global minimum structure [61,116,122,124,137,138,141]. Calculated molecular parameters of the ground electronic state are summarized in Table 5.

The barrier for the intramolecular rearrangement of the rhombus B_4^+ structure through a square D_{4h} transition state is nearly 10 times smaller than that of the neutral B_4 cluster [61,138], and thus the splitting of vibrational transitions should be even smaller. The lowest excited state, D_{2h} $^2B_{1g}$, is only 0.17 eV higher in energy [138].

The chemical bonding pattern in the rhombus global minimum of B_4^+ is very similar to that of the neutral B_4 (D_{2h}, ^1A_g) described above (see Fig. 11). The deep $1a_g$, $1b_{1u}$, $1b_{2u}$, and $1b_{3g}$ valence molecular orbitals can be localized onto four peripheral classical 2c-2e B–B bonds in the cluster. The remaining HOMO ($2a_g$) and HOMO-1 ($1b_{3u}$) are globally delocalized bonding σ-radial and π-molecular orbitals. With two π-electrons, the cluster is still π-aromatic. In addition, it also can be called partially σ-aromatic due to the presence of one electron on the bonding σ-HOMO [142]. The NICS calculations by Jin and Li [137] clearly support the description of chemical bonding: NICS(0.0) = −33.4 ppm and NICS(1.0) = −6.6 ppm.

The atomization energy for B_4^+ (B_4^+ (^2A_g) → 3B (^2P) + B$^+$ (^1S)) at the CCSD(T)/6-311+G(2df)//CCSD(T)/6-311+G*+ZPE level is 267 kcal/mol [131].

Table 5
Molecular properties of B_4^+

	B3LYP/6-311+G*[a]	MP2/6-311+G*[a]	QCISD(T)6-311+G*[b]	CCSD(T)/6-311+G*[c]
E_{total} (a.u.)	−98.81099	−98.43509	−98.45972	−98.483573
$R(B_1–B_2)$ (Å)	1.546	1.564	1.569	1.576
$\angle B_2–B_1–B_3$ (°)	82.5	82.2	80.9	80.5
$\omega_1(a_g)$ (cm^{-1})	1145	1174	[d]	1089
$\omega_2(a_g)$ (cm^{-1})	201	139	[d]	281
$\omega_3(b_{3g})$ (cm^{-1})	1118	1103	[d]	1027
$\omega_4(b_{1u})$ (cm^{-1})	1189	1394	[d]	1177
$\omega_5(b_{2u})$ (cm^{-1})	1076	1056	[d]	1001
$\omega_6(b_{3u})$ (cm^{-1})	270	281	[d]	281

[a] Refs. [131,137].
[b] Ref. [137].
[c] Ref. [131]. E_{total} = −98.5222237 a.u. at UCCSD(T)/6-311+G(2df)/CCSD(T)/6-311+G*.
[d] This property was not reported.

3.3.3. B_4^- and its photoelectron spectra

The structure of the anionic B_4^- cluster has been a subject of controversy in the recent literature. Initially, Jin and Li [137] predicted that the rhombus D_{2h} (^2A_g) structure is the global minimum of the B_4^- cluster. However, we identified two competing electronic states: D_{2h}, $^2B_{1u}$ ($1a_g^2 1b_{1u}^2 1b_{2u}^2 1b_{3u}^2 2a_g^2 1b_{3g}^2 2b_{1u}^1$) and ^2A_g ($1a_g^2 1b_{1u}^2 1b_{2u}^2 1b_{3u}^2 2a_g^2 1b_{3g}^2 2b_{1u}^0 3a_g^1$) [66]. The GEGA search (B3LYP/3-21G) for the global minimum predicted the rhombus D_{2h} $^2B_{1u}$ structure to be the global minimum [135]. The identified lowest-energy structures are given in Fig. 12.

As one may see, seven different rhombus isomers were found within 40 kcal/mol above the global minimum. The D_{2h} ^2A_g isomer reported by Jin and Li as a global minimum [137] was found to be the second most stable isomer. At higher levels of theory, the relative energies of the rhombus species D_{2h} ^2A_g and D_{2h} $^2B_{1u}$ (Fig. 12) vary [66]. The $^2B_{1u}$ state was predicted to be the most stable at our CASSCF(3,4)-MRCISD/6-311+G(2df)/RCCSD(T)/6-311+G* (by 3.0 kcal/mol) and CASSCF(3,5)-MRCISD/RCCSD(T)/6-311+G* (by 5.8 kcal/mol) highest levels of theory. However, we found that the ^2A_g state is slightly more stable at RCCSD(T)/6-

I, D_{2h} ($^2B_{1u}$)
NImag=0
ΔE= 0.0 kcal/mol

II, D_{2h} (^2A_g)
NImag=0
ΔE=6.1 kcal/mol

III, C_{2h} (^4B_u)
NImag=0
ΔE=26.2 kcal/mol

IV, D_{2h} ($^4B_{1u}$)
NImag=1
ΔE=26.6 kcal/mol

V, D_{2h} ($^4B_{2u}$)
NImag=1
ΔE=27.6 kcal/mol

VI, D_{2h} ($^2B_{2u}$)
NImag=0
ΔE=35.3 kcal/mol

VII, C_s ($^2A'$)
NImag=0
ΔE=35.9 kcal/mol

VIII, D_{2h} ($^2B_{2g}$)
NImag=0
ΔE=40.4 kcal/mol

IX, C_{2v} ($^2B_2$)
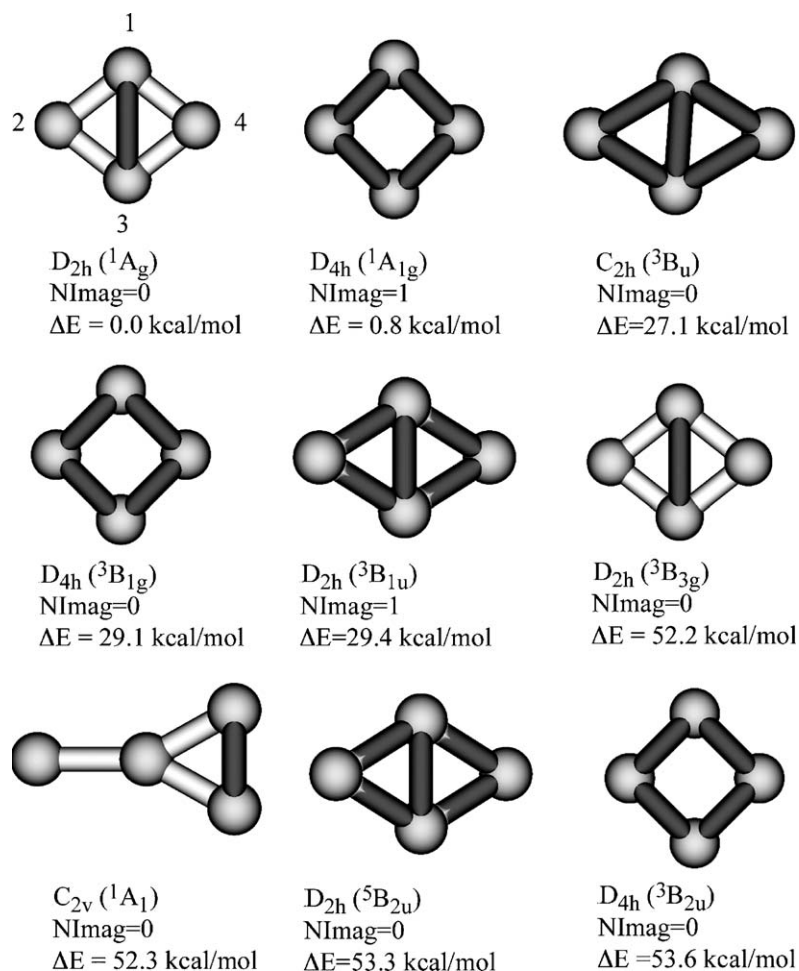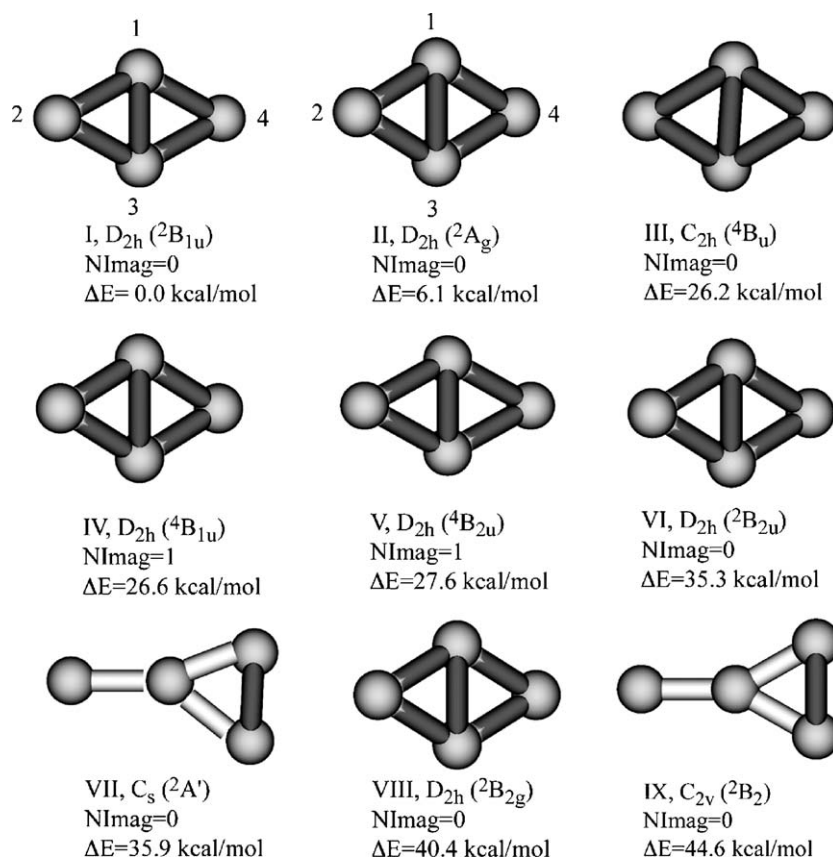NImag=0
ΔE=44.6 kcal/mol

Fig. 12. Alternative structures of B_4^- identified by GEGA (B3LYP/3-21G level of initial computation), and refined at the B3LYP/6-311+G* level of theory. (Reprinted with permission from Ref. [66]. Copyright 2003 American Chemical Society.)

Table 6
Molecular properties of B_4^-

	B_4^-, D_{2h} ($^2B_{1u}$)			B_4^-, D_{2h} (^2A_g)		
	B3LYP/6-311+G^{*a}	CASSCF/aug-cc-pvTZ[b]	RCCSD(T)/6-311+G^{*c}	B3LYP/6-311+G^{*a}	CASSCF/aug-cc-pvTZ[b]	RCCSD(T)/6-311+G^{*d}
E_{total} (a.u.)	−99.226968	e	−98.895463	−99.217253	e	−98.898718
ΔE (kcal/mol)	0.0	e	2.04	6.1	e	0.0
$R(B_1–B_2)$ (Å)	1.568	1.583	1.595	1.578	1.606	1.621
$\angle B_1–B_2–B_3$ (°)	63.5	63.3	63.6	84.3	68.6	73.8
$\omega_1(a_g)$ (cm^{-1})	1138	e	e	1053	e	e
$\omega_2(a_g)$ (cm^{-1})	800	e	e	136	e	e
$\omega_3(b_{3g})$ (cm^{-1})	1039	e	e	1116	e	e
$\omega_4(b_{1u})$ (cm^{-1})	1008	e	e	738	e	e
$\omega_5(b_{2u})$ (cm^{-1})	804	e	e	844	e	e
$\omega_6(b_{3u})$ (cm^{-1})	284	e	e	336	e	e

　[a] Ref. [66].

　[b] Ref. [141].

　[c] Ref. [66]. $E_{total} = -98.940051$ a.u. at RCCSD(T)/6-311+G(2df)/CCSD(T)/6-311+G*. The ^2A_g state is more stable at RCCSD(T)/6-311+G(2df)/CCSD(T)/6-311+G* by 0.4 kcal/mol. The $^2B_{1u}$ state is more stable at CASSCF(3,4)-MRCISD/6-311+G(2df) by 3.0 kcal/mol and at CASSCF(3,4)-MRCISD/6-311+G(2df) by 5.8 kcal/mol.

　[d] Ref. [66]. $E_{total} = -98.940741$ a.u. at RCCSD(T)/6-311+G(2df)/CCSD(T)/6-311+G*.

　[e] This property was not reported.

311+G* (by 2.0 kcal/mol) and at RCCSD(T)/6-311+G(2df) (by 0.4 kcal/mol). Maier and co-workers [141] recently reported that the D_{2h} $^2B_{1u}$ is the most stable at the RCCSD(T)/aug-cc-VQZ level of theory, in agreement with our MRCISD/6-311+G(2df) results. Molecular properties of the two most stable isomers of the cluster are given in Table 6.

The PES spectra of B_4^- at three photon energies have been recently recorded, and they are shown in Fig. 13 [66].

Four very broad bands were observed. The A and B bands were closely spaced and were overlapped. At 355 nm, vibrational structures were discernible for the A band (Fig. 13). The broad X band indicated a large geometry change between the ground

Table 7
Comparison of the experimental VDEs of B_4^- with calculated VDEs for the $^2B_{1u}$ and ^2A_g states of B_4^- [66]

Experimental spectra		Theoretical interpretation		
Band	VDE (eV)	Final state	VDE (eV)	
			RCCSD(T)/6-311+G(2df)	EOM-RCCSD(T)/6-311+G(2df)
$^2B_{1u}$ B_4^-				
X	1.99 ± 0.05	^1A_g, $1a_g^2 1b_{1u}^2 1b_{2u}^2 1b_{3u}^2 2a_g^2 1b_{3g}^2 2b_{1u}^0$	1.85[a]	
A	3.08 ± 0.03	$^3B_{2u}$, $1a_g^2 1b_{1u}^2 1b_{2u}^2 1b_{3u}^2 2a_g^2 1b_{3g}^1 2b_{1u}^1$	3.14	
B	3.41 ± 0.03	$^3B_{1u}$, $1a_g^2 1b_{1u}^2 1b_{2u}^2 1b_{3u}^2 2a_g^1 1b_{3g}^2 2b_{1u}^1$	3.24	
C	4.39 ± 0.05	$^1B_{2u}$, $1a_g^2 1b_{1u}^2 1b_{2u}^2 1b_{3u}^2 2a_g^2 1b_{3g}^1 2b_{1u}^1$		4.03
		$^3B_{2g}$, $1a_g^2 1b_{1u}^2 1b_{2u}^2 1b_{3u}^1 2a_g^2 1b_{3g}^2 2b_{1u}^1$	4.35	
		$^1B_{2g}$, $1a_g^2 1b_{1u}^2 1b_{2u}^2 1b_{3u}^1 2a_g^2 1b_{3g}^2 2b_{1u}^1$		4.65
		$^1B_{1u}$, $1a_g^2 1b_{1u}^2 1b_{2u}^2 1b_{3u}^2 2a_g^1 1b_{3g}^2 2b_{1u}^1$		5.37
^2A_g B_4^-				
X	1.99 ± 0.05	^1A_g, $1a_g^2 1b_{1u}^2 1b_{2u}^2 1b_{3u}^2 1b_{3g}^2 2a_g^2 3a_g^0$	1.87[b]	
A	3.08 ± 0.03			
B	3.41 ± 0.03	^3A_g, $1a_g^2 1b_{1u}^2 1b_{2u}^2 1b_{3u}^2 1b_{3g}^2 2a_g^1 3a_g^1$	3.47	
		$^3B_{3g}$, $1a_g^2 1b_{1u}^2 1b_{2u}^2 1b_{3u}^2 1b_{3g}^1 2a_g^2 3a_g^1$	3.61	
C	4.39 ± 0.05	$^3B_{3u}$, $1a_g^2 1b_{1u}^2 1b_{2u}^2 1b_{3u}^1 1b_{3g}^2 2a_g^2 3a_g^1$	4.05	
		$^1B_{3g}$, $1a_g^2 1b_{1u}^2 1b_{2u}^2 1b_{3u}^2 1b_{3g}^1 2a_g^2 3a_g^1$		4.34
		$^1B_{3u}$, $1a_g^2 1b_{1u}^2 1b_{2u}^2 1b_{3u}^1 1b_{3g}^2 2a_g^2 3a_g^1$		4.57
		^1A_g, $1a_g^2 1b_{1u}^2 1b_{2u}^2 1b_{3u}^2 1b_{3g}^2 2a_g^1 3a_g^1$		4.61

　[a] VDE for this detachment process has been also calculated as an attachment to the $2b_{1u}$-LUMO of the neutral B_4 cluster using ROVGF/6-311+G(2df) and ADC(3)/6-311+G(2df) methods at the optimal RCCSD(T)/6-311+G* geometry of the $^2B_{1u}$ isomer. Calculated VDE was found to be 1.74 eV (ROVGF) and 2.07 eV (ADC(3)).

　[b] VDE for this detachment process has been also calculated as an attachment to the $3a_g$-LUMO of the neutral B_4 cluster using ROVGF/6-311+G(2df) and ADC(3)/6-311+G(2df) methods at the optimal RCCSD(T)/6-311+G* geometry of the ^2A_g isomer. Calculated VDE was found to be 1.55 eV (ROVGF) and 1.73 eV (ADC(3)).
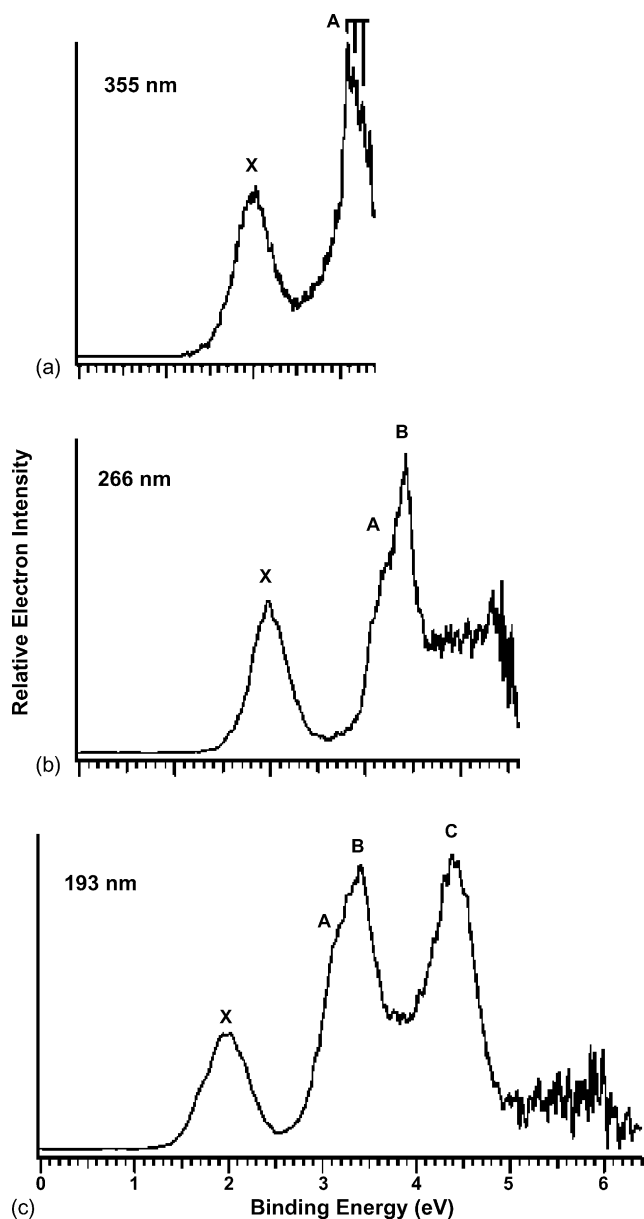
Fig. 13. Photoelectron spectra of B_4^- species at: (a) 355 nm, (b) 266 nm, and (c) 193 nm. (Reprinted with permission from Ref. [66]. Copyright 2003 American Chemical Society.)

states of the anion and neutral B_4. We estimated the ADE or the EA of B_4 to be ~1.6 eV. This makes the EA of B_4 to be the lowest among all the boron clusters from B_3 to B_{25}, partly explaining why the B_4^- anion was relatively unstable and had the weakest abundance from the cluster source.

We computed VDEs of both the D_{2h} ^2A_g and D_{2h} $^2B_{1u}$ isomers of B_4^- using various methods. The experimental data and the theoretical assignments of the features in the photoelectron spectra are given in Table 7.

From the analysis of these results we concluded that the ^2A_g state can be ruled out as a major contributor to the photoelectron spectra of B_4^-. The most convincing argument in the favor of the observation of the $^2B_{1u}$ state comes from the second peak A. In the calculated spectrum of the ^2A_g state, we did not find any one-

electron transition around 3.1 eV, while our calculations revealed the second transition at 3.14 eV with the final state $^3B_{2u}$ for the $^2B_{1u}$ initial state of B_4^-, in excellent agreement with the experimental VDE = 3.08 ± 0.03 eV (Table 7). The observed spectra should be primarily due to the $^2B_{1u}$ state, which was shown to be the ground state at the highest levels of theory [66,138].

Molecular orbitals of both isomers D_{2h} ^2A_g and D_{2h} $^2B_{1u}$ are given in Fig. 11b and c, respectively. The D_{2h} $^2B_{1u}$ isomer, in addition to the molecular orbitals described in Section 3.3.1, has one more σ-MO. The HOMO ($2b_{1u}$) is a part of the quasi-degenerate pair of MOs (the other part is the LUMO). Partial occupation of this quasi-degenerate MO imposes a first-order Jahn–Teller distortion. The rhombus distortion in B_4^- is significantly larger than that in the neutral species: the calculated bond angle ∠B–B–B is about 64° in $^2B_{1u}$ (B_4^-) compared to about 76° in B_4 (see Tables 4 and 6). Thus, the first-order Jahn–Teller distortion is significantly stronger than the second-order Jahn–Teller distortion. The cluster now possesses three σ-electrons (on HOMO and HOMO-2). Although not technically obeying the $4n$ rule for antiaromaticity, the cluster can be called partially σ-antiaromatic, since even partial occupation of the HOMO leads to destabilization and structural distortion of the cluster. The HOMO-3 ($1b_{3u}$) in the cluster is a π-MO, again rendering the cluster π-aromatic. The remaining valence MOs can be again localized into four peripheral 2c-2e bonds. Thus, the D_{2h} $^2B_{1u}$ B_4^- cluster is π-aromatic and σ-antiaromatic [66]. The σ-antiaromaticity of this state is responsible for substantial rhombus distortion from the square (Table 6).

In the second isomer, the $3a_g$ HOMO (the last member of the four MOs: HOMO-6 $1a_g$, HOMO-5 $1b_{1u}$, HOMO-4 $1b_{2u}$, and HOMO $3a_g$ formed primarily of 2s-AOs) is occupied by one electron. This completely antibonding MO does not change much the geometry of the species from that of the neutral cluster. The calculated ∠B–B–B angle is about 84° in ^2A_g (B_4^-) compared to about 76° in the neutral B_4. The double aromaticity and the second-order Jahn–Teller effect still exists in this state of B_4^- [66].

3.3.4. B_4^{2-}

The anionic B_4^- cluster is an open-shell species and in order to become a viable building block it should acquire one more electron and form a B_4^{2-} dianion. Sundholm and co-workers [143] calculated a planar square structure D_{4h} $^1A_{1g}$ ($1a_{1g}^2 1e_u^4 1b_{1g}^2 1b_{2g}^2 2a_{1g}^2 1a_{2u}^2$) of B_4^{2-} using an isoelectronic analogy to Al_4^{2-}, where an extensive search for the global minimum structure has been performed [133,144] and the D_{4h} $^1A_{1g}$ planar square structure was found to be the most stable isomers. The Al_4^{2-} dianion has been studied extensively, and, using a variety of criteria, it was shown that it is a doubly (σ- and π-) aromaticity system ([133,144] and references therein). Sundholm and co-workers [143] predicted the following molecular parameters for B_4^{2-}: R(B–B) = 1.668 A, $\omega_1(a_{1g})$ = 881 cm^{-1}, $\omega_2(b_{1g})$ = 375 cm^{-1}, $\omega_3(b_{2g})$ = 903 cm^{-1}, $\omega_4(b_{2u})$ = 286 cm^{-1}, and $\omega_5(e_u)$ = 709 cm^{-1} (all at CCSD(T)/TZV2P). They also calculated the ring-current susceptibility of B_4^{2-} which was found to be 7.4 nA T^{-1}. That is only 10% smaller than that for the
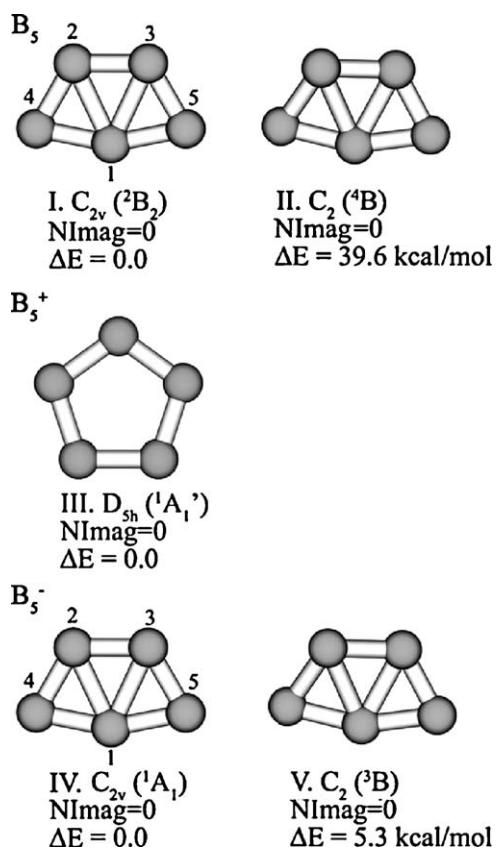
Fig. 14. Global minima and the first lowest-energy isomers of B_5, B_5^+, and B_5^-.

Table 8
Calculated molecular properties of the B_5 (C_{2v}, $^2B_2$) global minimum cluster [67]

	B3LYP/ 6-311+G*	CASSCF(7,8)/ 6-311+G*	RCCSD(T)/ 6-311+G*
E_{total} (a.u.)	−124.003032	−123.218158	−123.596877
$R(B_1–B_{2,3})$ (Å)	1.835	1.868	1.870
$R(B_1–B_{4,5})$ (Å)	1.582	1.584	1.606
$R(B_2–B_3)$ (Å)	1.553	1.552	1.584
$R(B_2–B_4)$ (Å)	1.563	1.591	1.596
$\omega_1(a_1)$ (cm^{-1})	1332	1337	a
$\omega_2(a_1)$ (cm^{-1})	955	958	a
$\omega_3(a_1)$ (cm^{-1})	739	759	a
$\omega_4(a_1)$ (cm^{-1})	602[b]	596[b]	a
$\omega_5(a_2)$ (cm^{-1})	346	368	a
$\omega_6(b_1)$ (cm^{-1})	266	306	a
$\omega_7(b_2)$ (cm^{-1})	1159	1170	a
$\omega_8(b_2)$ (cm^{-1})	1024	939	a
$\omega_9(b_2)$ (cm^{-1})	478	527	a

[a] Frequencies have not been calculated at this level of theory.
[b] $\omega = 550 \pm 40$ cm^{-1} was estimated from the PES of B_5^- [67].

prototypical aromatic molecule, benzene, thus confirming the aromatic nature of the dianion. The planar square B_4^{2-} dianion is a closed-shell system and could potentially be a new ligand in chemistry.

3.4. Pentaatomic clusters: B_5, B_5^+, B_5^-

3.4.1. B_5

Kato and Tanaka reported that B_5 has the C_{2v} $^2A_2$ most stable structure at MP4/3-21G [140]. Ray et al. [116] and Niu et al. [124] predicted a trigonal bipyramid D_{3h} to be the most stable structure (calculations at the UHF, MP2, and MP4 levels). Our results do not agree with all these previous predictions. According to our calculations [67] and a follow-up GEGA run (B3LYP/3-21G level) [135], the B_5 global minimum has the C_{2v} $^2B_2$ ($1a_1^2 1b_2^2 2a_1^2 3a_1^2 1b_1^2 2b_2^2 4a_1^2 3b_2^1$) structure (Fig. 14 and Table 8).

Our GEGA calculations did not reveal any low-lying isomers and the second lowest isomer, C_2 ^4B, (Fig. 14) is about 40 kcal/mol higher. Many other research groups reported the same planar C_{2v} ($^2B_2$) structure as the B_5 global minimum [60,62,118,125,145].

The calculated atomization energy for B_5 (C_{2v} $^2B_2$) is 407 kcal/mol at CCSD(T)/6-311+G(2df)+ZPE [131].

3.4.2. B_5^+

The cationic B_5^+ was reported to be a particularly stable cation (magic cluster) in collision-induced dissociation (CID)

studies by Anderson and co-workers [55]. They also were first to perform ab initio calculations of B_5^+. Anderson and co-workers [55] performed geometry optimizations for the linear, symmetric pentagon, square pyramid, and trigonal bipyramid at the SCF/6-31G* level of theory. They concluded that B_5^+ has the trigonal bipyramid structure. Ray et al. [116] also concluded that the trigonal bipyramid is the most stable structure for the singlet B_5^+. Kato et al. [122] and Ricca and Bauschlicher [61] reported that in the global minimum structure, B_5^+ adopts a planar pentagon slightly distorted toward the C_{2v} symmetry. Ricca and Bauschlicher stated that the D_{5h} ($^1A_1'$) planar pentagon has two imaginary frequencies at the B3LYP/cc-pvTZ level of theory, and, in the global minimum C_{2v} ($^1A_1$) structure, three bond lengths in the slightly distorted pentagon differ by only 0.001 Å and the average bond length is 1.56 Å. They pointed out that the trigonal bipyramid is 2.15 eV above the ground state at B3LYP/cc-pvTZ and 2.23 eV at CCSD(T)/cc-pvTZ. Li and Jin [145] recently confirmed the claim that B_5^+ is not a perfect pentagon, but rather a slightly distorted C_{2v} ($^1A_1$) structure at B3LYP/6-311+G* and MP2/6-311+G* levels of theory.

We performed a GEGA/B3LYP/3-21G search for the global minimum structure of the B_5^+ cluster [135]. Since the structures generated in GEGA are random, the symmetry of B_5^+ is usually C_1, or it can be C_s or $D_{\infty h}$ for deliberately generated planar and linear structures. Thus, the most stable species found by GEGA may not possess the right symmetry. The symmetry was identified and imposed manually during the calculations at higher levels of theory. After such symmetry imposed geometry and frequency calculations, we found that the high symmetry D_{5h} ($^1A_1'$) structure is a second-order saddle point at B3LYP/3-21G and the global minimum structure at this level of theory is only a slightly distorted pentagon with C_{2v} ($^1A_1$) symmetry, similar to that previously reported by Kato et al. [122], Ricca and Bauschlicher [61], and Li and Jin [145]. We performed an extensive study of the B_5^+

Table 9
Calculated molecular properties of B_5^+ (D_{5h}, $^1A_1'$) [131]

	B3LYP/aug-cc-pvDZ	B3LYP/6-311+G*	B3LYP/aug-cc-pvTZ	B3LYP/aug-cc-pvQZ
E_{total} (a.u.)	−123.67774	−123.69292	−123.70495	−123.71186
R(B–B) (Å)	1.562	1.551	1.548	1.547
$\omega_1(a_1')$ (cm^{-1})	971	974	975	975
$\omega_2(e_1')$ (cm^{-1})	1072	1073	1075	1076
$\omega_3(e_2')$ (cm^{-1})	1381	1389	1384	1385
$\omega_4(e_2')$ (cm^{-1})	35 i	64	85	84
$\omega_5(e_2'')$ (cm^{-1})	292	284	290	296

	MP2/aug-cc-pvDZ	MP2/6-311+G*	MP2/aug-cc-pvTZ
E_{total} (a.u.)	−123.21709	−123.24170	−123.30320
R(B–B) (Å)	1.592	1.577	1.568
$\omega_1(a_1')$ (cm^{-1})	918	925	933
$\omega_2(e_1')$ (cm^{-1})	1046	1049	1060
$\omega_3(e_2')$ (cm^{-1})	1285	1294	1311
$\omega_4(e_2')$ (cm^{-1})	69 i	111 i	18 i
$\omega_3(e_2'')$ (cm^{-1})	268	262	268

	CCSD(T)/aug-cc-pvDZ	CCSD(T)/6-311+G*
E_{total} (a.u.)	−123.26661	−123.29043
R(B–B) (Å)	1.596	1.580
$\omega_1(a_1')$ (cm^{-1})	913	921
$\omega_2(e_1')$ (cm^{-1})	1015	1019
$\omega_3(e_2')$ (cm^{-1})	1297	1307
$\omega_4(e_2')$ (cm^{-1})	102 i	138 i
$\omega_3(e_2'')$ (cm^{-1})	252	234

D_{5h} ($^1A_1'$) structure using a variety of theoretical methods (Table 9).

One can see that the D_{5h} ($^1A_1'$) structure is a second-order saddle point at the B3LYP/aug-cc-pvDZ level of theory, but in all other B3LYP calculations with the 6-311+G* and large basis sets it is a minimum. The D_{5h} ($^1A_1'$) structure is a second saddle point in all our MP2 and CCSD(T) calculations. Thus, we concluded that from our best calculations the B_5^+ global minimum structure is not the perfect planar pentagon. However, the global minimum structure is only a slightly distorted pentagon (C_{2v}, $^1A_1$). The energy difference between the distorted pentagon and the perfect pentagon structures is very small at all levels of theory and, after taking into account ZPE corrections, the vibrationally averaged B_5^+ structure is in fact a perfect pentagon. Thus, for all practical purposes we can assume that the D_{5h} ($^1A_1'$) structure is the B_5^+ global minimum.

The beautiful planar pentagon structure of B_5^+ can be understood from its molecular orbital analysis (Fig. 15).

The NBO analysis showed that if we remove four electrons from the HOMO and HOMO-1, the remaining molecular orbitals (HOMO-2 to HOMO-4) in the putative B_5^{5+} cluster can be localized onto five peripheral 2c-2e B–B bonds with strong s–p hybridization on all boron atoms: $2s^{1.03}2p^{0.75}$ (from HOMO-2 to HOMO-4). The HOMO in B_5^+ is a globally bonding σ-MO, and HOMO-1 is a globally bonding π-MO, thus making this cation doubly (σ- and π-) aromatic. Double aromaticity in conjunction with the presence of five 2c-2e B–B peripheral bonds makes the B_5^+ cluster to be vibrationally averaged D_{5h} structure and makes it a magic cluster in CID experiments [55]. The distor-

tion of the D_{5h} ($^1A_1'$) structure found in our MP2 and CCSD(T) calculations can be explained by the second-order Jahn–Teller effect, because there is nothing in occupied MOs (Fig. 15) of the pentagon structure indicating the deviation from high symmetry. That is similar to the rhombus distortion in the B_4 cluster, and like in that case, the second-order distortion makes a very shallow potential energy surface for B_5^+.

3.4.3. B_5^- and its photoelectron spectra

The anionic B_5^- cluster has been studied both experimentally and theoretically [67,145,146]. There is an agreement in the literature that the B_5^- anion has a planar C_{2v} $^1A_1$ ($1a_1^2 1b_2^2 2a_1^2 3a_1^2 1b_1^2 2b_2^2 4a_1^2 3b_2^2$) ground state structure shown in Fig. 14. The molecular properties of the C_{2v} ($^1A_1$) structure are summarized in Table 10.

Our recent GEGA (B3LYP/3-21G run) search confirmed the global minimum structure and showed that there are no other singlet isomers within 15 kcal/mol [135]. We found, however, the low-lying C_2 (^3B) triplet isomer (Fig. 14), which was only 5.3 kcal/mol less stable than the global minimum at the B3LYP/6-311+G* level of theory [67].

The PES spectra of B_5^- were recorded at three detachment photon energies [67], as shown in Fig. 16.

The X and A bands were vibrationally resolved, as indicated by the vertical lines. The 355 nm spectrum revealed a well-resolved vibrational progression for the ground state transition with a 550 cm^{-1} spacing. The 0–0 transition defined an ADE of 2.33 eV for B_5^-, which also represents the adiabatic electron affinity (EA) of the neutral B_5. The VDE was defined by
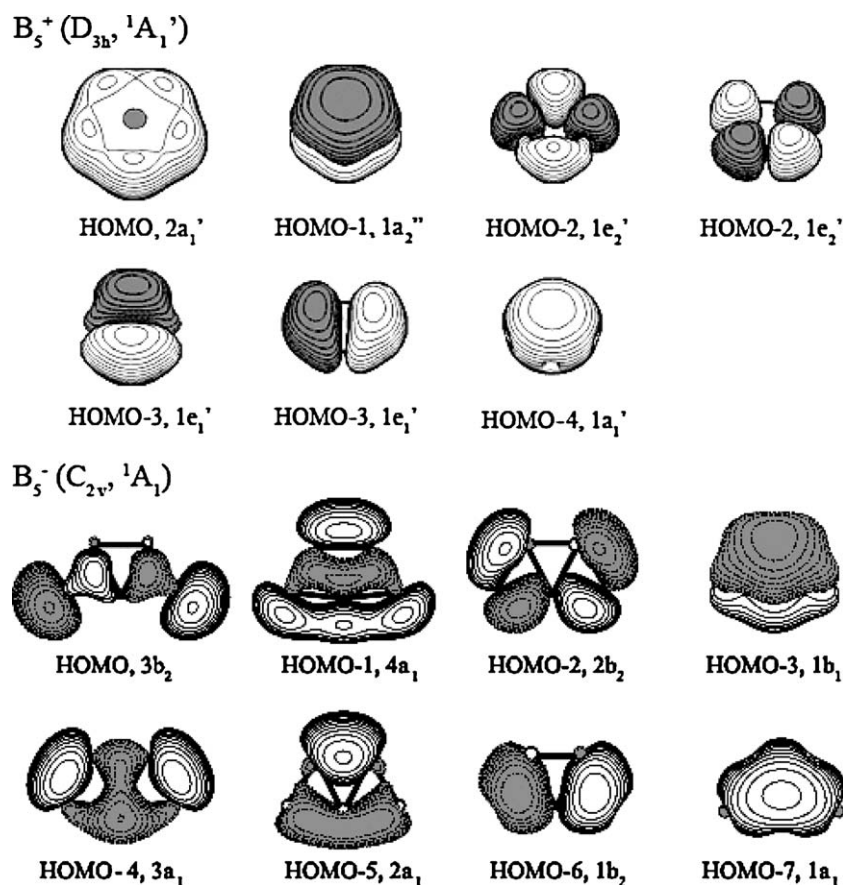
Fig. 15. Molecular orbital pictures of the: B_5^+ (D_{5h}, $^1A_1'$) and B_5^- (C_{2v}, $^1A_1$) clusters.

the $0 \to 1$ transition at 2.40 eV. The weak feature at 2.24 eV, labeled as HB in Fig. 16a, was assigned as a hot band transition, because the spacing between this feature and the 2.33 eV peak is much larger (680 cm^{-1}). The latter represents the vibrational frequency of the anion, indicating that a bonding electron was removed in the transition from the ground state of the anion to that of the neutral. At 266 nm, a relatively sharp and intense

band (A) was observed at 3.61 eV, as well as a weak feature (B) at higher binding energies. The A band displayed a short vibrational progression with an average spacing of 530 cm^{-1}, similar to that of the ground state band (X). The A band represents the first excited state of B_5. The short vibrational progression suggests that there is little geometric change between the anion ground state and the first excited state of the neutral.

Table 10
Calculated molecular properties of B_5^- (C_{2v}, $^1A_1$) [67]

	B3LYP/6-311+G*	CASSCF(8,8)/6-311+G*	RCCSD(T)/6-311+G*
E_{total} (a.u.)	−124.080875	−123.252276	−123.677914[a]
$R(B_1–B_{2,3})$ (Å)	1.738	1.752	1.765
$R(B_1–B_4)$ (Å)	1.614	1.632	1.639
$R(B_2–B_3)$ (Å)	1.577	1.557	1.607
$R(B_3–B_5)$ (Å)	1.579	1.583	1.617
$\omega_1(a_1)$ (cm^{-1})	1259	1320	1196
$\omega_2(a_1)$ (cm^{-1})	965	985	928
$\omega_3(a_1)$ (cm^{-1})	719[a]	738[a]	710[a]
$\omega_4(a_1)$ (cm^{-1})	638[a]	647[a]	593[a]
$\omega_5(a_2)$ (cm^{-1})	374	402	357
$\omega_6(b_1)$ (cm^{-1})	253	277	202
$\omega_7(b_2)$ (cm^{-1})	1067	1121	1082
$\omega_8(b_2)$ (cm^{-1})	998	994	929
$\omega_9(b_2)$ (cm^{-1})	582	637	556

[a] The anion ground state frequency was estimated to be 680 ± 60 cm^{-1} from the observed hot band transition (Fig. 16).
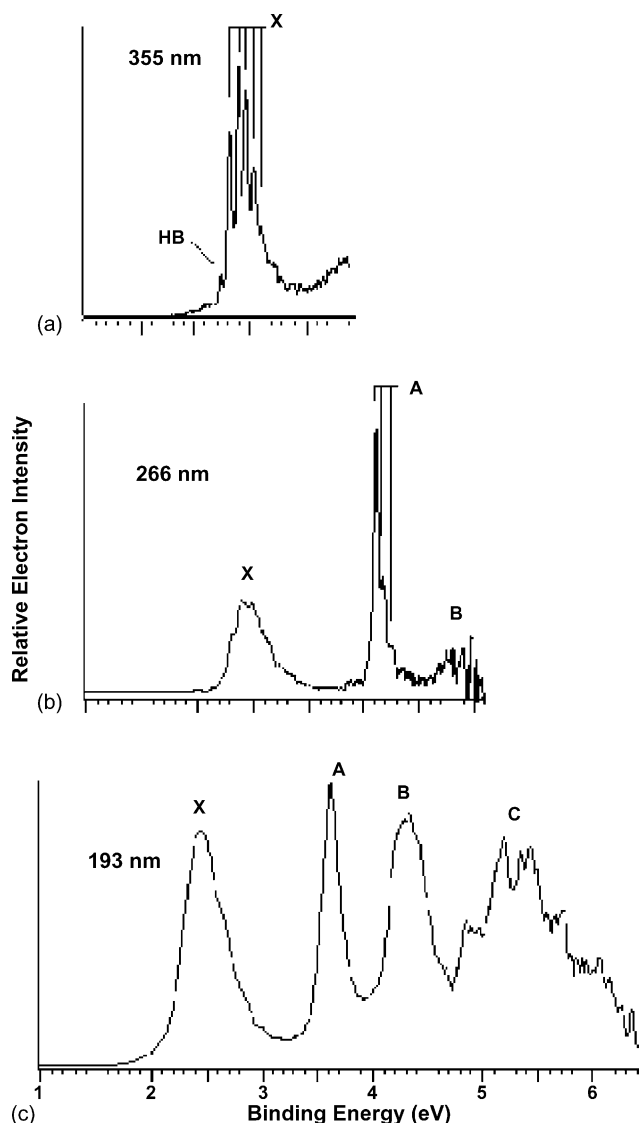
Fig. 16. Photoelectron spectra of B_5^- at: (a) 355 nm, (b) 266 nm (4.661 eV), and (c) 193 nm (6.424 eV). "HB" denotes a hot band transition. (Reprinted with permission from Ref. [67]. Copyright 2002 American Institute of Physics.)

In order to confirm the B_5^- (C_{2v}, $^1A_1$) global minimum structure, we calculated its VDEs by using various ab initio methods and compared them with the experimental results (Table 11).

An excellent agreement between experimental and theoretical VDEs lends considerable credence to the theoretically predicted B_5^- global minimum structure.

The calculated atomization energy (B_5^- (C_{2v}, $^1A_1$) → 4B (^2P) + B^- (^3P)) is 457 kcal/mol at CCSD(T)/6-311+G(2df)+ZPE [131].

Chemical bonding in B_5^- (Fig. 15b) can be easily understood if we start with the B_5^+ D_{5h} ($^1A_1'$) structure (Fig. 15a). The LUMO in B_5^+ D_{5h} ($^1A_1'$) is a part of the doubly degenerate $1e_1''$-MO which is a partially bonding/antibonding orbital related to the $1a_2''$-HOMO-1. These three MOs are a part of the set of five MOs formed by the $2p_z$-AOs of B and responsible for global π-bonding. However, it is LUMO + 1 ($3e_1'$-MO), which is partially occupied in the B_5^- global minimum structure. When only one of the pairs of doubly degenerate LUMO + 1 is occupied by either one electron, as it is in the neutral B_5, or by a pair of electrons as, it is in the singlet B_5^-, the Jahn–Teller distortion results in the C_{2v} ($^2B_2$) or C_{2v} ($^1A_1$) planar structures, respectively. The LUMO + 1 in B_5^+ belongs to a partially bonding/antibonding orbital related to the $2a_1'$-HOMO. These three MOs are a part of the set of five MOs formed by the 2p-radial AOs of B, and responsible for global σ-bonding. Thus, B_5^- has four electrons on globally σ-delocalized HOMO-1 ($4a_1$) and HOMO ($3b_2$), and two electrons on globally π-delocalized HOMO-3 ($1b_1$), making it a system with conflicting aromaticity (σ-antiaromatic and π-aromatic). The remaining molecular orbitals (HOMO-2, and HOMO-4 to HOMO-7) can be localized onto five peripheral 2c-2e B–B bonds in the putative B_5^{5+} cluster.

The neutral B_5 cluster possesses the same set of molecular orbitals as B_5^-, and the only difference is that the HOMO is singly occupied. The cluster is π-aromatic for the reason described above, and it can be described as partially σ-antiaromatic due to the presence of three electrons in the σ-radial subsystem.

In addition to the bare B_5^- cluster, Li and Jin [146] also reported a computational study on MB_5 (M = Li, Na, K, Rb, and Cs) and MB_5^+ (M = Be, Mg, Ca, and Sr) clusters using B3LYP and MP2 methods with the 6-311+G^* basis set. The structure of the B_5^- ligand in these systems retained its original planar C_{2v} shape. The metal ions were found to coordinate to one of the vertices of the cluster (the position of coordination varied depending on the metal atom).

Table 11
Calculated and observed photoelectron spectra of B_5^- [67]

Observed feature	ADE (eV)[a]	VDE (eV)[a]	Term value (eV)	Molecular orbital	VDE (theoretical)[b] ROVGF/6-311+G(2df) (eV)	VDE (theoretical) RCCSD(T)/6-311+G(2df) (eV)
X	2.33 (0.02)[c]	2.40 (0.02)	0	$3b_2$	2.36 (0.84)	2.45
A	3.61 (0.02)	3.61 (0.02)	1.28	$4a_1$	4.00 (0.78)	3.75
B	4.05 (0.05)	4.33 (0.05)	1.72	$2b_2$	4.51 (0.86)	
C		4.7–6.2		$1b_1$	5.25 (0.87)	5.22
				$3a_1$	5.78 (0.76)	

The anion ground state frequency was estimated to be 680 ± 60 cm^{-1} from the hot band transition (Fig. 16).

[a] The numbers in the parentheses represent the experimental uncertainty.

[b] The numbers in the parentheses indicate the pole strength, which characterizes the validity of the one-electron detachment picture.

[c] The adiabatic electron affinity of B_5.

3.5. Hexaatomic clusters: B_6, B_6^+, B_6^-, B_6^{2-}

3.5.1. B_6

There was a controversy in the literature about the structure of the global minimum of B_6. Initially, Whiteside [109] proposed the singlet pentagonal pyramid C_{5v} as the lowest isomer for B_6 (Fig. 17).

Niu et al. [124], Boustani [62], Li et al. [148] and Kato et al. [122] supported this finding using DFT/[10s5p1d/3s2p1d], SCF/3-21G and HF/6-311G*, B3LYP/6-311+G*, B3PW91/6-311+G*, and MP2/6-311+G* levels of theory, respectively. Ray et al. [116] reported the square bipyramid structure to be the most stable at the MP4/3-21G*//SCF/3-21G* level of theory. Ma et al. [149] found that the global minimum structure of B_6 is a triplet C_{2h} ^3A_u isomer (Fig. 17) at B3LYP/6-311+G(3df),

with the singlet pentagonal pyramid C_{5v} $^1A_1$ being the lowest isomer with the relative energy of just 1.8 kcal/mol. Guerini and Piquini [147,150] stated that the C_i ^3A_u structure is the global minimum structure.

In 2003 [68], we showed that the B_6 cluster has two nearly degenerate isomers (Fig. 17 and Table 12).

At the B3LYP/6-311+G* level of theory the planar triplet C_{2h} ^3A_u $(1a_g^2 1b_u^2 2a_g^2 2b_u^2 3a_g^2 1a_u^2 3b_u^2 4a_g^2 4b_u^1 1b_g^1)$ isomer was found to be the most stable. The pentagonal pyramid C_{5v} $^1A_1$ was found to be only 1.2 kcal/mol higher at the same level of theory. Our recent GEGA (B3LYP/3-21G) search confirmed that these two isomers are the lowest in energy with the C_{2h} ^3A_u being the most stable. However, at our highest CCSD(T)/6-311+G(2df)//B3LYP/6-311+G* level, the C_{5v} $^1A_1$ structure is the most stable, with the C_{2h} ^3A_u structure

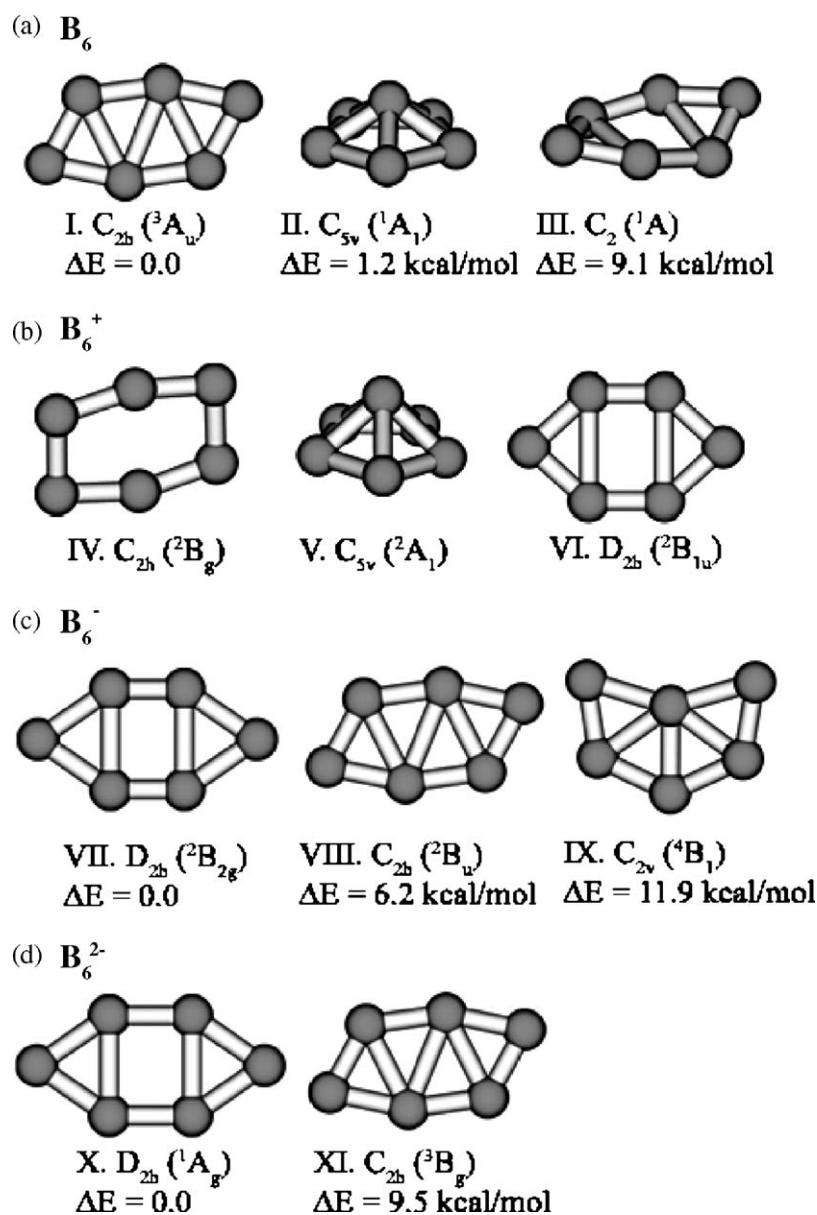Fig. 17. Lowest-energy structures of: (a) B_6, (b) B_6^+, (c) B_6^-, and (d) B_6^{2-}. Structures (a), (c), and (d) are given at the B3LYP/6-311+G* level. (Reprinted with permission from Ref. [68]. Copyright 2003 American Chemical Society.) Structures (b) are obtained at different levels by different groups, so the relative energies are not shown. All species are minima on the potential energy surface.

Table 12
Calculated molecular properties of the alternative structures of B_6 (B3LYP/6-311+G* level of theory) [68]

Cluster	B_6, C_{2h}, ^3A_u	B_6, C_{5v}, $^1A_1$	B_6, C_2, ^1A
E_{total} (a.u.)	−148.82943	−148.82749	−148.81492
Geometry	$R(B_1–B_2) = 1.516$ Å	$R(B_1–B_2) = 1.659$ Å	$R(B_1–B_3) = 1.571$ Å
	$R(B_2–B_3) = 1.845$ Å	$R(B_2–B_3) = 1.610$ Å	$R(B_1–B_4) = 1.548$ Å
	$R(B_3–B_4) = 2.012$ Å	$R(B_2–B_4) = 2.604$ Å	$R(B_3–B_4) = 1.826$ Å
	$R(B_2–B_4) = 1.583$ Å	$\angle B_2–B_1–B_4 = 103.4°$	$R(B_3–B_6) = 1.580$ Å
	$R(B_1–B_3) = 1.579$ Å	$\angle B_2–B_1–B_3 = 58.0°$	$\angle B_1–B_4–B_5–B_2 = 35.9°$
Frequencies (cm^{-1})	$\omega_1(a_g) = 1390$	$\omega_1(a_1) = 1047$	$\omega_1(a) = 1292$
	$\omega_2(a_g) = 1081$	$\omega_2(a_1) = 649$	$\omega_2(a) = 1072$
	$\omega_3(a_g) = 807$	$\omega_3(e_1) = 1079$	$\omega_3(a) = 838$
	$\omega_4(a_g) = 517^a$	$\omega_4(e_1) = 814$	$\omega_4(a) = 556^a$
	$\omega_5(a_g) = 264$	$\omega_5(e_2) = 1112$	$\omega_5(a) = 316$
	$\omega_6(b_g) = 321$	$\omega_6(e_2) = 591$	$\omega_6(a) = 203$
	$\omega_7(b_u) = 1329$	$\omega_7(e_2) = 336$	$\omega_7(a) = 171$
	$\omega_8(b_u) = 1081$		$\omega_8(b) = 1349$
	$\omega_9(b_u) = 661$		$\omega_9(b) = 1098$
	$\omega_{10}(b_u) = 516$		$\omega_{10}(b) = 708$
	$\omega_{11}(a_u) = 332$		$\omega_{11}(b) = 567$
	$\omega_{12}(a_u) = 238$		$\omega_{12}(b) = 411$

[a] $\omega = 510 \pm 40$ cm^{-1} was determined from the PES of B_6^- [68].

being 7.2 kcal/mol higher in energy. Thus, we believe that we established with certainty that the C_{5v} $^1A_1$ structure is the global minimum structure of B_6.

3.5.2. B_6^+

There is also a controversy in the literature about the structure of the global minimum of B_6^+. The highest level of theory employed by Li et al. [148] for finding the lowest energy structure of B_6^+ was MP2/6-311G*. They claimed that B_6^+ has the C_{2h} ^2B_g global minimum structure (Fig. 17) with the lowest excited local minimum a square bipyramid structure D_{4h}. Ma et al. [149] reported the D_{2h} $^2B_{1u}$ structure to be the lowest in their B3LYP/6-31+G* calculations. According to Niu et al. [124] the B_6^+ cluster has a perfect hexagonal shape. Kato et al. [122] reported the B_6^+ cluster has a C_2 (^2B) symmetry. Ray et al. [116] reported the square pyramid to be the most stable. Certainly more accurate calculations are needed to determine the global minimum structure with certainty.

3.5.3. B_6^- and its photoelectron spectra

We predicted [68] the most stable structure of B_6^- to be the planar D_{2h}, $^2B_{2g}$ $(1a_g^2 1b_{1u}^2 1b_{2u}^2 2a_g^2 1b_{3g}^2 1b_{3u}^2 3a_g^2 2b_{1u}^2 2b_{2u}^2 1b_{2g}^1)$ structure (Fig. 17 and Table 13).

Our follow-up GEGA (B3LYP/3-21G) search confirmed that this structure is the most stable one [135]. The lowest isomer, C_{2h}, ^2B_u $(1a_g^2 1b_u^2 2a_g^2 2b_u^2 3a_g^2 1a_u^2 3b_u^2 4a_g^2 1b_g^2 4b_u^1)$ was found to be 6.2 kcal/mol higher in energy (B3LYP/6-311+G*). Other structures were found to be more than 10 kcal/mol higher. The applicability of the one-electron approximation was tested using CASSCF(9,8)/6-311+G* calculations. For the most stable structure we found that even though the Hartree–Fock configuration is still dominant ($C_{HF} = 0.885$), the second configuration $(1a_g^2 1b_{1u}^2 1b_{2u}^2 2a_g^2 1b_{3g}^2 1b_{3u}^2 3a_g^2 2b_{1u}^0 2b_{2u}^2 1b_{2g}^1 4a_g^2)$ contributes substantially to the CASSCF wave function ($C_{14} = 0.360$, where the coefficient C_i represents the contribution of the ith excited

configuration). Ma et al. [149] confirmed the D_{2h}, $^2B_{2g}$ global minimum structure, but Li et al. [148] apparently missed the global minimum structure.

The PES spectra of B_6^- were first obtained by Zhai and co-workers, as shown in Fig. 18 at three different photon energies [68].

Vibrational structures were partially resolved in the bands X and A at 355 nm (Fig. 18a), and band D at 193 nm (Fig. 18c). Both bands B and C were broad and might have contained unresolved electronic transitions. Higher binding energy transitions may exist beyond 5.4 eV, but this part of the spectrum at 193 nm had poor signal-to-noise ratio and was not well resolved. At 355 nm (Fig. 18a), only bands X and A were observed. The ground state transition (X) contained a short vibrational progression with a vibrational spacing of 510 cm^{-1}. Higher vibrational transitions of the X band were apparently overlapped with band A.

Table 13
Calculated molecular properties of the D_{2h} ($^2B_{2g}$) structure of B_6^- [68]

	B3LYP/6-311+G*	CASSCF(9,8)/6-311+G*
E_{total} (a.u.)	−148.926468	−147.92236
$R(B_{1–3,4})$ (Å)	1.539	1.557
$R(B_3–B_4)$ (Å)	1.807	1.805
$R(B_3–B_6)$ (Å)	1.615	1.611
$\omega_1(a_g)$ (cm^{-1})	1343	1346
$\omega_2(a_g)$ (cm^{-1})	816	843
$\omega_3(a_g)$ (cm^{-1})	626	691
$\omega_4(a_u)$ (cm^{-1})	298	341
$\omega_5(b_{2g})$ (cm^{-1})	396	455
$\omega_6(b_{3g})$ (cm^{-1})	1074	1007
$\omega_7(b_{3g})$ (cm^{-1})	229	191
$\omega_8(b_{1u})$ (cm^{-1})	1165	1174
$\omega_9(b_{1u})$ (cm^{-1})	676	720
$\omega_{10}(b_{2u})$ (cm^{-1})	1333	1414
$\omega_{11}(b_{2u})$ (cm^{-1})	659	707
$\omega_9(b_{3u})$ (cm^{-1})	206	250

Fig. 18. Photoelectron spectra of B_6^- at: (a) 355 nm (3.496 eV), (b) 266 nm (4.661 eV), and (c) 193 nm (6.424 eV). (Reprinted with permission from Ref [68]. Copyright 2003 American Chemical Society.)

Since B_6^- is an open-shell system, transitions from the doublet state of the anion both to the singlet and to the triplet states were possible [68]. The comparison of experimental and theoretical (obtained at three different levels of theory) spectra is given in Table 14 [68].

The theoretical VDEs from the D_{2h} global minimum of B_6^- are in excellent agreement with the experimental data, lending credence for this structure as the global minimum.

3.5.4. B_6^{2-}

Fowler and co-workers [151] were first to predict the D_{2h} ^1A_g $(1a_g^2 1b_{1u}^2 1b_{2u}^2 2a_g^2 1b_{3g}^2 1b_{3u}^2 3a_g^2 2b_{1u}^2 2b_{2u}^2 1b_{2g}^2)$ structure for the B_6^{2-} dianion. This structure was confirmed by Ma et al. [149] and Alexandrova et al. [68].

The chemical bonding in the B_6^{2-} cluster is intriguing. The molecular orbital pictures of the D_{2h} global minimum are given in Fig. 19, which also includes the valence MOs of the B_3^- cluster. The MO pictures of the B_6^- anion are identical to those of the B_6^{2-}, except that it is an open shell system with one electron occupying the $1b_{2g}$ HOMO. The elongated shape of the D_{2h} B_6^{2-} (and B_6^-) ground state (Fig. 17) can be understood in terms of the fusion of two doubly aromatic B_3^- fragments [68]. In addition to the MOs described in Section 3.2.3, the LUMO in B_3^- is a degenerate pair of σ^*-MOs ($2e'$, Fig. 19). The MOs of B_6^- and B_6^{2-} can be interpreted as combinations of the MOs of two B_3^- fragments, as shown in Table 15.

The NBO analysis performed on a B_6^{6+} cluster, with only the HOMO-1 and HOMO-5 to HOMO-9 occupied, reveals the existence of the six classical 2c-2e B–B bonds on the periphery of the distorted hexagon. These MOs cannot be responsible for its distorted shape.

The remaining four MOs (HOMO, HOMO-2 to HOMO-4) participate in global bonding in the B_6^- and B_6^{2-} clusters. The HOMO-2 ($2b_{1u}$) and HOMO-3 ($3a_g$) are σ-radial molecular orbitals, with the HOMO-3 being completely bonding, and the HOMO-2 having one nodal plane. The species clearly contains four σ-electrons, leading to antiaromaticity, and making B_6^- and B_6^{2-} σ-antiaromatic.

Table 14
Observed and calculated photoelectron spectra of B_6^- [68]

Experiment				Theory			
Feature	ADE (eV)[a]	VDE (eV)[a]	Vibrational frequency (cm^{-1})	Final state	UOVGF/ 6-311+G(2df)	RCCSD(T)/ 6-311+G(2df)	EOM-RCCSD(T)/ 6-311+G(2df)
X	3.01 (0.04)	3.01 (0.04)	510 (40)	$^3B_{3u}$ $(1b_{3u}^2 3a_g^2 2b_{1u}^2 2b_{2u}^1 1b_{2g}^1)$	3.19 (0.86)[b]	2.86	
A	3.17 (0.04)	3.17 (0.04)	530 (40)	^1A_g $(1b_{3u}^2 3a_g^2 2b_{1u}^2 2b_{2u}^2 1b_{2g}^0)$	3.05 (0.89)	2.90	
B		3.55 (0.05)		$^1B_{3u}$ $(1b_{3u}^2 3a_g^2 2b_{1u}^2 2b_{2u}^1 1b_{2g}^1)$			3.30
				^3A_u $(1b_{3u}^2 3a_g^2 2b_{1u}^1 2b_{2u}^2 1b_{2g}^1)$	4.90 (0.81)	4.06	
C	4.13 (0.06)	4.35 (0.05)		^1A_u $(1b_{3u}^2 3a_g^2 2b_{1u}^1 2b_{2u}^2 1b_{2g}^1)$			4.58
				$^3B_{2g}$ $(1b_{3u}^2 3a_g^1 2b_{1u}^2 2b_{2u}^2 1b_{2g}^1)$	4.45 (0.89)	4.26	
D	4.95 (0.03)	5.04 (0.03)	720 (30)	$^1B_{2g}$ $(1b_{3u}^2 3a_g^1 2b_{1u}^2 2b_{2u}^2 1b_{2g}^1)$			4.75
				$^3B_{1u}$ $(1b_{3u}^2 3a_g^2 2b_{1u}^2 2b_{2u}^2 1b_{2g}^1)$	4.68 (0.90)	4.75	
				$^1B_{1u}$ $(1b_{3u}^1 3a_g^2 2b_{1u}^2 2b_{2u}^2 1b_{2g}^1)$			5.82

[a] The numbers in the parentheses represent the experimental uncertainty.

[b] The numbers in the parentheses indicate the pole strength, which characterizes the validity of the one-electron detachment picture in UOVGF.
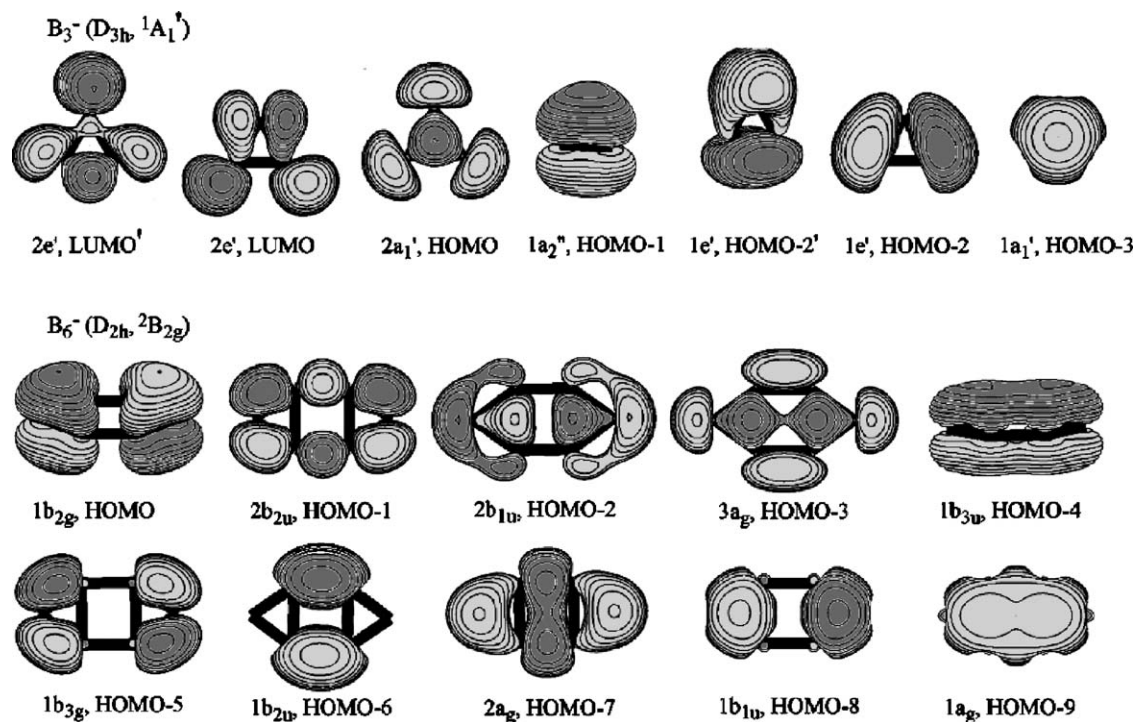
Fig. 19. Molecular orbital pictures of B_3^- (D_{3h}, $^1A_1'$) and B_6^- (D_{2h}, $^2B_{2g}$) clusters. The order of the orbitals given in accordance with R(U)OVGF/6-311+G(2df) calculations. (Reprinted with permission from Ref [68]. Copyright 2003 American Chemical Society.)

In addition, the delocalized HOMO-4 ($1b_{3u}$) and HOMO ($1b_{2g}$) are π-MOs. The HOMO-4 is completely bonding, and the HOMO is a partially bonding orbital. Thus, we can assign the B_6^{2-} as a doubly (σ- and π-) antiaromatic system. The global minimum of B_6^- is partially π-antiaromatic system because it has three π-electrons, but it, overall, can be also assigned as a doubly (σ- and π-) antiaromatic system.

Current density maps could provide us an important clue to the chemical bonding in clusters and such maps have been recently reported for B_6 and B_6^{2-} species [68]. The electronic configurations of the neutral, monoanion, and dianion of B_6 differ only in the occupation of the π-orbital of b_{2g} symmetry, which is the HOMO of both B_6^- and B_6^{2-} at this geometry.

Computed current density maps for the two closed-shell species (B_6 and B_6^{2-}) are shown in Fig. 20. In each case, the total

Table 15
Molecular orbitals of B_6^- (D_{2h}, $^2B_{2g}$) expressed in terms of molecular orbitals of B_3^- (D_{3h}, $^1A_1'$)

MOs of B_6^-	MOs of B_3^-
HOMO ($1b_{2g}$)	HOMO-1 ($1a_2''$) − HOMO-1 ($1a_2''$)
HOMO-1 ($2b_{2u}$)	LUMO ($2e'$) + LUMO ($2e'$)
HOMO-2 ($2b_{1u}$)	HOMO-2' ($1e'$) − HOMO-2' ($1e'$)
HOMO-3 ($3a_g$)	HOMO ($2a_1'$) + HOMO ($2a_1'$)
HOMO-4 ($1b_{3u}$)	HOMO-1 ($1a_2''$) + HOMO-1 ($1a_2''$)
HOMO-5 ($1b_{3g}$)	HOMO-2 ($1e'$) − HOMO-2 ($1e'$)
HOMO-6 ($1b_{2u}$)	HOMO-2 ($1e'$) + HOMO-2 ($1e'$)
HOMO-7 ($2a_g$)	HOMO-2' ($1e'$) + HOMO-2' ($1e'$)
HOMO-8 ($1b_{1u}$)	HOMO-3 ($1a_1'$) − HOMO-3 ($1a_1'$)
HOMO-9 ($1a_g$)	HOMO-3 ($1a_1'$) + HOMO-3 ($1a_1'$)

Refer to Fig. 19 for the orbitals.

($\sigma + \pi$), σ-, and π-only contributions are plotted at the height of 1 bohr (0.529 Å) above the molecular plane. In the dianion, the total current is a superposition of a paramagnetic π ring current confined to the inner square of B atoms, and a set of σ paramagnetic vortices localized on the B centers. In the neutral species, the $1b_{2g}$ orbital is empty, and the HOMO π current is absent. The total map for B_6 is now essentially identical with its σ-only map, and is little changed from the σ-only map for the dianion. A small diamagnetic π current is also contributed in B_6 by the two remaining π-electrons, which occupy the low-lying $1b_{3u}$ orbital.

These observations have a ready interpretation in the ipsocentric model, in terms of the orbital contributions. For a planar system subjected to a perpendicular magnetic field the induced current density can be partitioned rigorously into a sum over orbital excitations [152], each of which corresponds either to an in-plane translational transition (producing a diamagnetic current) or to an in-plane rotational transition (producing a paramagnetic current). Both types of transition preserve σ–π separation.

The large π current in the dianion arises from the rotationally allowed (and therefore paratropic) transitions between the occupied $1b_{2g}$ HOMO and the empty $1b_{1g}$ orbital that would form the other half of a $\Lambda = 1$ pair in the ideal six-membered ring [153]. The σ currents result from a combination of contributions from HOMO-1 and lower-lying orbitals, and originate from transitions to virtual orbitals that are related by local rotations [151–153]. Likewise, in neutral B_6, the loss of the HOMO π pair removes the main contribution to the π current, leaving the σ current essentially undisturbed, but opening up the new translationally allowed $\pi \rightarrow \pi^*$ channel from which the weak diamagnetic current arises.

Fig. 20. Computed current density maps at $1a_0$ above the molecular plane for dianionic (left) and neutral (right) D_{2h} hexa-boron rings at the geometry of the monoanion. Diamagnetic circulation is shown anticlockwise, paramagnetic circulation clockwise. Arrows indicate the projection of the current density vector in the plotting plane. (a) All-electron ($\sigma + \pi$) current density, (b) total π current density, and (c) total σ current density. (Reprinted with permission from Ref. [68]. Copyright 2003 American Chemical Society.)

In open-shell systems, the allowed translational and rotational transitions describing the first-order response of the orbital current density to the external field are between spin-orbitals with the same component of spin. The ipsocentric model for the monoanion therefore predicts that this species will have essentially the same σ current as in B_6 and B_6^{2-}, plus a significant HOMO π current of the same kind as in B_6^{2-}, but with reduction in intensity as only one π-electron is now participating, plus a small diamagnetic b_{3u} π current as in B_6, again reduced as only one 'hole' is available in the b_{2g} SOMO. Hence, B_6^- is predicted to have a paramagnetic ring current dominated by its least-bound π-electron, and therefore to be antiaromatic by the magnetic criterion. Thus, this joint MO and ring-current anal-

ysis left no doubt that the B_6^- and B_6^{2-} clusters are doubly antiaromatic.

Ma et al. [149] probed aromaticity in B_6, B_6^+, B_6^-, and B_6^{2-} by calculating the NICS indices. They stated that, according to the NICS index, the neutral B_6 and anionic B_6^- clusters are nonaromatic, the B_6^+ cation is aromatic, and the B_6^{2-} dianion is antiaromatic, which disagrees with our assignment of antiaromaticity to B_6^-.

From the MO analysis of B_6^{2-}, one can predict that if four electrons will be deleted, two from the π-antibonding HOMO ($1b_{2g}$) and two from the σ-antibonding HOMO-2 ($2b_{1u}$), the resulting B_6^{2+} dication may acquire double aromatic character and the high symmetry D_{6h} ($^1A_{1g}$) structure. Indeed ab initio
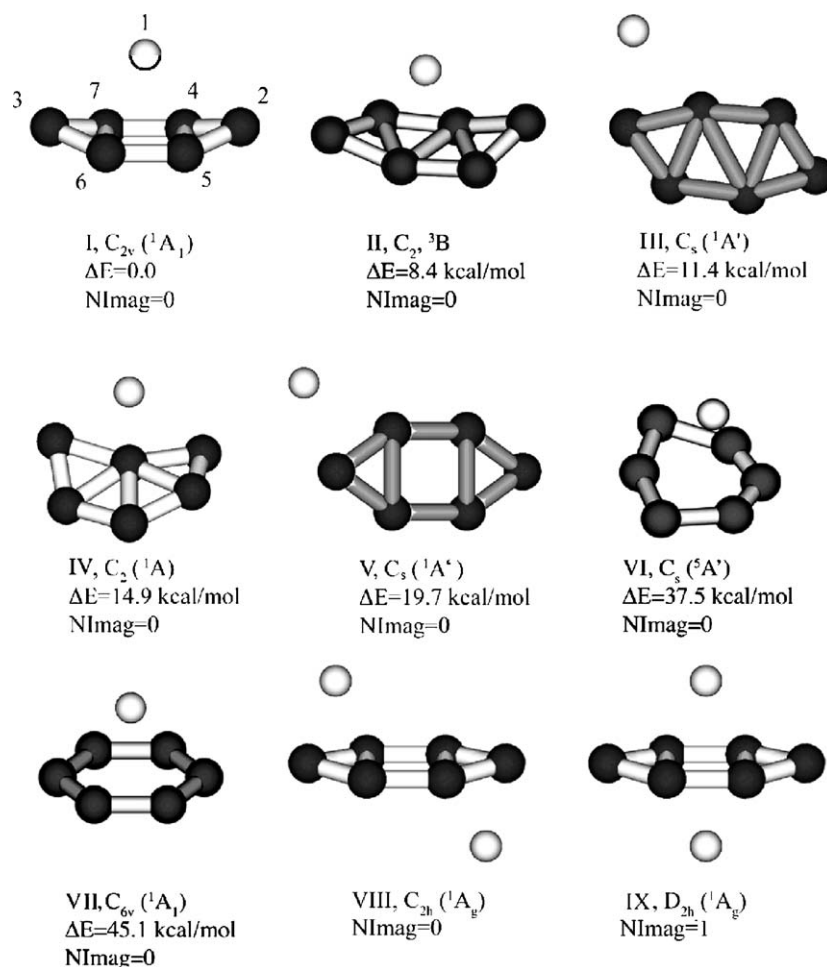
Fig. 21. Low-lying isomers of the LiB_6^- and Li_2B_6 species along with their relative energies at the B3LYP/6-311+G* level of theory. (Reprinted with permission from Ref. [154]. Copyright 2005 American Institute of Physics.)

calculations at different levels of theory confirmed that the D_{6h} ($^1A_{1g}$) structure is a true minimum.

3.5.5. LiB_6^-, Li_2B_6, and MB_6 (M = Be, Mg, Ca, and Sr)

We recently reported a joint ab initio and experimental study on the LiB_6^- cluster, which is the first example of a salt-like $Li^+B_6^{2-}$ anion [154]. We performed the GEGA (B3LYP/3-21G) search for the global minimum structure and then refined low-lying structures at higher levels of theory. The lowest energy structures of this species are given in Fig. 21.

The D_{2h} (^1A_g) structure of B_6^{2-} is clearly preserved in the C_{2v} ($^1A_1$) global minimum structure of LiB_6^- complex with only minor distortions. The lowest LiB_6^- excited isomer was found to have the triplet C_2 ^3B structure (Fig. 21) which is 8.4 kcal/mol (B3LYP/6-311+G*) higher in energy. From among other found local minima we would like to mention a highly symmetric C_{6v} $^1A_1$ isomer, which, however, is 45.1 kcal/mol higher in energy than the global minimum. We recorded the photoelectron spectrum of the LiB_6^- anion at three photon energies (Fig. 22 and Table 16).

A good agreement between the theoretically predicted and experimental VDEs up to 4.2 eV was observed. However, the higher binding energy features D and E did not seem to agree well with calculated detachment channels. This was most likely

Table 16
Calculated and experimental VDEs for LiB_6^- [154]

Feature	VDE (eV)[a]	MO	TD-B3LYP/6-311+G(2df)	ROVGF/6-311+G(2df)[b]	RCCSD(T)/6-311+G(2df)
X	2.60 (0.03)	$3b_2$	2.36	2.57 (0.86)	2.71
A	2.97 (0.03)	$2b_2$	3.06	3.12 (0.87)	
B	3.76 (0.05)	$2b_1$	3.92	3.78 (0.86)	3.68
C	4.00 (0.05)	$4a_1$	4.04	4.18 (0.82)	4.08
D	4.56 (0.02)	$1a_2$	5.21	5.41 (0.85)	5.22
E	4.79 (0.03)				

[a] The numbers in the parentheses represent the experimental uncertainty.
[b] The numbers in the parentheses indicate the pole strength, which characterizes the validity of the one-electron detachment picture in UOVGF.
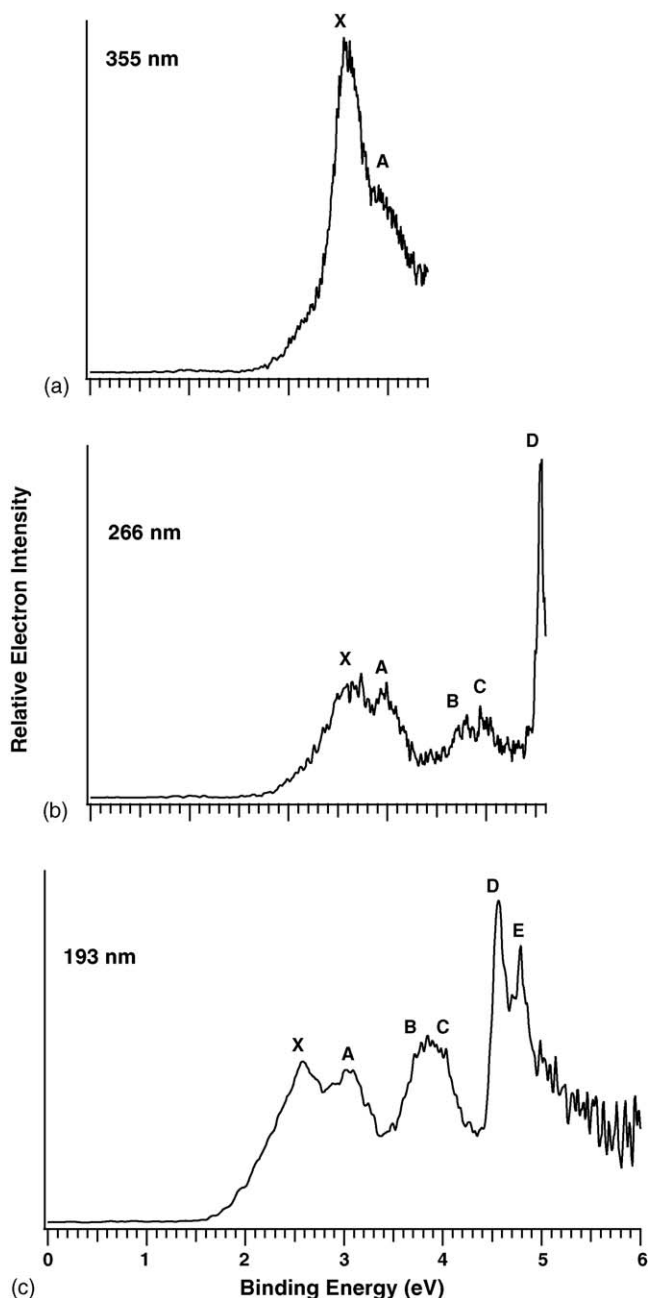
Fig. 22. Photoelectron spectra of LiB_6^- at: (a) 355 nm (3.496 eV), (b) 266 nm (4.661 eV), and (c) 193 nm (6.424 eV). (Reprinted with permission from Ref. [154]. Copyright 2005 American Institute of Physics.)
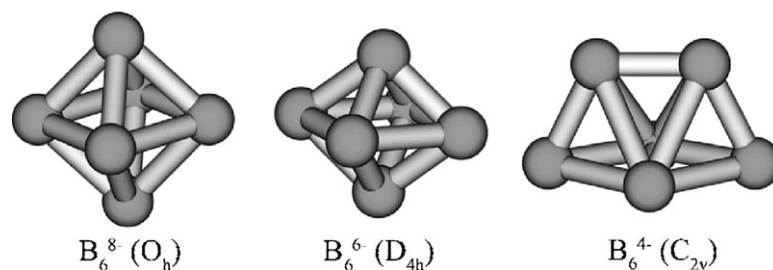
due to the fact that the methods based on the one-electron approximation used in this work deteriorate at high binding energy. Thus, on the basis of good agreement for four lowest VDEs we concluded that overall agreement between theory and experiment is satisfying, lending credence to the C_{2v} $^1A_1$ global minimum structure of LiB_6^-. The chemical bonding pattern of the global minimum species remains almost identical to that of the bare B_6^{2-} cluster. The doubly antiaromatic character of the species is preserved [154].

However, although the B_6^{2-} cluster is globally doubly antiaromatic, one can see from the MOs (Fig. 19 and Table 15) that it can be viewed as composed of two aromatic B_3^- clusters. Indeed, $1b_{2g}$-HOMO and $1b_{3u}$-HOMO-4 are a π-bonding and π-antibonding pair of the π-MO in B_3^-. Thus, π-MOs do not contribute to chemical bonding between two B_3^- groups. That allows us to speculate that π-MOs in B_6^{2-} can be considered as localized over two triangular areas in B_6^{2-}, i.e., we have an island aromaticity in B_6^{2-}. In order to test that, we optimized the geometry for the neutral Li_2B_6 cluster. The D_{2h} (^1A_g) structure (Fig. 21), containing one Li^+ cation above and another Li^+ below the plane of B_6^{2-} dianion, was found to be a saddle point on the potential energy surface. Geometry optimization, following the normal mode of the imaginary frequency, led to the C_{2h} (^1A_g) structure with two Li^+ ions located above and below the B_3^- triangular areas in B_6^{2-}. These results confirmed the presence of the π-island aromaticity in the overall doubly antiaromatic system.

Li and Jin recently reported a theoretical study of a series of MB_6 (M = Be, Mg, Ca, and Sr) clusters [155]. They concluded that BeB_6 and MgB_6 clusters have half-sandwich C_{6v} $^1A_1$ pyramidal structures with the M^{2+} cation interacting with the planar hexagonal B_6^{2-} dianion, whereas the two other CaB_6 (C_1, ^1A) and SrB_6 (C_s, $^1A'$) clusters possess quasi-pyramidal structure with the M^{2+} cation interacting with a chair-like B_6^{2-} dianion. Our calculations at the B3LYP/6-311+G* level of theory showed, however, that these structures are *not* the most stable structures for the corresponding clusters. The structure with the M^{2+} cation coordinated to the D_{2h} ^1A_g type structure of B_6^{2-} is significantly more stable, which is consistent with our results for LiB_6^-.

The B_6^{z-} systems ($z = 4, 6, 8$) with assumed six-vertex delta-hedron structure were studied computationally by King et al. [156]. B_6^{8-} was reported to have an octahedral structure, B_6^{6-} had a D_{4h} bipyramidal structure, and B_6^{4-} was a C_{2v} bicapped tetrahedron (Fig. 23).

The B_6^{8-} octahedral species possesses 14 skeletal electrons corresponding to $2n + 2$ skeletal electrons required for the octa-

Fig. 23. Structures of B_6^{8-}, B_6^{6-}, and B_6^{4-}. (Reprinted with permission from Ref. [156]. Copyright 2001 American Chemical Society.)

hedron ($n = 6$) to be stable. In addition, there are six globally binding MOs. Upon two-electron oxidation of B_6^{8-}, the triply degenerate HOMO becomes partially populated, leading to a Jahn–Teller distortion toward D_{4h} symmetry. Further oxidation (to B_6^{4-}) reduces the symmetry even more, as the HOMO of B_6^{4-} is the only orbital from the initially triply degenerate set remaining occupied [156].

3.6. Heptaatomic clusters: B_7, B_7^+, B_7^-

3.6.1. B_7^+

The global minimum structure of the cationic B_7^+ cluster was reported to be a C_{6v} $^1A_1$ ($1a_1^2 1e_1^4 1e_2^4 2a_1^2 1b_1^2 3a_1^2 2e_1^4$) pyramid with rather small deviation from planarity (Fig. 24 and Table 17) [122,125,127–129,135,157].

Ray et al. [116] reported that the pentagonal bipyramid structure is the most stable on the potential energy surface of B_7^+, but this claim is apparently wrong. Few other local minimum isomers were identified by Li et al. [157].

Molecular orbital analysis helps to understand why B_7^+ has the C_{6v} $^1A_1$ structure. To make the interpretation simpler, let us consider MOs in the D_{6h} $^1A_{1g}$ structure (Fig. 25), where separation of MOs into σ- and π- can be easily made.

The set of six MOs (HOMO-2, HOMO-4, HOMO-4′, HOMO-5, HOMO-5′, and HOMO-6) is responsible for the peripheral bonding and can be localized into six 2c-2e B–B bonds. The HOMO-3 is formed by $2p_z$-AOs, and it is responsible for the global π-bonding. The HOMO, HOMO′, and HOMO-1 are composed of 2p-radial AOs, and they are responsible for global σ-bonding in the B_7^+ cluster. Thus, B_7^+ in the D_{6h} $^1A_{1g}$ configuration is a doubly (σ- and π-) aromatic system with 2π- and 6σ-electrons. However, the central cavity in the B_6 hexagon is too small to favorably accommodate a central boron atom, and, therefore, a C_{6v} $^1A_1$ pyramidal structure corresponds to the global minimum. While in the pyramidal structure σ- and π-MOs are now mixed, we believe that the bonding picture we developed for the D_{6h} $^1A_{1g}$ structure is still qualitatively valid, because the deviation from planarity is not that big (the central boron atom is about 0.72 Å above the plane).
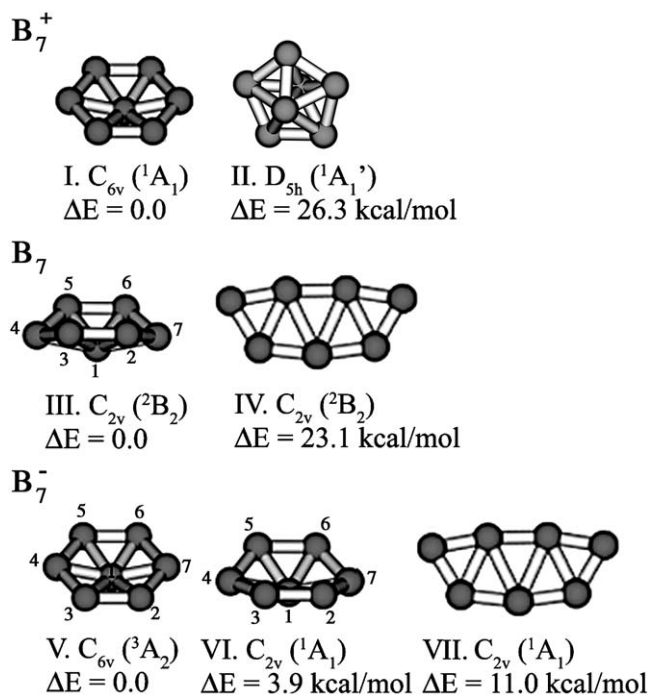
Fig. 24. Lowest-energy structures of the heptaatomic pure-boron clusters. Computation of B_7^+ is done at the B3LYP/6-31G* level of theory. Structures of B_7 and B_7 are shown at the B3LYP/6-311+G* level. (Reprinted with permission from Ref. [69]. Copyright 2004 American Chemical Society.)

From among alternative structures of B_7^+ we would like to discuss the cyclic structure D_{7h} $^3A_2'$. It was found to be a local minimum and also doubly aromatic system, but it is 62.4 kcal/mol (at B3LYP/6-311+G*) higher in energy than the C_{6v} $^1A_1$ pyramidal global minimum structure. The question is, why the doubly aromatic D_{7h} $^3A_1'$ structure is significantly less stable than the pyramidal C_{6v} $^3A_2'$ structure. Our explanation is that, when the number of atoms in the cyclic structure is increasing, the electrostatic field from the screened boron nuclei is decreasing, and, in the case of boron clusters at $n = 7$ the presence of the central boron atom starts to be essential in order to stabilize the delocalized density at the center of cluster, com-

Table 17
Molecular properties of B_7^+ (C_{6v}, $^1A_1$) global minimum structure

	B3LYP/6-311+G*[a]	BPW91/6-311+G*[b]	MP2/6-311+G*[b]
E_{total} (a.u.)	−173.41787	−173.3289	−172.7873
$R(B_1–B_{2–7})$ (Å)	1.739	1.743	1.767
$\angle B_2–B_1–B_3$ (°)	54.2	54.1	53.9
$\omega_1(a_1)$ (cm^{-1})	921	[c]	904
$\omega_2(a_1)$ (cm^{-1})	499	[c]	515
$\omega_3(b_1)$ (cm^{-1})	1290	[c]	1313
$\omega_4(b_2)$ (cm^{-1})	612	[c]	578
$\omega_5(b_2)$ (cm^{-1})	443	[c]	401
$\omega_6(e_1)$ (cm^{-1})	997	[c]	1006
$\omega_7(e_1)$ (cm^{-1})	805	[c]	783
$\omega_8(e_2)$ (cm^{-1})	1243	[c]	1226
$\omega_9(e_2)$ (cm^{-1})	528	[c]	512
$\omega_{10}(e_2)$ (cm^{-1})	317	[c]	308

[a] Data from [131].
[b] Data from [158].
[c] Frequencies were not reported at this level of theory.

B$_7^+$ (C_{6v}, $^1A_1$)	LUMO, 3e$_1$	LUMO', 3e$_1$	HOMO, 2e$_1$
B$_7$ (C_{2v}, $^2B_2$)	LUMO, 4b$_1$	HOMO, 3b$_2$	HOMO-2, 2b$_2$
B$_7^-$ (C_{6v}, $^3A_2$)	HOMO, 3e$_1$	HOMO', 3e$_1$	HOMO-1, 2e$_1$
B$_7^-$ (C_{2v}, $^1A_1$)	LUMO, 4b$_1$	HOMO, 3b$_2$	HOMO-1, 2b$_2$

B$_7^+$ (C_{6v}, $^1A_1$)	HOMO', 2e$_1$	HOMO-1, 3a$_1$	HOMO-2, 1b$_1$
B$_7$ (C_{2v}, $^2B_2$)	HOMO-1, 3b$_1$	HOMO-4, 4a$_1$	HOMO-3, 2b$_1$
B$_7^-$ (C_{6v}, $^3A_2$)	HOMO-1', 2e$_1$	HOMO-2, 3a$_1$	HOMO-3, 1b$_1$
B$_7^-$ (C_{2v}, $^1A_1$)	HOMO-2, 3b$_1$	HOMO-3, 4a$_1$	HOMO-4, 2b$_1$

B$_7^+$ (C_{6v}, $^1A_1$)	HOMO-3, 2a$_1$	HOMO-4, 1e$_2$	HOMO-4', 1e$_2$
B$_7$ (C_{2v}, $^2B_2$)	HOMO-5, 3a$_1$	HOMO-7, 2a$_1$	HOMO-6, 1a$_2$
B$_7^-$ (C_{6v}, $^3A_2$)	HOMO-4, 2a$_1$	HOMO-5, 1e$_2$	HOMO-5', 1e$_2$
B$_7^-$ (C_{2v}, $^1A_1$)	HOMO-5, 3a$_1$	HOMO-6, 2a$_1$	HOMO-7, 1a$_2$

B$_7^+$ (C_{6v}, $^1A_1$)	HOMO-5, 1e$_1$	HOMO-5', 1e$_1$	HOMO-6, 1a$_1$
B$_7$ (C_{2v}, $^2B_2$)	HOMO-8, 1b$_1$	HOMO-9, 1b$_2$	HOMO-10, 1a$_1$
B$_7^-$ (C_{6v}, $^3A_2$)	HOMO-6, 1e$_1$	HOMO-6', 1e$_1$	HOMO-7, 1a$_1$
B$_7^-$ (C_{2v}, $^1A_1$)	HOMO-8, 1b$_1$	HOMO-9, 1b$_2$	HOMO-10, 1a$_1$

Fig. 25. Molecular orbital picture of B$_7^+$ (C_{6v}, $^1A_1$), B$_7$ (C_{2v}, $^2B_2$), B$_7^-$ (C_{6v}, $^3A_2$), and B$_7^-$ (C_{2v}, $^1A_2$). (Reprinted with permission from Ref. [69]. Copyright 2004 American Chemical Society.)

pared to the dangling density at the center of the cyclic D$_{7h}$ structure. This effect is even more pronounced for the eight and nine atomic boron clusters.

3.6.2. B$_7$

If one electron is added to the doubly degenerate LUMO of the global minimum structure of the B$_7^+$ cluster, the resulting structure of a neutral B$_7$ cluster is now a distorted quasi-pyramid due to the Jahn–Teller effect. The global minimum structure is C_{2v} $^2B_2$ ($1a_1^2 1b_2^2 1b_1^2 2a_1^2 1a_2^2 3a_1^2 2b_1^2 4a_1^2 2b_2^2 3b_1^2 3b_2^1$) (Fig. 24 and Table 18) [69,122,125,157,158].

According to our GEGA search, there are no low-lying isomers of the cluster within 23 kcal/mol (B3LYP/6-311+G* level) [135]. The occupation of partially bonding/antibonding π-MO (3b$_2$) (Fig. 25) brings the number of π electrons to three and thus B$_7$ is partially π-antiaromatic, but it is still a σ-aromatic system.

The calculated atomization energy of B$_7$ is 633 kcal/mol at CCSD(T)/6-311+G(2df)+ZPE [131].

3.6.3. B$_7^-$ and its photoelectron spectra

The B$_7^-$ anion received the least attention in the literature. Also, there is a controversy regarding the geometry of the global minimum of the B$_7^-$ species. According to Li et al. [157], the global minimum has a closed-shell C_{2v} ($^1A_1$) structure. However, this result does not completely agree with ours. According to our GEGA search (B3LYP/3-21G level) for both singlets and triplets [135], the B$_7^-$ cluster has a triplet very flat C_{6v} $^3A_2$ ($1a_1^2 1e_1^4 1e_2^4 2a_1^2 3a_1^2 1b_1^2 2e_1^4 3e_1^2$) pyramidal structure as a global minimum (Fig. 24).

The second lowest C_{2v} $^1A_1$ ($1a_1^2 1b_2^2 1b_1^2 2a_1^2 1a_2^2 3a_1^2 2b_1^2 4a_1^2 2b_2^2 3b_1^2 3b_2^2$) structure was found to be just 3.9 kcal/mol higher (B3LYP/6-311+G*) in energy than the global minimum struc-

Table 18
Molecular properties of B_7 (C_{2v}, $^2B_2$) global minimum structure

	B3LYP/6-311+G*[a]	BPW91/6-311+G*[b]	MP2/6-311+G*[b]	RCCSD(T)/6-311+G*[a]
E_{total} (a.u.)	−173.7102201	−173.6263	−173.0662	−173.1415275[c]
$R(B_1-B_{2,3,5,6})$ (Å)	1.691	1.695	1.704	1.718
$R(B_1-B_{4,7})$ (Å)	1.764	1.740	1.743	1.757
$R(B_2-B_3)$ (Å)	1.622	1.620	1.639	1.646
$R(B_4-B_{3,5})$ (Å)	1.557	1.570	1.574	1.595
$\omega_1(a_1)$ (cm^{-1})	1181	d	d	d
$\omega_2(a_1)$ (cm^{-1})	925	d	d	d
$\omega_3(a_1)$ (cm^{-1})	613	d	d	d
$\omega_4(a_1)$ (cm^{-1})	450	d	d	d
$\omega_5(a_1)$ (cm^{-1})	274	d	d	d
$\omega_6(a_2)$ (cm^{-1})	1101	d	d	d
$\omega_7(a_2)$ (cm^{-1})	600	d	d	d
$\omega_8(a_2)$ (cm^{-1})	358	d	d	d
$\omega_9(b_1)$ (cm^{-1})	1218	d	d	d
$\omega_{10}(b_1)$ (cm^{-1})	1063	d	d	d
$\omega_{11}(b_1)$ (cm^{-1})	764	d	d	d
$\omega_{12}(b_2)$ (cm^{-1})	1029	d	d	d
$\omega_{13}(b_2)$ (cm^{-1})	793	d	d	d
$\omega_{14}(b_2)$ (cm^{-1})	617	d	d	d
$\omega_{15}(b_2)$ (cm^{-1})	416	d	d	d

[a] Data from [69].
[b] Data from [158].
[c] At the RCCSD(T)/6-311+G(2df) level of theory total energy is −173.2111598 a.u.
[d] Frequencies were not reported at this level of theory.

ture. The geometries of these lowest lying isomers were then refined at the RCCSD(T)/6-311+G* level, and the final relative energies were estimated at the RCCSD(T)/6-311+G(2df)//RCCSD(T)/6-311+G* level of theory. At our highest level of theory, we found that the triplet structure V (C_{6v}, $^3A_2$) is lower in energy than the singlet structure VI (C_{2v}, $^1A_1$) by just 0.7 kcal/mol. Thus, these two structures are almost degenerate. The single point CASSCF(8,8)/6-

Table 19
Molecular properties of structures V–VII (Fig. 24) of B_7^- [69]

Structure V (C_{6v}, $^3A_2$)		Structure VI (C_{2v}, $^1A_1$)		Structure VII (C_{2v}, $^1A_1$)	
B3LYP/6-311+G*	RCCSD(T)/6-311+G*	B3LYP/6-311+G*	RCCSD(T)/6-311+G*	B3LYP/6-311+G*	RCCSD(T)/6-311+G*
E_{total} = −173.8037621	E_{total} = −173.2344498[a]	E_{total} = −173.797532	E_{total} = −173.234794[b]	E_{total} = −173.7861476	E_{total} = −173.2237467[c]
$R(B_1-B_{2-7})$ = 1.655 Å	$R(B_1-B_{2-7})$ = 1.683 Å	$R(B_1-B_{2,3,5,6})$ = 1.667 Å	$R(B_1-B_{2,3,5,6})$ = 1.694 Å	$R(B_1-B_{2,3})$ = 1.999 Å	$R(B_1-B_{2,3})$ = 1.932 Å
$R(B_2-B_3)$ = 1.606 Å	$R(B_2-B_3)$ = 1.633 Å	$R(B_1-B_{4,7})$ = 1.738 Å	$R(B_1-B_{4,7})$ = 1.781 Å	$R(B_1-B_{4,5})$ = 1.584 Å	$R(B_1-B_{4,5})$ = 1.609 Å
		$R(B_2-B_3)$ = 1.660 Å	$R(B_2-B_3)$ = 1.680 Å	$R(B_1-B_{6,7})$ = 2.780 Å	$R(B_1-B_{6,7})$ = 2.814 Å
		$R(B_4-B_{3,5})$ = 1.558 Å	$R(B_4-B_{3,5})$ = 1.590 Å	$\angle B_2-B_1-B_3$ = 48.96°	$\angle B_2-B_1-B_3$ = 50.98°
				$\angle B_4-B_1-B_5$ = 162.85°	$\angle B_4-B_1-B_5$ = 167.68°
				$\angle B_6-B_1-B_7$ = 113.82°	$\angle B_6-B_1-B_7$ = 116.26°
$\omega_1(a_1)$ = 918		$\omega_1(a_1)$ = 1130		$\omega_1(a_1)$ = 1303	
$\omega_2(a_1)$ = 293		$\omega_2(a_1)$ = 932		$\omega_2(a_1)$ = 1207	
$\omega_3(b_1)$ = 1057		$\omega_3(a_1)$ = 652		$\omega_3(a_1)$ = 817	
$\omega_4(b_2)$ = 756		$\omega_4(a_1)$ = 441		$\omega_4(a_1)$ = 665	
$\omega_5(b_2)$ = 352		$\omega_5(a_1)$ = 240		$\omega_5(a_1)$ = 566	
$\omega_6(e_1)$ = 1121		$\omega_6(a_2)$ = 1104		$\omega_6(a_1)$ = 435	
$\omega_7(e_1)$ = 756		$\omega_7(a_2)$ = 648		$\omega_7(a_2)$ = 472	
$\omega_8(e_2)$ = 1111		$\omega_8(a_2)$ = 423		$\omega_8(a_2)$ = 246	
$\omega_9(e_2)$ = 685		$\omega_9(b_1)$ = 1183		$\omega_9(b_1)$ = 416	
$\omega_{10}(e_2)$ = 356		$\omega_{10}(b_1)$ = 1091		$\omega_{10}(b_1)$ = 183	
		$\omega_{11}(b_1)$ = 695		$\omega_{11}(b_2)$ = 1273	
		$\omega_{12}(b_2)$ = 1094		$\omega_{12}(b_2)$ = 1126	
		$\omega_{13}(b_2)$ = 797		$\omega_{13}(b_2)$ = 886	
		$\omega_{14}(b_2)$ = 570		$\omega_{14}(b_2)$ = 671	
		$\omega_{15}(b_2)$ = 409		$\omega_{15}(b_2)$ = 534	

[a] At the RCCSD(T)/6-311+G(2df) E_{total} = −173.3156597 a.u.
[b] At the RCCSD(T)/6-311+G(2df) E_{total} = −173.314586 a.u.
[c] At the RCCSD(T)/6-311+G(2df) E_{total} = −173.3033020 a.u.

311+G(2df) calculations showed that the Hartree–Fock configuration is dominant for B_7^- (C_{HF} are 0.953 for the triplet structure and 0.963 for the singlet structure). Hence, our B3LYP and RCCSD(T) calculations should be reliable. There is also a planar low-lying local minimum structure C_{2v}, $^1A_1$ ($1a_1^2 1b_2^2 2a_1^2 3a_1^2 2b_2^2 3b_2^2 1b_1^2 4a_1^2 5a_1^2 1a_2^2 4b_2^2$). At the RCCSD(T)/6-311+G(2df) level of theory it was 7.8 kcal/mol above the global minimum. Molecular properties of the three lowest-energy isomers of B_7^- are given in Table 19.

The calculated atomization energy for B_7^- (B_7^- (C_{6v}, $^3A_1' \rightarrow 6B$ (^2P) + B^- (^3P)) was calculated to be 695 kcal/mol at CCSD(T)/6-311+G(2df)+ZPE [131].

The photoelectron spectra of B_7^- were obtained at three photon energies, as shown in Fig. 26 [69].

All data shown were taken with the ^{10}B enriched target ($^{10}B_7^- = 70$ amu). Spectra taken with the natural isotope boron target for two isotopmers 76 amu and 77 amu were used to rule out the $B_4O_2^-$ contaminations. With the ^{10}B enriched target, we were able to completely separate B_7^- (70 amu) and $B_4O_2^-$ (72 amu) in the mass spectrum.

Fig. 27 shows the experimental evidence for the coexistence of isomers in the B_7^- beam.

Fig. 27a displays the same data as Fig. 26c, which was taken with the pure ^{10}B enriched target. Fig. 27b presents the spectrum taken with a ^{10}B/Li mixed target, which gave pure boron clusters in addition to the B/Li mixed clusters, but at different source conditions relative to a pure boron target. Surprisingly, the relative intensities of certain spectral features are quite different in the two data sets: the intensities of features A, B, and G were significantly decreased in Fig. 27b compared to the spectrum in Fig. 27a. Since we were able to eliminate any possibilities for contamination, this observation indicated that features A, B, and G came from a different isomer of B_7^-. Even though we had the ability to control the cluster temperatures to some degree with our cluster source, we were not able to alter the populations of the two isomers of B_7^- significantly when pure boron targets were used in the laser vaporization.

The ab initio calculations suggested that at least two isomers (V and VI) could coexist in the B_7^- beam and contribute to the photoelectron spectra of B_7^-. Isomer VII could also be present, though it was expected to be weak because it was 7.8 kcal/mol higher than the ground state structure V at the RCCSD(T)/6-311+G(2df) level of theory. The calculated VDEs from V (into final quartet states only), VI, and VII at the OVGF level of theory (Table 20) are plotted as vertical bars in Fig. 27.

Structures V and VI gave very similar spectral transitions because they are nearly degenerate and have similar MO patterns. The bottom row of the vertical bars is for the lowest energy pyramidal triplet structure V (C_{6v}, $^3A_2$), the middle row is for the lowest energy pyramidal singlet isomer VI (C_{2v}, $^1A_1$), and the top row is for the planar singlet isomer VII (C_{2v}, $^1A_1$). VDEs with the final doublet states for the structure V of B_7^- overlap with the VDEs corresponding to transitions into the similar states for the structure VI (Table 20). However, the VDEs for the structure VI are in better agreement (especially at the OVGF/6-311+G(2df) level of theory) with the experimentally observed peaks X, E, F, H, and I. The features A, B, and G could be
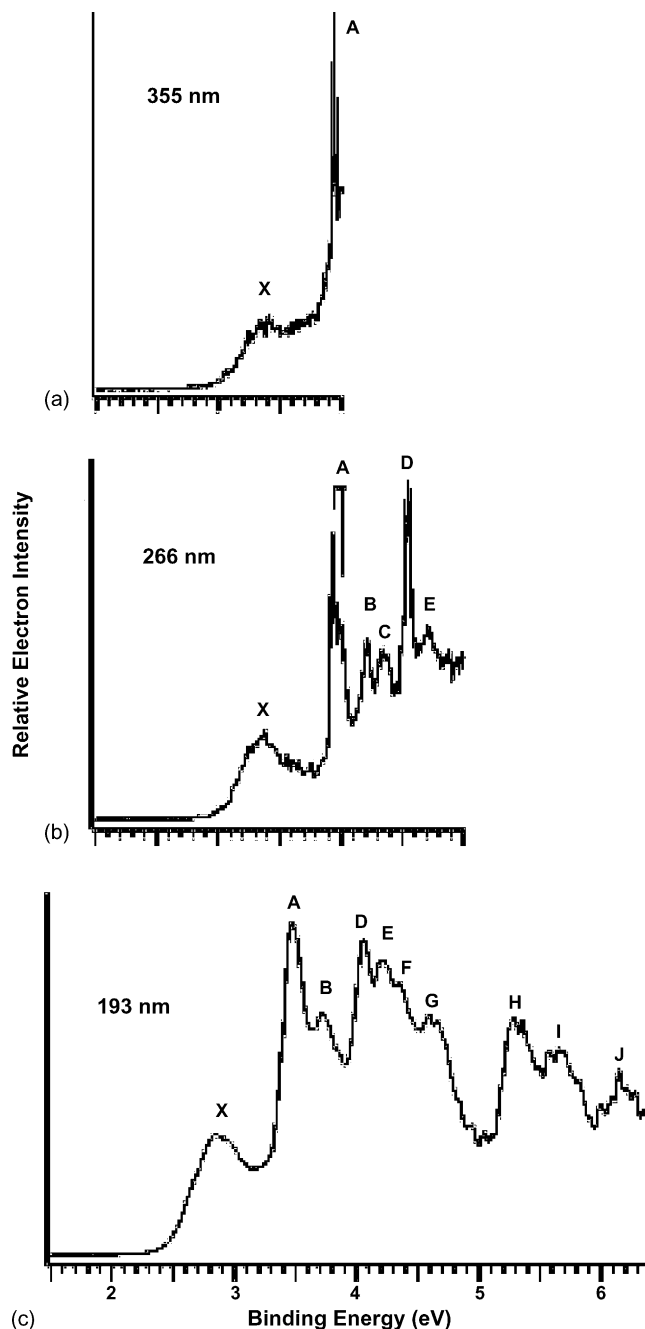
Fig. 26. Photoelectron spectra of B_7^- at: (a) 355 nm (3.496 eV), (b) 266 nm (4.661 eV), and (c) 193 nm (6.424 eV). (Reprinted with permission from Ref. [69]. Copyright 2004 American Chemical Society.)

attributed to contributions from the higher energy planar structure VII. Overall, the calculated spectra from the pyramidal and planar structures of B_7^- are in excellent agreement with the experimental data.

It is interesting to note the large energy gaps between the first detachment transition (X) and the second transition (D) for both of the pyramidal isomers (Table 20). This large energy gap suggested that the two electrons in the HOMO of these two isomers are relatively unstable and their removal would produce a much more electronically stable B_7^+. This expectation was supported
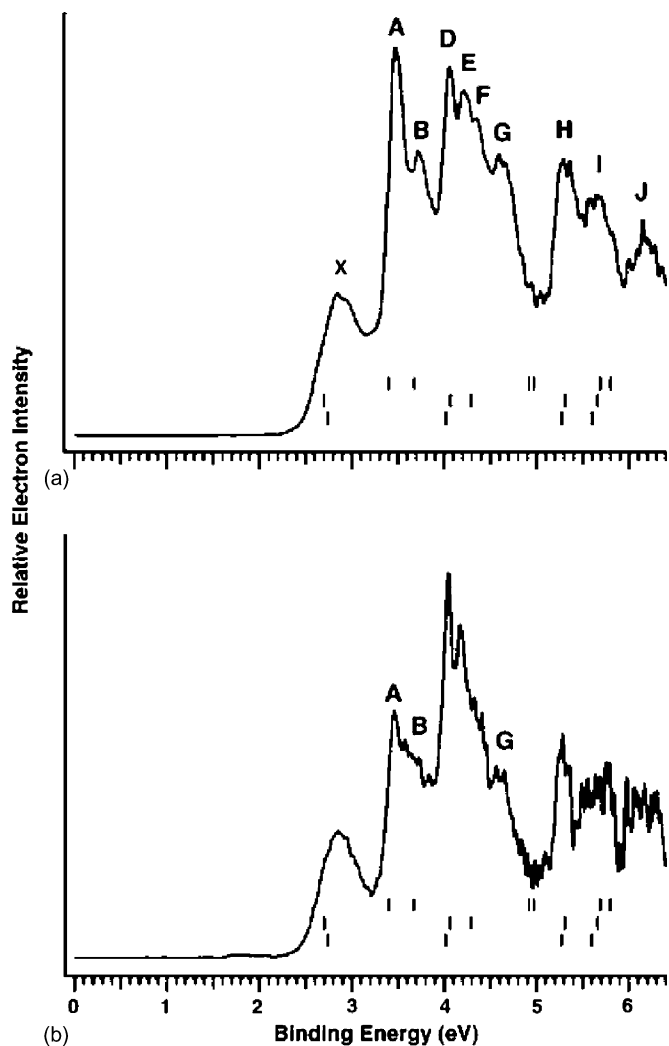
Fig. 27. Photoelectron spectra of B_7^- at two different conditions. The B_7^- cluster beam was produced with a: (a) ^{10}B enriched target and (b) $^{10}B/Li$ mixed target, respectively. Note the intensity variation of features A, B, and G from (a) to (b), indicating that these features were from a different isomer of B_7^-. The vertical bars were theoretical VDEs at the OVGF level of theory for isomers V, VI, and VII as shown in Fig. 24 (from bottom row up), respectively. (Reprinted with permission from Ref. [69]. Copyright 2004 American Chemical Society.)

by previous experimental studies, which did show that B_7^+ was an extremely stable cation [53–59]. This observation provided another confirmation for the validity of the interpretation of the B_7^- photoelectron spectra.

The planar isomer VII of B_7^-, although it is significantly less favorable energetically than the pyramidal ones, was quite abundant from our cluster source. Its spectral intensities were as intense as the more stable pyramidal B_7^-. This was rather surprising. The high abundance of the planar B_7^- isomer must be due to its high kinetic stability and can be understood from the cluster growth mechanisms. As was shown in Section 3.5, both B_6^- and B_6 are planar. Addition of one B atom to any of these structures would lead to the planar B_7^- structure VII with small geometry changes. On the other hand, formation of the pyramidal B_7^- from the D_{2h} or C_{2h} hexamer by addition of one B atom would involve significant structural rearrangement.

The chemical bonding of all pyramidal B_7^- clusters can be understood from Fig. 25. The molecular orbitals shown in the figure are drawn for the model planar D_{6h} system. MOs of all considered B_7^- clusters are very similar to those of the planar D_{6h} species. NBO analysis showed that the set of low-energy MOs: $1a_1$, $1e_1$, $1e_2$, and $1b_1$ (in the species of the C_{6v} symmetry point group), or $1a_1$, $1b_2$, $1b_1$, $1a_2$, $2a_1$, and $2b_1$ (in the species of the C_{2v} symmetry point group), can be localized onto six peripheral 2c-2e B–B bonds, forming the hexagonal framework. The remaining molecular orbitals cannot be localized, and they are responsible for global bonding in the clusters and for the bonding of the hexagons with the central B-atoms.

In the neutral (C_{2v}, $^2B_2$) B_7 cluster, molecular orbitals analyzed for B_7^+ (see Section 3.6.1) are also present in the valence pool. In addition, one of the partially bonding π-MOs with one nodal plane is occupied (HOMO, $3b_2$ in Fig. 25, second from the top line). This orbital belongs to the quasi-degenerate set of π-MOs with a counterpart as the LUMO ($4b_1$). Partial occupation of the degenerate MO abolishes the degeneracy and imposes a Jahn–Teller distortion on the geometry of the cluster. That is why the pyramidal C_{6v} structure of the cation undergoes deformation toward C_{2v} geometry of the neutral in its global minimum form. Furthermore, now the π-subsystem of MOs contains three electrons (two in the HOMO-5 ($3a_1$) and one in the HOMO ($3b_2$)), although the classical $4n$ rule is not followed in this case, the cluster possesses structural deformation, and it can be called partially π-antiaromatic. Note that σ-aromaticity of the species is preserved.

The last two lines in the MO assignment in Fig. 25 belong to the global minimum isomers of the anion B_7^-. Isomer V (C_{6v}, $^3A_2$) possesses the same MOs as the cationic B_7^+ cluster. However, in this case, the partially bonding π-MO (HOMO, $3e_1$), which was the LUMO in the cation, is also occupied. In this triplet species the π-orbitals forming the doubly degenerate HOMO are equally populated by one electron each. The reverse $4n$ Hückel's rule for aromaticity in triplets in obeyed in this cluster. The species is π-aromatic. It is also σ-aromatic for the reason described above, and thus doubly aromatic character is identified in this species. It is worth pointing out that, although the electron pairing is a beneficial occurrence, the triplet species is more stable than its singlet ancestor (species VI). The doubly aromatic character of the chemical bonding is the reason for this stabilization.

In the singlet B_7^- species VI (C_{2v}, $^1A_1$), the two electrons (unpaired in the triplet) are now coupled. Thus, it has now four π-electrons and for singlets, that it means it is π-antiaromatic, but it is still σ-aromatic with six globally delocalized electrons.

The similar MO analysis for the C_{2v} ($^1A_1$) planar structure VII (Fig. 24) reveals that it is doubly (σ- and π-) antiaromatic.

Li and Gong [159] computationally considered the possibility to forming MB_7 (M = Li, Na, K, Rb, and Cs). They assumed that these species will adopt either a planar structure with a cation being at the center of the planar D_{7h} cyclic B_7^- cluster, or they will adopt a heptagonal pyramid with a cation located above the planar D_{7h} cyclic B_7^- cluster. While they indeed found that these structures are true local minima on the potential energy surface,

Table 20
Calculated VDEs of B_7^- at different levels of theory for structures V–VII (Fig. 24) and recommended PES data assignments

Isomer	Calculated transition	Theoretical VDE[a]				PES data assignment	
		U(R)OVGF/ 6-311+G(2df)	RCCSD(T)/ 6-311+G(2df)	TD-B3LYP/ 6-311+G(2df)	TD-BPW91 6-311+G(2df)	Observed feature	Experimental VDE
V (C_{6v}, $^3A_2$)[b]	$3e_1\ \alpha \to\ ^2E_1$	2.74 (0.91)	2.89	2.80	2.95	X	2.85
	$2e_1\ \beta \to\ ^4E_1$	4.02 (0.89)	4.14	3.96	3.88	D	4.05
	$2e_1\ \alpha \to\ ^2E_1$	[4.28 (0.90)][c]		4.04	3.93		
	$3a_1\ \beta \to\ ^4A_1$	5.27 (0.91)	5.85	5.35	5.13	H	5.32
	$1b_1\ \beta \to\ ^4B_1$	5.60 (0.90)	5.96	5.39	5.36	I	5.64
	$1b_1\ \alpha \to\ ^2B_1$	[5.61 (0.90)][c]		4.71	4.72		
	$3a_1\ \beta \to\ ^2A_1$	[6.35 (0.84)][c]		5.18	5.04		
VI (C_{2v}, $^1A_1$)[d]	$3b_2 \to\ ^2B_2$	2.70 (0.88)	2.83	2.59	2.65	X	2.85
	$3b_1 \to\ ^2B_1$	4.07 (0.87)	4.20	4.18	4.07	E	4.21
	$2b_2 \to\ ^2B_2$	4.29 (0.88)		4.33	4.30	F	4.35
	$2b_1 \to\ ^2B_1$	5.31 (0.87)		5.32	5.08	H	5.32
	$4a_1 \to\ ^2A_1$	5.66 (0.80)	5.87	5.93	5.89	I	5.64
VII (C_{2v}, $^1A_1$)[e]	$4b_2 \to\ ^2B_2$	3.40 (0.86)	3.51	3.10	3.06	A	3.44
	$1a_2 \to\ ^2A_2$	3.67 (0.88)	3.69	3.55	3.68	B	3.71
	$5a_1 \to\ ^2A_1$	4.92 (0.83)	4.81	4.72	4.52	G	4.60
	$4a_1 \to\ ^2A_1$	4.97 (0.83)		5.33	5.27		
	$1b_1 \to\ ^2B_1$	5.69 (0.83)	5.78	5.84	5.76		
	$3b_2 \to\ ^2B_2$	5.80 (0.84)		5.49	5.35		

All energies are in eV [69].

[a] The numbers in the parentheses indicate the pole strength, which characterizes the validity of the one-electron detachment picture.

[b] At the RCCSD(T)/6-311+G(2df) level of theory $\Delta E = 0.0$ kcal/mol.

[c] Vertical electron detachment energies calculated at the UOVGF level of theory leading to the final doublet states should be considered as very crude due to the multi-configurational nature of the reference wave function in the final doublet states.

[d] At the RCCSD(T)/6-311+G(2df) level of theory $\Delta E = 0.7$ kcal/mol.

[e] At the RCCSD(T)/6-311+G(2df) level of theory $\Delta E = 7.8$ kcal/mol.

we believe that it would be impossible to make such species even in molecular beams, because the planar D_{7h} $^1A_1'$ cyclic structure is highly unfavorable (less stable than the C_{6v} $^3A_2$ structure by 83.8 kcal/mol at B3LYP/6-311+G*) for the isolated B_7^- anion according to our calculations. The explanation why the doubly aromatic planar D_{7h} $^1A_1'$ cyclic structure is significantly less stable than the centered C_{6v} $^3A_2$ global minimum structure is the same as in the case of B_7^+ (see Section 3.6.1).

3.6.4. $H_2B_7^-$ and $Au_2B_7^-$

Two anionic clusters, $H_2B_7^-$ and $Au_2B_7^-$, have been recently studied theoretically, and the latter was also studied by photoelectron spectroscopy [160,161]. We discuss these anions in more detail than other partially hydrated boron clusters, because these two systems show us the usefulness of the multiple aromaticity/antiaromaticity concepts we discussed for pure boron clusters.

As we just discussed, the pure-boron B_7^- cluster has a doubly (σ- and π-) aromatic C_{6v} ($^3A_2$) quasi-planar wheel-type triplet global minimum (structure I, see Fig. 28), a low-lying σ-aromatic and π-antiaromatic quasi-planar singlet C_{2v} ($^1A_1$) isomer II (0.7 kcal/mol above the global minimum), and a planar doubly (σ- and π-) antiaromatic C_{2v} ($^1A_1$) isomer III (7.8 kcal/mol above the global minimum).

In our recent paper [160], we have shown that upon hydrogenation, an inversion in the stability of the species occurs. The search for the most stable structure of the $B_7H_2^-$ anion, performed by the GEGA and accompanied by the

higher-level calculations, revealed that the planar IV C_{2v}, $^1A_1$ ($1a_1^2 1b_2^2 2a_1^2 2b_2^2 3a_1^2 4a_1^2 3b_2^2 1b_1^2 4b_2^2 5a_1^2 6a_1^2 1a_2^2$) (Fig. 28b) structure is the global minimum. The order of the lowest energy structures for $B_7H_2^-$ was the same at the B3LYP/3-21G, B3LYP/6-311+G* and CCSD(T)/6-311+G* levels of theory. The planar $B_7H_2^-$ (C_{2v}, $^1A_1$) isomer IV, originating from the addition of two hydrogen atoms to the doubly antiaromatic B_7^- isomer III, becomes the global minimum structure. The second most stable $B_7H_2^-$ isomer V, originating from the quasi-planar triplet wheel isomer I of B_7^-, was found to be 27 kcal/mol higher in energy.

We performed a careful chemical bonding analysis for the two lowest isomers, which reveals that the inversion in stability occurs due to the loss of the doubly aromatic character in the wheel-type global minimum isomer I (C_{6v}, $^3A_1$) of B_7^- upon H_2-addition. In contrast, the planar isomer III of B_7^- (C_{2v}, $^1A_1$) gains aromatic character upon addition of two hydrogen atoms, which makes it more stable. According to the NBO analysis of the global minimum structure of $B_7H_2^-$, it has nine classical 2c-2e bonds, seven of which are localized on the peripheral edges of the B_7-unit (bonds B_1–B_4, B_4–B_6, B_6–B_2, B_2–B_3, B_3–B_7, B_7–B_5, and B_5–B_1, see Fig. 28), and the remaining two are simply covalent B–H bonds. The rest of the electrons in the system participate in delocalized bonding over the entire cluster. A similar bonding picture was found in structure III of the bare B_7^- species. The NBO analysis showed the presence of seven peripheral 2c-2e B–B bonds in the B_7^- cluster. However, the difference between the dihydride and the original B_7^- cluster occurs in the structure of delocalized bonding patterns.
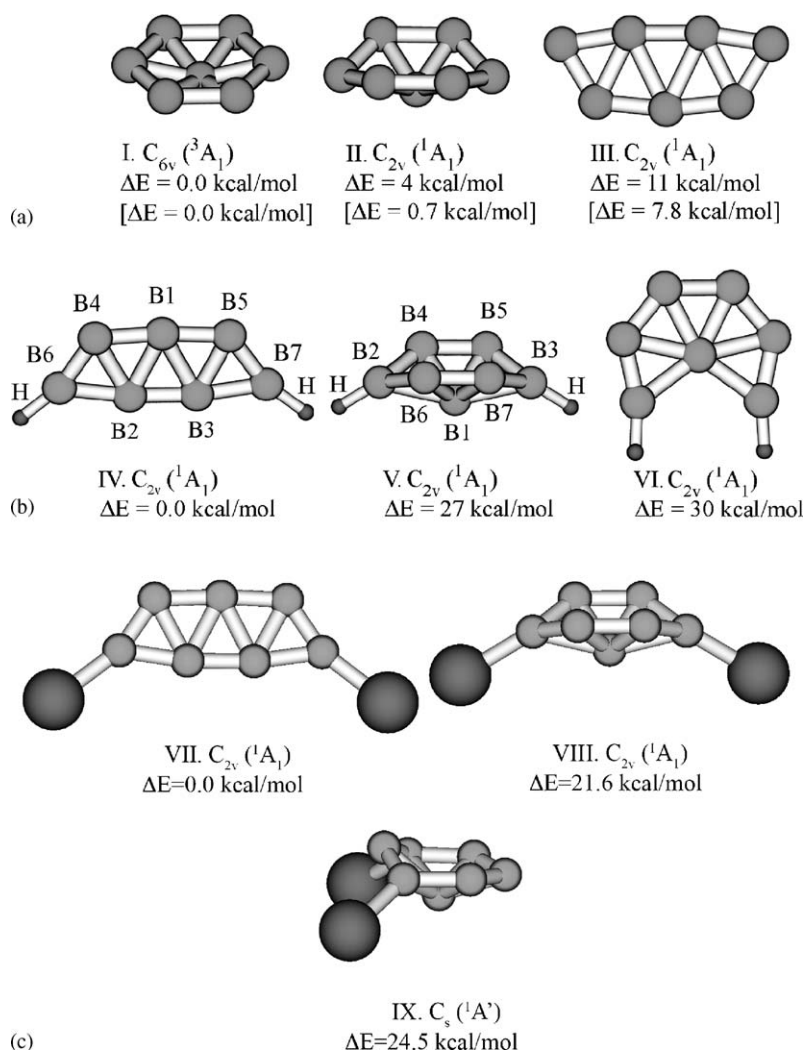
Fig. 28. (a) Low-energy isomers of B_7^- cluster at the B3LYP/6-311+G* level of theory (relative energies computed at the CCSD(T)/6-311+G(2df) level are shown in square brackets). (b) The global minimum and two low-lying isomers of $B_7H_2^-$ at the B3LYP/6-311+G* level of theory. (c) The global minimum and two low-lying isomers of $Au_2B_7^-$ at the B3LYP/B/aug-cc-pvTZ/Au/Stuttgart + 2f1g level of theory. (Reprinted with permission from Ref. [161]. Copyright 2006 American Chemical Society.)

The molecular orbitals of the global minimum isomer IV of $B_7H_2^-$ are shown in Fig. 29a. Fig. 29b represents the molecular orbitals of structure III of the bare B_7^- cluster.

The HOMO, HOMO-1, and HOMO-4 in $B_7H_2^-$ are responsible for the bonding over the whole system. Similar analysis performed on the bare B_7^- cluster revealed that the delocalized region sacrifices one molecular orbital. Indeed, the HOMO of the B_7^- cluster is missing in $B_7H_2^-$, while the HOMO-1 in B_7^- corresponds to the HOMO in $B_7H_2^-$, the HOMO-2 in B_7^- corresponds to the HOMO-1 in $B_7H_2^-$, and the shapes of the HOMO-4 are identical in the two species (see Fig. 29).

The planar isomer III of the B_7^- cluster possesses doubly antiaromatic character. The HOMO-4 ($1b_1$) is a completely bonding π-molecular orbital, and the HOMO-1 ($1a_2$) is partially bonding π-MO with one π-nodal plane. Four π-electrons on these MOs make structure III of B_7^- π-antiaromatic. The HOMO-2 ($5a_1$) and the HOMO ($4b_2$) are molecular orbitals of σ-type formed by the radial overlap of the 2p-AOs on boron atoms, where the former MO is completely bonding, and the

latter one is partially bonding. Hence, the four electrons occupying these MOs make the system also σ-antiaromatic.

In the hydride, the mentioned partially bonding σ-molecular orbital (HOMO in B_7^-) is now a virtual orbital. The only delocalized σ-MO in the species is the HOMO-1 ($6a_1$) (Fig. 29a). Thus, the cluster is σ-aromatic. The π-molecular orbitals in the $B_7H_2^-$ cluster are analogous to those in the B_7^- species. Four electrons in these MOs make the global minimum of $B_7H_2^-$ π-antiaromatic. Consequently, upon the molecular hydrogen addition, the planar B_7^- cluster gains σ-aromaticity and loses the antibonding character in the σ-set of MOs.

We also performed a molecular orbital analysis for the wheel-type B_7^- and $B_7H_2^-$ moieties. The molecular orbitals of these species are shown in Fig. 30.

Fig. 30 depicts the MOs of the clusters in a simplified manner, i.e., when geometries of both clusters are adjusted to planarity. This adjustment is done in order to make the bonding picture clearer (the sets of valence MOs shown are analogous to the ones in the original species). The HOMO, HOMO-1, HOMO-
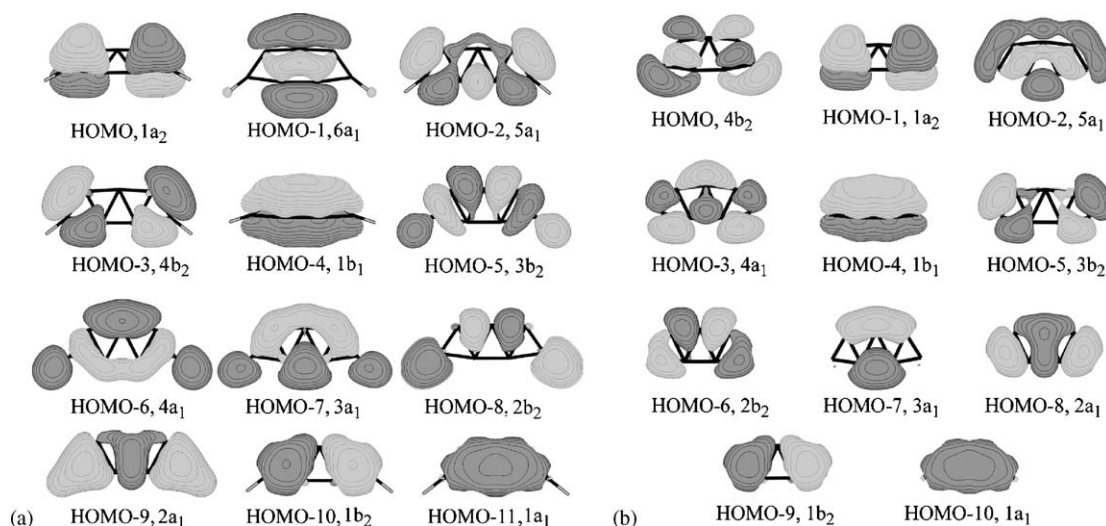
Fig. 29. Molecular orbital picture of the: (a) global minimum of $B_7H_2^-$ (C_{2v}, $^1A_1$) and (b) planar bare B_7^- cluster (C_{2v}, $^1A_1$). (Reprinted with permission from Ref. [160]. Copyright 2005 Springer.)

2, and HOMO-5 in $B_7H_2^-$, and HOMO, HOMO′, HOMO-1, HOMO-1′, HOMO-2, and HOMO-4 in B_7^- are responsible for the global bonding over the whole system. As has been reported earlier [69], the triplet species I is doubly aromatic. The HOMO-4 ($1a_{2u}$) in Fig. 30b is a completely bonding π-MO and the HOMO-2 ($2a_{1g}$) is a completely bonding σ-MO. Degenerate pairs HOMO ($1e_{1g}$) and HOMO-1 ($2e_{1u}$) are partially bonding MOs of π- and σ-radial types, respectively. Thus, the structure I is σ-aromatic (six σ-electrons), and π-aromatic (four π-electrons with single occupancy of the every degenerate HOMO). In the second isomer of B_7^- (singlet structure II, Fig. 28), the HOMO (Fig. 30b) is doubly occupied, leaving the second degenerate MO unoccupied. Thus, the regular $4n$ rule governs the shape of the cluster, making it π-antiaromatic. However, the second lowest isomer of $B_7H_2^-$ (structure V, Fig. 28)

possesses double antiaromaticity. The HOMO-5 ($1b_{3u}$) and HOMO ($1b_{2g}$) are π-MOs populated by four electrons, and thus the system is π-antiaromatic. The HOMO-2 ($4a_g$) and HOMO-1 ($3b_{2u}$) are σ-radial MOs populated by four σ-electrons, and thus the system is also σ-antiaromatic. Hence, upon hydration, the most stable triplet B_7^- cluster I loses both π- and σ-aromatic character. The singlet isomer III of B_7^-, being σ-aromatic and π-antiaromatic, becomes doubly antiaromatic during the hydration process. This MO analysis although somewhat long, allows us to rationalize why this alteration in relative energies of B_7^- clusters occurs upon addition of two hydrogen atoms.

There are no experimental data to verify our prediction for $H_2B_7^-$, but we recently obtained an indirect proof of that through a joint experimental and theoretical study of the $Au_2B_7^-$ anion [161].
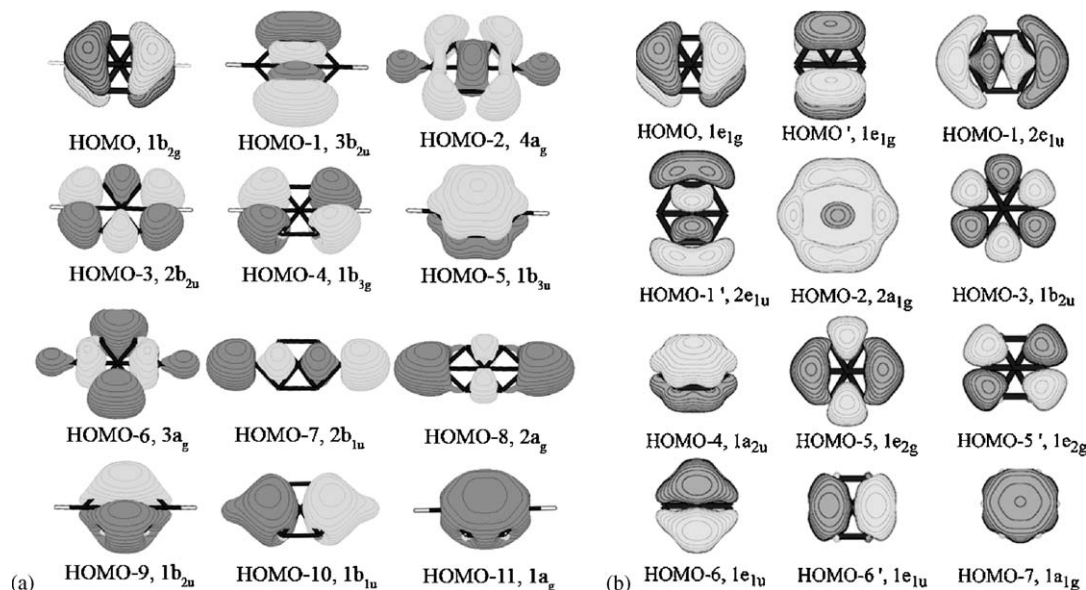
Fig. 30. Adjusted to the planarity molecular orbital picture of: (a) the second isomer of $B_7H_2^-$ and (b) bare B_7^- cluster with corresponding geometry. (Reprinted with permission from Ref. [160]. Copyright 2005 Springer.)

Wang and co-workers recently demonstrated in joint photoelectron spectroscopy and theoretical calculations that gold atoms apes hydrogen in Au–Si clusters [162,163]. On the basis of that and the similarity in electronegativity between B and Si, we conjecture that Au may form some Au–B clusters similar to the corresponding valence isoelectronic H–B clusters. We thought that $Au_2B_7^-$ cluster could be a good candidate for such a test. If Au in the $Au_2B_7^-$ cluster would result in the significant stabilization of the structure similar to structure IV for $B_7H_2^-$ (Fig. 28), we would expect a great simplification of the photoelectron spectra of $Au_2B_7^-$ compared to those of B_7^-, which is very congested and complicated because of the presence of a few low-lying isomers (Figs. 26 and 27).

We generated $Au_2B_7^-$ anions in a molecular beam and recorded their photoelectron spectra. The PES data of $Au_2B_7^-$ at 266 nm and 193 nm photon energies are shown in Fig. 31a and b, respectively.

The 193 nm PES spectra of B_7^- are also shown in Fig. 31c for comparison. The observed detachment energies and vibrational frequencies are summarized in Table 21.

One can see that indeed, the $Au_2B_7^-$ photoelectron spectrum is substantially simpler with vibrational resolution in the feature X, in agreement with our expectations. Note that the lower binding energy B_7^- isomers (I and II, Fig. 28) disappeared completely in $Au_2B_7^-$.

In order to confirm further that only one structure of $Au_2B_7^-$ (H substituted by Au in the isomer IV of $B_7H_2^-$) contributed to experimental spectrum, we performed quantum chemical calculations for a variety of $Au_2B_7^-$ structures, which we derived from the low-lying $B_7H_2^-$ structures. We found that the geometry for global minimum structure of $Au_2B_7^-$ is very similar at two levels of theory [161].

We then calculated VDEs for the $Au_2B_7^-$ global minimum structure using the TD-B3LYP/aug-cc-pvTZ/Au/ Stuttgart_rsc_1997_ecp level of theory and they are compared with the experimental VDEs in Table 21.

Good agreement between experimental and theoretical VDEs confirmed the theoretical prediction of global minimum structure VII for $Au_2B_7^-$, and thus indirectly confirmed theoretically predicted structure IV of $B_7H_2^-$ (Fig. 28). The substantial stabilization of structure III of B_7^- upon either addition of two H or two Au atoms confirms the earlier observation by Wang and co-workers [162,163] that Au may mimic H in some valence isoelectronic clusters.

Table 21
Experimental vertical detachment energies (VDEs) of $B_7Au_2^-$ from the photoelectron spectra, compared with theoretical calculations [161]

Feature	VDE (experimental) (eV)[a]	MO	VDE (theoretical) (eV)[b]
X	3.52 (2)	$3a_2$	3.46
A	4.27 (2)	$9a_1$	4.21
B	4.38 (3)	$8a_1$	4.36
C	4.90 (2)	$7b_2$	4.92
D	5.08 (3)	$6b_2$	5.19
E	5.58 (2)	$7a_1$	5.31
F	5.93 (2)	$3b_1$	5.75

[a] Numbers in parentheses represent experimental uncertainties in the last digit.
[b] At TD-B3LYP/B/aug-cc-pvTZ/Au/Stuttgart_rsc_1997_ecp level of theory.
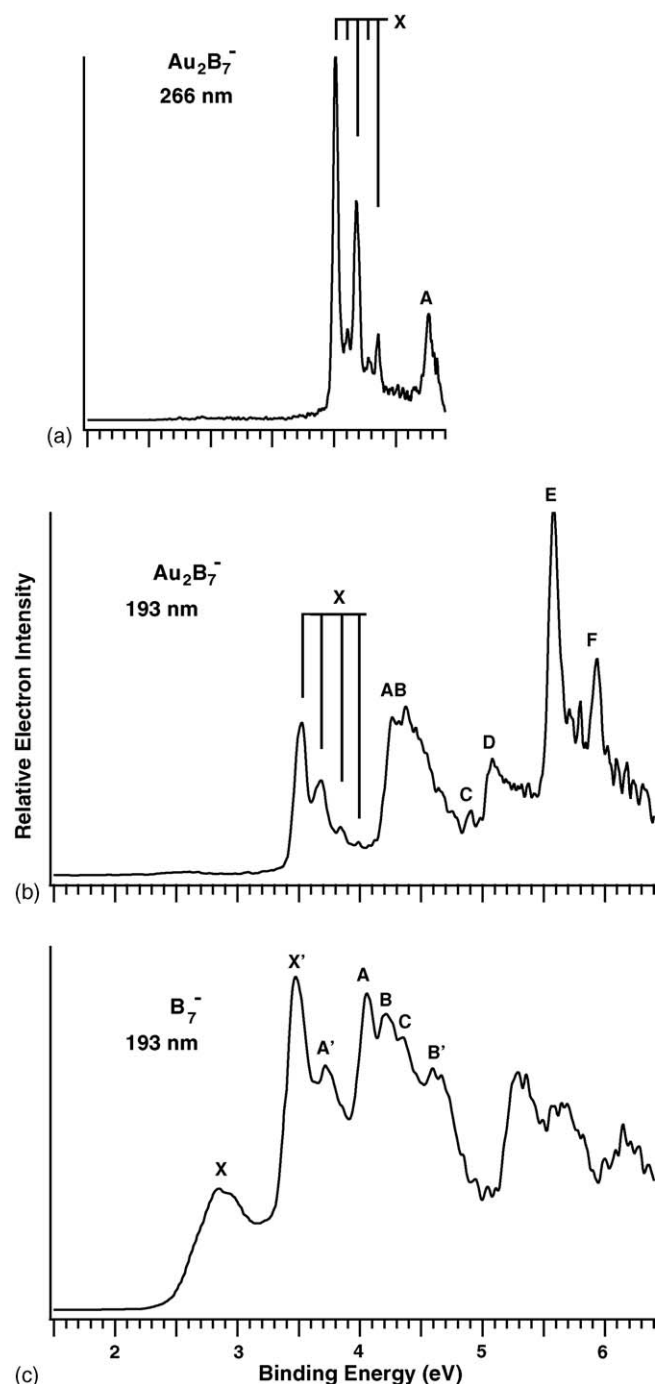
Fig. 31. Photoelectron spectra of $Au_2B_7^-$ at: (a) 266 nm (4.661 eV) and (b) 193 nm (6.424 eV). The 193 nm spectrum of B_7^- (c) is also included for comparison. (Reprinted with permission from Ref. [161]. Copyright 2006 American Chemical Society.)

3.7. Octaatomic clusters: B_8, B_8^+, B_8^-, B_8^{2-}

3.7.1. B_8^+

According to various levels of theoretical studies by Bonacic-Kounecky et al. [125], Boustani [127], and Ricca and Bauschlicher (CCSD(T)/cc-pVTZ//B3LYP/cc-pVTZ level of theory) [61,128], the B_8^+ cation has a C_{2v} ($^2B_1$) structure, which is a Jahn–Teller distorted planar heptagon (Fig. 32).
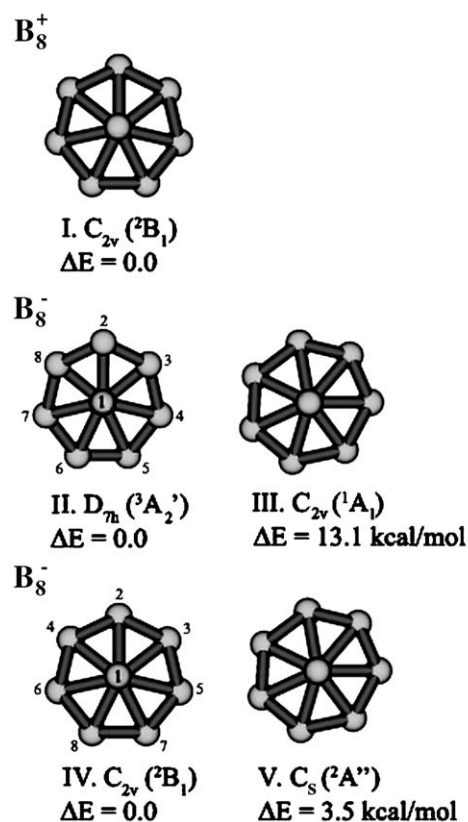
Fig. 32. Lowest-energy structures of octaatomic pure-boron cluster. (Reprinted with permission from Ref. [70]. Copyright 2003 Wiley.)

The true heptagon (D_{7h}) is just 1.2 kcal/mol above the ground state and has one imaginary frequency. The D_{6h} hexagonal bipyramid is 35.5 kcal/mol above the ground state and has two imaginary frequencies [61,128]. A different spectroscopic state

(C_{2v}, $^2A_2$) was reported by Kato et al. [122], who used the MP4(SDTQ)/3-21G level of computation. Ray et al. predicted the global minimum of B_8^+ to have a dodecahedral shape [116]. However, we believe that the distorted heptagon with the C_{2v}, $^2B_1$ structure is a true global minimum structure on the basis of published results in the literature and our joint experimental and theoretical study of B_8 and B_8^-.

3.7.2. B_8

The neutral B_8 cluster has been more extensively studied than the charged ones. According to the our GEGA search (B3LYP/3-21G) [135], and further calculations at higher levels of theory (B3LYP/6-311+G*, CCSD(T)/6-311+G*, and CCSD(T)/6-311+G(2df)) [70], the neutral B_8 cluster has a triplet perfect heptagon structure D_{7h} $^3A_2'$ ($1a_1'^2 1e_1'^4 1e_2'^4 2a_1'^2 1e_3'^4 1a_2''^2 2e_1'^4 1e_1''^2$) as its ground electronic state (structure II in Fig. 32). We also identified another wheel-type structure C_s $^1A'$, which was a singlet Jahn–Teller distorted heptagon, because in the heptagon singlet structure only one MO out of the two doubly degenerate $1e_1''$-HOMO is occupied (isomer III, Fig. 32) [70].

However, not everyone agrees with this assignment of the global minimum structure for the B_8 cluster. Boustani [62], Bonacic-Koutecky et al. [125], and Li et al. [164] agree with us that B_8 has the triplet D_{7h} structure. According to Reis et al., the D_{7h} heptagon has yet another ground spectroscopic triplet state: $^3B_2'$ [118]. A singlet C_{2v} ($^1A_1$) structure, which is a result of the Jahn–Teller distortion of the D_{7h} heptagon, was reported by Kato et al. [122] (MP4(SDTQ)/3-21G). We believe that according to the best theoretical results available today the correct global minimum structure is the triplet D_{7h}, $^3A_2'$ structure, with a low-lying singlet C_{2v} $^1A_1$ isomer [70]. Calculated molecular parameters of the neutral B_8 cluster are shown in Table 22.

Table 22
Molecular properties of the B_8 and B_8^- global minima [70]

	B_8 (D_{7h}, $^3A_2'$)			B_8^- (C_{2v}, $^2B_1$)	
	B3LYP/6-311+G^{*a}	CCSD(T)/6-311+G^{*a}	CASSCF(6,8)/6-311+G^{*a}	B3LYP/6-311+G^{*a}	
E_{total} (a.u.)	−198.5961959	−197.9432668[b]	−197.220515	−198.6993826[c]	
Geometry	R(B$_1$–B$_{2–8}$) = 1.791 Å	R(B$_1$–B$_{2–8}$) = 1.818 Å	R(B$_1$–B$_{2–8}$) = 1.791 Å	R(B$_1$–B$_2$) = 1.766 Å	∠B$_2$–B$_1$–B$_{3,4}$ = 52.2°
				R(B$_1$–B$_{3,4}$) = 1.788 Å	∠B$_{3,4}$–B$_1$–B$_{5,6}$ = 50.3°
				R(B$_1$–B$_{5,6}$) = 1.802 Å	∠B$_{5,6}$–B$_6$–B$_{1,8}$ = 51.1°
				R(B$_6$–B$_{1,8}$) = 1.772 Å	∠B$_7$–B$_1$–B$_8$ = 52.7°
Frequencies (cm^{-1})	ν_1(a$_1'$) = 815	[d]	ν_1(a$_1'$) = 871	ν_1(a$_1$) = 1378	ν_{10}(b$_1$) = 356
	ν_2(a$_2''$) = 278	[d]	ν_2(a$_2''$) = 245	ν_2(a$_1$) = 1234	ν_{11}(b$_1$) = 277
	ν_3(e$'$) = 1378	[d]	ν_3(e$'$) = 1420	ν_3(a$_1$) = 946	ν_{12}(b$_2$) = 1369
	ν_4(e$'$) = 1243	[d]	ν_4(e$'$) = 1323	ν_4(a$_1$) = 816	ν_{13}(b$_2$) = 987
	ν_5(e$'$) = 938	[d]	ν_5(e$'$) = 953	ν_5(a$_1$) = 800	ν_{14}(b$_2$) = 641
	ν_6(e$'$) = 702	[d]	ν_6(e$'$) = 687	ν_6(a$_1$) = 731	ν_{15}(b$_2$) = 597
	ν_7(e$'$) = 598	[d]	ν_7(e) = 623	ν_7(a$_1$) = 618	ν_{16}(b$_2$) = 418
	ν_8(e$'$) = 481	[d]	ν_8(e$'$) = 556	ν_8(a$_1$) = 499	ν_{17}(b$_2$) = 417
	ν_9(e$''$) = 423	[d]	ν_9(e$''$) = 465	ν_9(a$_2$) = 295	ν_{18}(b$_2$) = 5
	ν_{10}(e$''$) = 276	[d]	ν_{10}(e$''$) = 303		

[a] Method.

[b] At the CCSD(T)/6-311+G(2df)//B3LYP/6-311+G* level of theory $E_{total} = -198.033583$.

[c] At the CCSD(T)/6-311+G(2df)//B3LYP/6-311+G* level of theory $E_{total} = -198.141332$.

[d] Frequencies were not calculated at this level of theory.
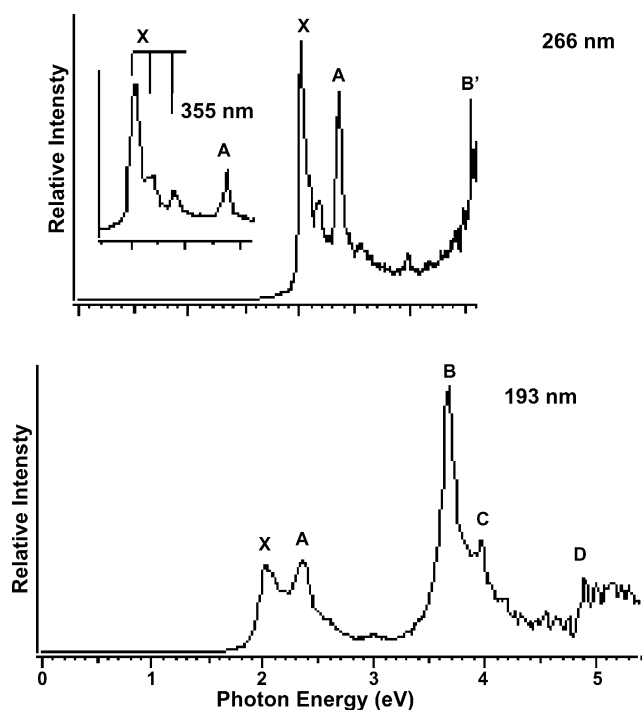
Fig. 33. Photoelectron spectra of B_8^- at 266 nm (the inset shows the spectrum taken at 355 nm) and at 193 nm. (Reprinted with permission from Ref. [70]. Copyright 2003 Wiley.)

We also tested three cyclic structures of B_8: I (D_{8h}, $^1A_{1g}$ ($1a_{1g}^2 1e_{1u}^4 1e_{2g}^4 1e_{3u}^4 1b_{2g}^2 2a_{1g}^2 1a_{2u}^2 1e_{1u}^4$)); II ($D_{8h}$, $^1A_{1g}$ ($1a_{1g}^2 1e_{1u}^4 1e_{2g}^4 1e_{3u}^4 1b_{2g}^2 2a_{1g}^2 1a_{2u}^2 1e_{1g}^4$)), and I ($D_{8h}$, $^5A_{1g}$ ($1a_{1g}^2 1e_{1u}^4 1e_{2g}^4 1e_{3u}^4 1b_{2g}^2 2a_{1g}^2 1a_{2u}^2 1e_{1u}^2 1e_{1g}^2$)). All these structures have eight peripheral B–B bonds and all are doubly aromatic systems with 6σ- and 2π- completely delocalized electrons in the structure I, 2σ- and 6π- completely delocalized electrons in the structure II, and with 4σ- and 4π-completely delocalized electrons in the structure III. However, all these three structures are significantly (>90 kcal/mol at B3LYP/6-311+G*) less stable than the global minimum centered D_{7h} $^3A_2'$ structure (see explanation why in Section 3.6.1).

3.7.3. B_8^- and its photoelectron spectra, B_8^{2-}

The singly charged anion B_8^- was found to be a doublet C_{2v} ($^2B_1$) [70]. The global minimum structure and the second low-lying isomer (C_s, $^2A''$) are shown in Fig. 32 as species IV and V, respectively. The doubly charged B_8^{2-} anion is a singlet, in which the D_{7h} symmetry is restored again because the $1e_1''$-HOMO is now occupied by four electrons [70].

Our joint experimental and theoretical study helped to establish the global minimum structures for B_8 and B_8^- [70]. The photoelectron spectra of B_8^- are shown in Fig. 33.

The VDEs for the global minimum species of B_8^- were found to be in excellent agreement with the experiment (Table 23) [70].

The chemical bonding in all B_8^+, B_8, B_8^-, and B_8^{2-} wheel-clusters can be understood via molecular orbital analysis (Fig. 34) [70].

The NBO analysis showed that the low-lying molecular orbitals HOMO-3, HOMO-5 to HOMO-7, can be localized into seven peripheral B–B bonds in the heptagon. The remaining delocalized MOs (HOMO, HOMO-1, HOMO-2, and HOMO-4) are responsible for the global bonding in the cluster, and for the bonding of the cycle with the central B-atom.

The HOMO ($1e_1''$) and HOMO-2 ($1a_2''$) are π-type MOs. They are occupied by four electrons in the triplet (D_{7h}, $^3A_2'$) structure of B_8, making it π-aromatic according to the reversed $4n$ Hückel's rule for triplets. The HOMO and HOMO-2 are occupied by six electrons in the singlet (D_{7h}, $^1A_1'$) structure of B_8^{2-} making it π-aromatic according to the $4n + 2$ Hückel's rule for singlets. The HOMO and HOMO-2 are occupied by three and by five electrons in B_8^+ and B_8^- clusters, respectively, making them partially antiaromatic.

The σ-radial type HOMO-1 ($2e_1'$) and HOMO-4 ($2a_1'$) are occupied by six electrons in all four clusters, and thus the clusters are also σ-aromatic ($4n + 2$ rule).

Overall, B_8^+ and B_8^- are σ-aromatic and partially π-antiaromatic. The triplet B_8 and the singlet B_8^{2-} are doubly (σ- and π-) aromatic. The doubly aromatic character of chemical bonding in the triplet B_8 and the singlet B_8^{2-} is responsible for the perfectly symmetric spectacular shape of these clusters.

Table 23
Experimental and theoretical vertical detachment energies (in eV) for B_8^- [70]

Observed features	VDE (experimental)[a]	Molecular orbital	Final state	VDE (theoretical), CCSD(T)/6-311+G(2df)	VDE (theoretical), EOM-RCCSD(T)/6-311+G(2d)
X	3.02 (2)	HOMO-1 ($1a_2$)	$^3B_2$	2.99[b]	
A	3.35 (2)	HOMO ($2b_1$)	$^1A_1$	3.45[b]	3.41
		HOMO-1 ($1a_2$)	$^1B_2$		3.45
B′	4.55 (4)	HOMO-2 ($6a_1$)	$^3B_1$	4.74[b]	
B	4.68 (6)	HOMO-3 ($4b_2$)	$^3A_2$	4.78[b]	
		HOMO-3 ($4b_2$)	$^1A_2$		4.79
C	4.98 (6)	HOMO-2 ($6a_1$)	$^1B_1$		5.15
		HOMO-4 ($1b_1$)	$^3A_1$	5.86[b]	

[a] Numbers in parentheses indicate the uncertainties of the last digit.
[b] Calculations were done at the RCCSD(T) level of theory.
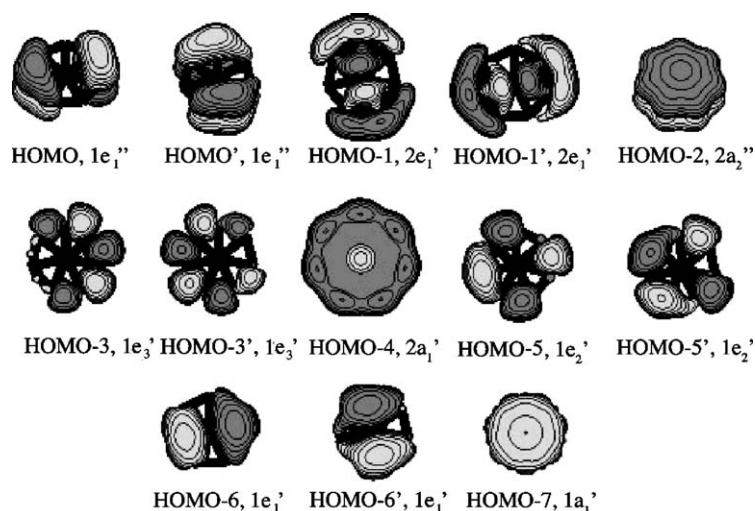
Fig. 34. Molecular orbital picture of B$_8$ (D_{7h}, $^3A_2'$). Adapted from [70].
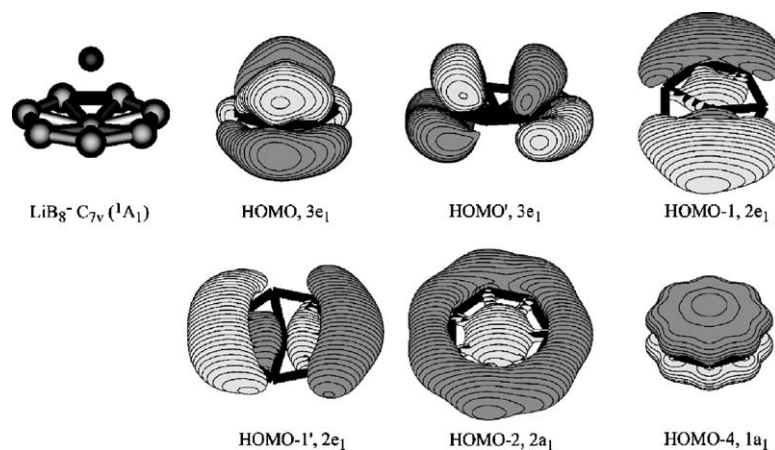
Fig. 35. Structure and delocalized molecular orbitals of the LiB$_8^-$ salt. (Reprinted with permission from Ref. [165]. Copyright 2004 American Chemical Society.)

3.7.4. LiB$_8^-$ half sandwich and Fe(B$_8$)$_2^{2-}$ sandwich structures

The perfectly symmetric and doubly aromatic molecular wheel B$_8^{2-}$ (D_{7h}, $^1A_1'$) species is an excellent candidate for a new inorganic ligand or a new building block. In order to probe the possibility to form a salt-like charge transfer complex between B$_8^{2-}$ and an alkali metal cation, we performed a joint experimental and theoretical study of the LiB$_8^-$ cluster [165]. We found computationally that LiB$_8^-$ in its global minimum half sandwich structure indeed contains a B$_8^{2-}$ ligand of the wheel shape. Fig. 35 also contains the delocalized MOs of the C_{7v} ($^1A_1$) structure, and one can see that the doubly aromatic character of B$_8^{2-}$ is preserved inside of this salt-like LiB$_8^-$ anion (Fig. 35).

The Li-atom is coordinated to the plane of the ligand above the center of the wheel. Structures in which the Li-atom was coordinated to the side or to the vertex of the wheel, were found to be first-order saddle points on the potential energy surface. An additional proof that this structure is indeed a global minimum structure comes from comparing the experimental photoelec-

tron spectrum of this anion with theoretically calculated VDEs (Fig. 36 and Table 24) [165].

A good agreement between the theory and the experiment was found, which confirms our assignment of the global minimum structure.

Fig. 36. Photoelectron spectrum of LiB$_8^-$ at 193 nm. (Reprinted with permission from Ref. [165]. Copyright 2004 American Chemical Society.)

Table 24
Experimental and theoretical VDEs (in eV for LiB_8^- [165]

Observed features	VDE (experimental)	Molecular orbital	VDE (theoretical), ROVGF/6-311+G(2df)	VDE (theoretical), TD B3LYP/6-311+G(2df)
X	3.09 ± 0.05	HOMO ($3e_1$)	3.39 (0.90)[a]	3.27
A	4.40 ± 0.04	HOMO-1 ($2e_1$)	4.83 (0.90)[a]	4.66
B	5.7 ± 0.1	HOMO-2 ($2a_1$)	5.87 (0.87)[a]	5.58

[a] Numbers in parentheses indicate the pole strength.

Fig. 37. Lowest-energy structures of nonaatomic cationic, neutral and anionic clusters. (Reprinted with permission from Ref. [70]. Copyright 2003 Wiley.)

Li et al. [166] predicted computationally that a remarkable D_{7h} sandwich-type of the $(B_8)_2Fe^{2-}$ dianion with two B_8-ligands sandwiching the Fe^{2+} cation is a minimum on the potential energy surface. However, the authors did not address the issue of catenation between two B_8^{2-} groups. Thus, more work should be done on sandwich species with all-boron clusters. However, if such species were confirmed, it would be a truly remarkable breakthrough in all-boron cluster coordination chemistry.

Table 25
Molecular properties of the B_9 and B_9^- global minima [70]

	B_9 (D_{2h}, $^2B_{1g}$)		B_9^- (D_{8h}, $^1A_{1g}$)		
	B3LYP/6-311+G*[a]	RCCSD(T)/6-311+G*[a]	B3LYP/6-311+G*[a]	CASSCF/6-311+G*[a]	CCSD(T)/6-311+G*[a]
E_{total} (a.u.)	−223.415132	−222.678750	−223.4128673	−221.9934254	−222.8010847
NImag	0	b	0	0	b
Geometry	$R(B_1-B_{2,6}) = 1.918$ Å	$R(B_1-B_{2,6}) = 1.954$ Å	$R(B_1-B_{2-9}) = 1.976$ Å	$R(B_1-B_{2-9}) = 1.981$ Å	$R(B_1-B_{2-9}) = 2.004$ Å
	$RB_1-B_{3,5,7,9} = 1.981$ Å	$RB_1-B_{3,5,7,9} = 2.009$ Å			
	$R(B_1-B_{4,8}) = 2.058$ Å	$R(B_1-B_{4,8}) = 2.079$ Å			
	$\angle B_2-B_1-B_3 = 46.2°$	$\angle B_2-B_1-B_3 = 46.1°$			
Frequencies (cm^{-1})	$\nu_1(a_g) = 1271$	b	$\nu_1(a_{1g}) = 727$	$\nu_1(a_{1g})$ 749	b
	$\nu_2(a_g) = 723$	b	$\nu_2(a_{2u}) = 427$	$\nu_2(a_{2u})$ 440	b
	$\nu_3(a_g) = 449$	b	$\nu_3(b_{1g}) = 471$	$\nu_3(b_{1g})$ 521	b
	$\nu_4(a_g) = 245$	b	$\nu_4(b_{2g}) = 1655$	$\nu_4(b_{2g})$ 1713	b
	$\nu_5(a_u) = 172$	b	$\nu_5(b_{2u}) = 395$	$\nu_5(b_{2u})$ 437	b
	$\nu_6(b_{1g}) = 392$	b	$\nu_6(e_{1u}) = 908$	$\nu_6(e_{1u})$ 938	b
	$\nu_7(b_{2g}) = 300$	b	$\nu_7(e_{1u}) = 262$	$\nu_7(e_{1u})$ 297	b
	$\nu_8(b_{3g}) = 1658$	b	$\nu_8(e_{2u}) = 200$	$\nu_8(e_{2u})$ 239	b
	$\nu_9(b_{3g}) = 968$	b	$\nu_9(e_{3u}) = 1273$	$\nu_9(e_{3u})$ 1309	b
	$\nu_{10}(b_{1u}) = 1450$	b	$\nu_{10}(e_{3u}) = 418$	$\nu_{10}(e_{3u})$ 469	b
	$\nu_{11}(b_{1u}) = 929$	b	$\nu_{11}(e_{2g}) = 1477$	$\nu_{11}(e_{2g})$ 1537	b
	$\nu_{12}(a_{2u}) = 1512$	b	$\nu_{12}(e_{2g}) = 278$	$\nu_{12}(e_{2g})$ 349	b
	$\nu_{13}(a_{2u}) = 853$	b	$\nu_{13}(e_{3g}) = 364$	$\nu_{13}(e_{3g})$ 404	b
	$\nu_{14}(a_{2u}) = 485$	b			
	$\nu_{15}(b_{2u}) = 94$	b			
	$\nu_{16}(b_{3u}) = 410$	b			
	$\nu_{17}(b_{3u}) = 391$	b			
	$\nu_{18}(b_{3u}) = 388$	b			
	$\nu_{19}(b_{3u}) = 385$	b			
	$\nu_{20}(a_{3u}) = 160)$	b			
	$\nu_{21}(a_{3u}) = 58$	b			

[a] Method.
[b] Frequencies were not calculated at this level of theory.

3.8. Nonaatomic clusters: B_9, B_9^+, B_9^-

3.8.1. B_9^+

Nonaatomic pure-boron clusters are less studied than all systems discussed so far. Two different structures have been reported by Kato et al. [122], and by Boustani [127], as global minimum structures for B_9^+, which are shown in Fig. 37 as structures I and II, respectively.

Ricca and Bauschlicher [61,128] also reported the global minimum structure II, C_s ($^1A'$).

3.8.2. B_9

We found the slightly distorted D_{2h} ($^2B_{1g}$) wheel-structure III (Fig. 37) to be the global minimum of the B_9 cluster from our GEGA search (B3LYP/3-21G) and follow-up calculations at the B3LYP/6-311+G* and RCCSD(T)/6-311+G* levels of theory [70,135]. The result is a little different from that obtained by Kato et al. [122], who found the planar C_{2v} $^2A_1$ to be the global minimum structure. Boustani [62] reported a nonplanar C_s structure, which is similar to that of the cation (Fig. 37, structure II). However, we found that this structure is 10.4 kcal/mol higher in energy (B3LYP/6-311+G*) [70] than our global minimum structure D_{2h} $^2B_{1g}$. According to our calculations, a distorted heptagonal bipyramid C_{2v} $^2A_1$ (Fig. 37, structure IV) is the lowest (3.2 kcal/mol at B3LYP/6-311+G*) alternative B_9 isomer. Calculated molecular properties of the B_9 D_{2h} $^2B_{1g}$ global minimum structure are summarized in Table 25.

3.8.3. B_9^-

For the anionic B_9^- cluster, we found from GEGA search (B3LYP/3-21G) and follow-up higher-level calculations (B3LYP, CASSCF, and UCCSD(T) with 6-311+G* basis set) that the perfect planar D_{8h} $^1A_{1g}$ wheel-shape structure is the global minimum (Fig. 37, structure V) [70,135]. According to our calculations at B3LYP/6-311+G*, there is no isomer within 14 kcal/mol. The perfect octagon structure of B_9^- is unprecedented in chemistry and represents the first example of octacoordinated atom in a planar environment.

In order to verify these theoretical results we recorded photoelectron spectra at several wavelengths. The PES spectra of B_9^- at 266 nm and 193 nm are shown in Fig. 38.

Theoretically calculated VDEs for the major features X and A at the ROVGF/6-311+G(2df) and CCSD(T)/6-311+G(2df) levels of theory are presented in Table 26.

Good agreement between two levels of theory and observed features X and A was achieved.
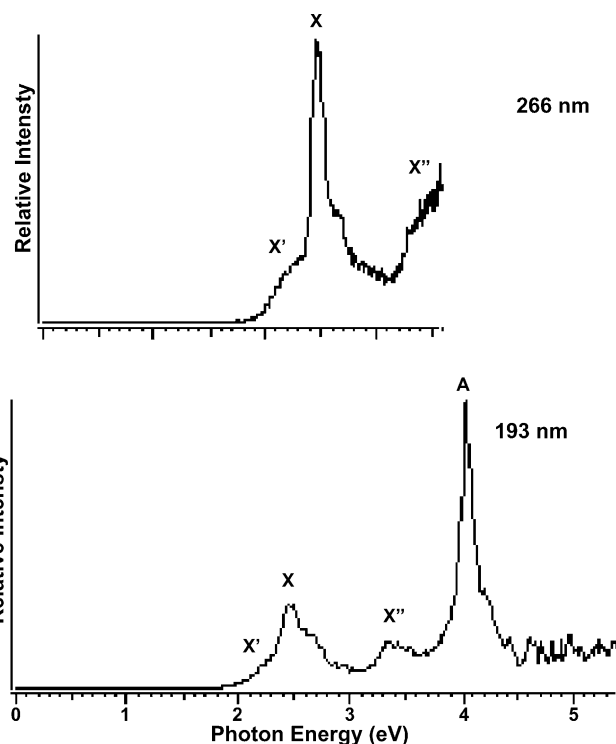

Fig. 38. Photoelectron spectra of B_9^-. (Reprinted with permission from Ref. [70]. Copyright 2003 Wiley.)

The remarkable planar octagon structure of B_9^- can be easily rationalized on the basis of the presence of doubly (σ- and π-) aromaticity (Fig. 39).

As before, we can use the NBO analysis and localize eight MOs: HOMO-3 ($1b_{2g}$), HOMO-5, HOMO-5' ($1e_{3u}$), HOMO-6, HOMO-6' ($1e_{2g}$), HOMO-7, HOMO-7' ($1e_{1u}$), and HOMO-8 ($1a_{1g}$) into eight 2c-2e B–B peripheral bonds. The other valence MOs are delocalized over the octagon, and they are responsible for global bonding between the central B atom and peripheral B atoms. The three π-MOs: HOMO, HOMO' ($1e_{1g}$), and HOMO-2 ($1a_{2u}$), are responsible for π-aromaticity, and the three σ-MOs: HOMO-1, HOMO-1' ($2e_{1u}$), and HOMO-4 ($2a_{1g}$), are responsible for σ-aromaticity in B_9^- [70].

If we delete one electron in the B_9^- anion from the doubly degenerate $1e_{1g}$-HOMO, the resulting neutral B_9 cluster undergoes the Jahn–Teller deformation toward D_{2h} ($^2B_{1g}$) symmetry and that explains its global minimum structure. Thus, the neutral B_9 cluster is σ-aromatic and partially π-antiaromatic [70].

Similar chemical bonding picture can be expected in the valence isoelectronic CB_8, SiB_8, and PB_8^+ species. The planar structures and π-aromatic (with six π-electrons) character

Table 26
Experimental and theoretical vertical detachment energies (in eV) for B_9^- [70]

Observed features	VDE (experimental)[a]	Molecular orbital	Final state	VDE (theoretical), ROVGF/6-311+G(2df)	VDE (theoretical), CCSD(T)/6-311+G(2df)
X	3.46 (6)	HOMO ($1e_{1g}$)	$^2E_{1g}$	3.38	3.47
A	5.04 (6)	HOMO-1 ($1e_{1u}$)	$^2E_{1u}$	4.84	5.07
		HOMO-2 ($1a_{2u}$)	$^2A_{2u}$	5.79	

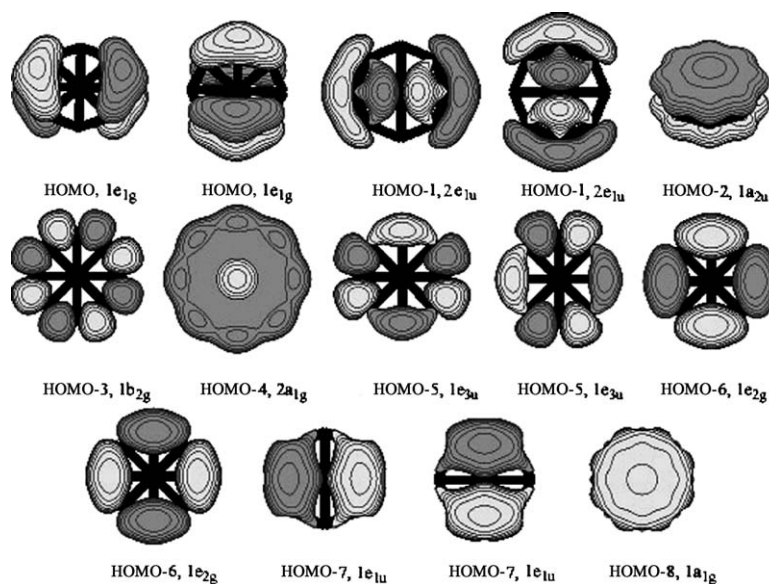[a] Numbers in parentheses indicate the uncertainties of the last digit.

Fig. 39. Molecular orbital picture of the B_9^- (D_{2h}, $^1A_{1g}$) cluster. (Reprinted with permission from Ref. [70]. Copyright 2003 Wiley.)

in CB_8, SiB_8, and PB_8^+ species was reported by Minkin and Minyaev [167] and by Minyaev et al. [168]. The authors found, however, that in the case of octa-coordinated carbon, the B_8-cycle is too large in comparison to the B–C distance. The D_{8h} structure of CB_8 is a second-order saddle point. The normal mode displacements lead to a C_{2v} ($^1A_1$) structure, in which the central C-atom is shifted to the side [168]. However, the barrier to the intramolecular rearrangement is rather small, allowing one to consider the fluxional CB_8 system as one with -effective octa-coordination of the central atom. The two other clusters, SiB_8 and PB_8^+, were found to have a perfect octagonal structure. We would like to add that, in addition to π-aromaticity of CB_8, SiB_8, and PB_8^+ species, they are also σ-aromatic systems with six σ-globally delocalized electrons, and with eight 2c-2e B–B peripheral bonds similar to what we found for B_9^-.

B_9^- is indeed another example of a closed-shell doubly aromatic, perfectly stable planar wheel that can be used as a new ligand or a new structural block for inorganic molecules and solids.

3.9. The 10-atomic clusters B_{10}^+, B_{10}, B_{10}^-

3.9.1. B_{10}^+

According to Ricca and Bauschlicher [61], B_{10}^+ has a C_{2v} $^2B_1$ global minimum structure of the convex shape having two hexagonal pyramids as subunits (Fig. 40) at B3LYP/6-311+G*.

The same ground electronic state was reported by Boustani [127].

3.9.2. B_{10}

The global minimum structure of B_{10}, according to Zhai et al. [71], is a C_{2h} (^1A_g) structure (Fig. 41) at PW91/TZ2P, which is quasi-planar with eight boron atoms forming a distorted ring around two atoms at the center, with one of the center atoms being above the plane and another one below the plane. The same structure was also reported by Cao et al. [158]. Kato et al. [122]
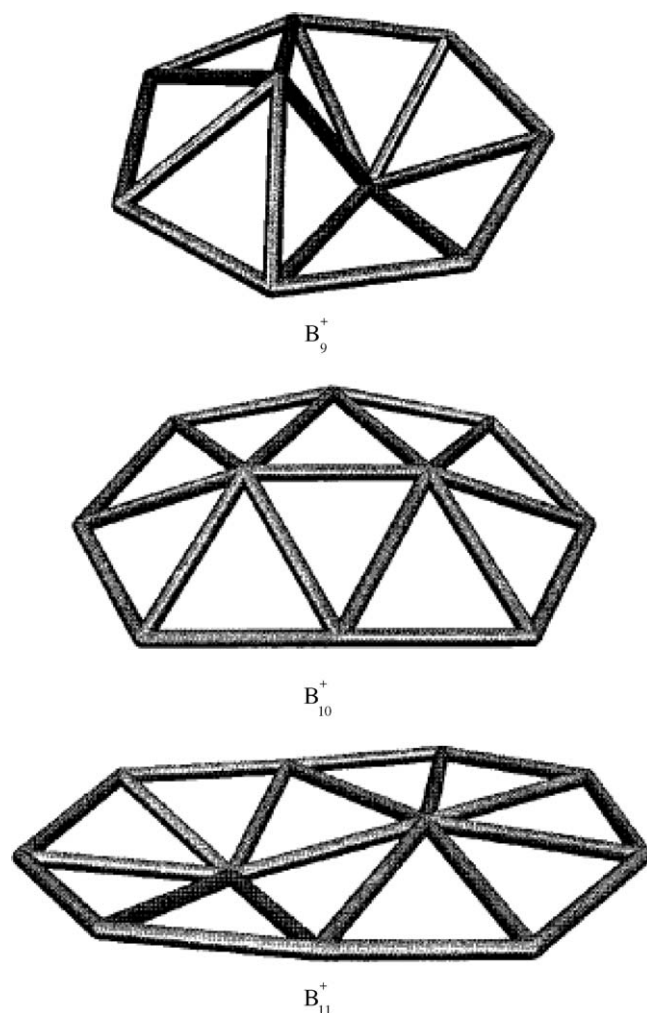

Fig. 40. The optimal B3LYP/6-31G* geometries for B_9^+ to B_{11}^+. (Reprinted with permission from ref. [61]. Copyright 1996 Elsevier.)
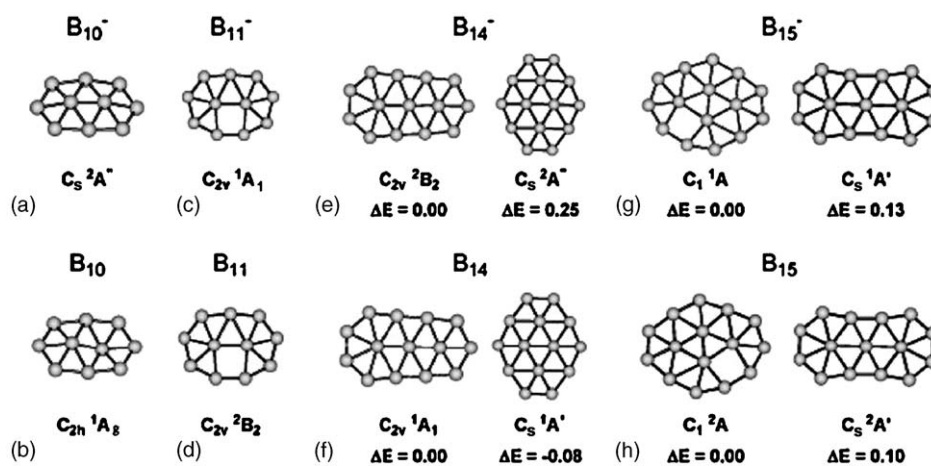
Fig. 41. (a–h) The low-lying structures of B_{10}^-, B_{11}^-, B_{14}^-, and B_{15}^- and their neutrals. The relative energies are in eV. (Reprinted with permission from Ref. [71]. Copyright 2003 Nature Publishing Group.)

reported the planar C_{2v} global minimum structure and the convex C_{2v} structure was predicted by Boustani at LSD/[621/321] [62].

The chemical bonding analysis of the global minimum structure of B_{10} was performed for the π-system, and it was shown that this structure has six π-electrons, and thus it is a π-aromatic system (Fig. 42) [71].

In a recent article [169], σ-electrons were also included into the discussion of chemical bonding in B_{10}. It was shown that NBO analysis revealed eight peripheral 2c-2e B–B bonds and one 2c-2e bond between the two central boron atoms. Three MOs are responsible for the global π-bonding, and then the remaining three σ-MOs are responsible for the global σ-bonding. Thus, B_{10} is a doubly (σ- and π-) aromatic cluster.

For B_{10}, we also tested a doubly aromatic planar cluster, D_{9h} $^1A_1'$, with only one boron atom at the center. It was found to be significantly higher in energy (60.5 kcal/mol at B3LYP/6-311+G*) than the global minimum C_{2h} ^1A_g structure. That

is because the cavity in the D_{9h} $^1A_1'$ structure is too large ($r = 2.202$ Å) for one boron atom, the structure C_{2h} ^1A_g with two centered boron atoms (although they do not fit perfectly in the planar structure) is more stable. Thus, in our chemical bonding discussion we need to take into account not only electronic factors, but also the geometric considerations.

3.9.3. B_{10}^- and its photoelectron spectra

Zhai et al. [71] reported a slightly nonplanar structure C_s $^2A''$ (Fig. 41), as the global minimum for B_{10}^- at PW91/TZ2P. Photoelectron spectra of B_{10}^- (Fig. 43) recorded at 193 nm and 266 nm reveal two distinct features, X and A, in the low energy part of the spectra with a rather broad feature between 4.5 eV and 6 eV.

In Table 27 we summarize the experimental VDEs and ADE of B_{10}^- and compare them with the theoretical VDEs and ADE. One can see that the two features, X and A, cor-
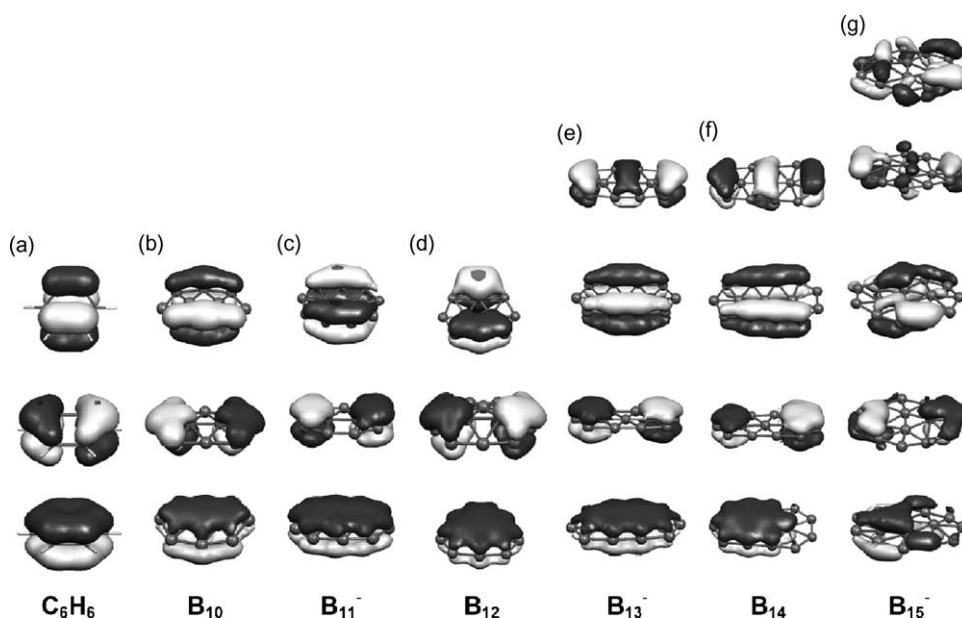

Fig. 42. Comparison of the occupied π molecular orbitals (MOs) of benzene with those of boron clusters. The π-MOs are given for: (a) benzene, (b) B_{10}, (c) B_{11}^-, (d) B_{12}, (e) B_{13}^-, (f) B_{14}^-, and (g) B_{15}^-. (Reprinted with permission from Ref. [71]. Copyright 2003 Nature Publishing Group.)
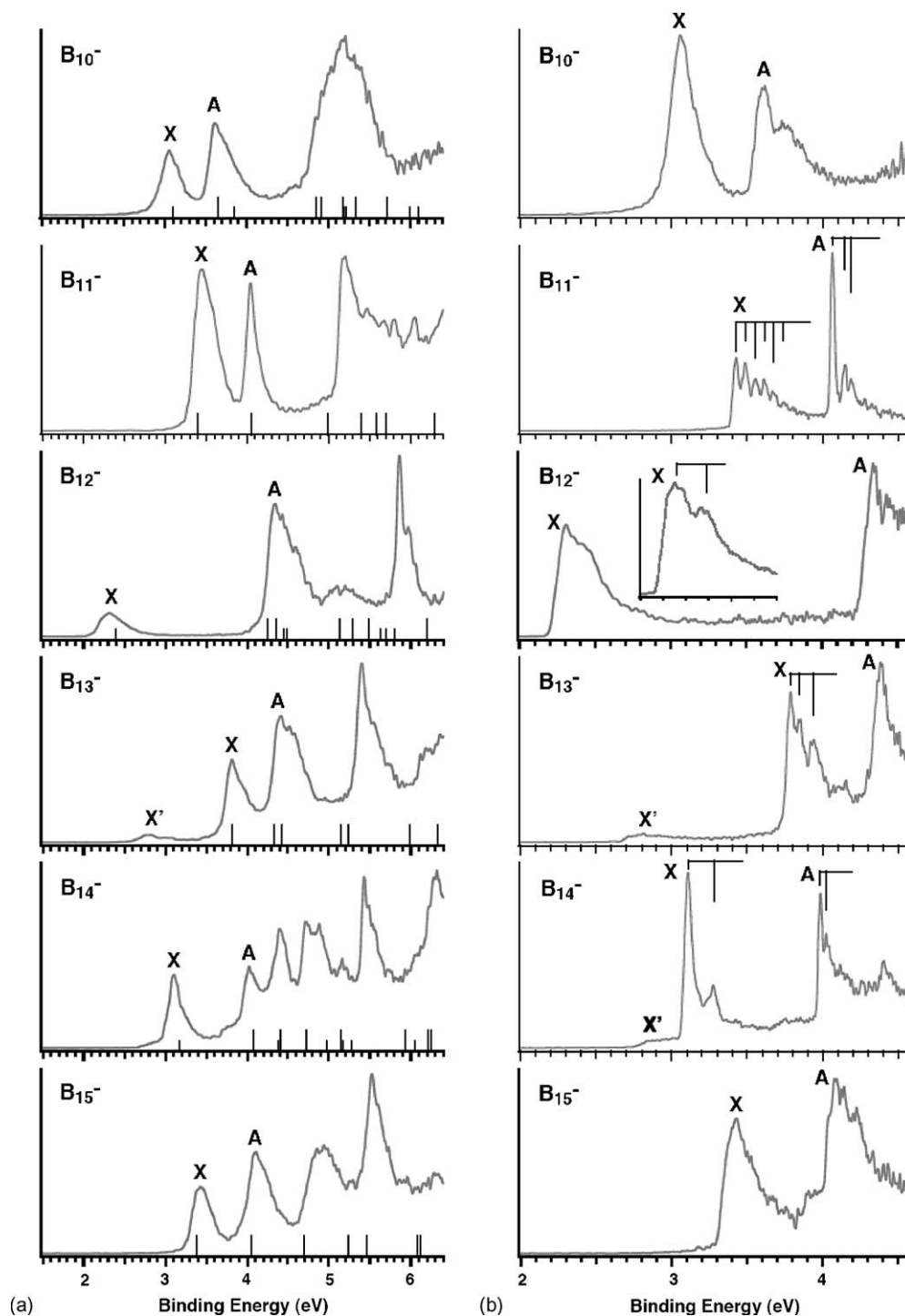
Fig. 43. Photoelectron spectra of B_n^- ($n = 10$–15). (a) At 193 nm. The vertical bars off the binding energy axis represent the calculated vertical electron detachment energies for the lowest anion structures (see Figs. 41 and 45). For even-sized clusters, the shorter bars represent detachment transitions to singlet neutral states, whereas the longer bars represent transitions to triplet final states. (b) At 266 nm. The inset in the frame of B_{12}^- shows the spectrum of B_{12}^- at 355 nm. The vertical lines above the spectra indicate resolved vibrational structures. (Reprinted with permission from Ref. [71]. Copyright 2003 Nature Publishing Group.)

responding to electron detachment from HOMO ($7a''$) and HOMO-1 ($6a''$), and the next five electron detachment channels correspond to the broad features at higher binding energies. Good agreement between theory and experiment confirmed that the structure C_s $^2A''$ is indeed the global minimum structure [71].

3.10. The 11-atomic clusters B_{11}^+, B_{11}, B_{11}^-

3.10.1. B_{11}^+

Ricca and Bauschlicher [61] reported a quasi-planar C_s $^1A'$ structure for B_{11}^+ at B3LYP/6-31G*. It can be considered as a B_7^+ subunit sharing four atoms with a B_8^+ subunit (Fig. 40).

Table 27
Experimental and theoretical adiabatic (ADE) and vertical (VDE) detachment energies of B_{10}^-

Feature	Experimental		Theoretical[a]		
	ADE	VDE	MO	ADE	VDE
B_{10}^- X	2.88 ± 0.09	3.06 ± 0.03	$7a''$	2.84	3.10
A		3.61 ± 0.04	$6a''$		3.65
			$9a'$		4.85
			$8a'$		4.92
			$5a''$		5.19
			$7a'$		5.34
			$4a''$		5.84

All energies are in eV [71].
  [a] VDE and ADE calculated at the PW91/TZ2P level of theory.

Table 28
Experimental and theoretical adiabatic (ADE) and vertical (VDE) detachment energies of B_{11}^-

Feature	Experimental		Theoretical[a]		
	ADE	VDE	MO	ADE	VDE
B_{11}^- X	3.426 ± 0.010	3.426 ± 0.010	$6b_2$	3.27	3.38
A		4.065 ± 0.010	$2b_1$		4.05
			$8a_1$		4.99
			$1a_2$		5.41
			$7a_1$		5.59
			$5b_2$		5.71
			$6a_1$		6.32

All energies are in eV [71].
  [a] VDE and ADE calculated at the PW91/TZ2P level of theory.

Boustani reported a similar, but planar C_s $^1A'$ structure to be the global minimum for B_{11}^+ at LSD/[621/321] [127].

3.10.2. B_{11}

Zhai et al. [71] reported a perfectly planar C_{2v} $^2B_2$ structure (Fig. 41) for B_{11} at PW91/TZ2P, which is built out of nine peripheral boron atoms with two additional atoms located at the center of the nine-atom circle. Boustani [62] also reported a similar planar structure but with a lower symmetry C_s $^2A''$.

3.10.3. B_{11}^- and its photoelectron spectra

The global minimum structure C_{2v} $^1A_1$ for B_{11}^- reported by Zhai et al. [71] at PW91/TZ2P is the same as a global minimum structure of B_{11} with the additional electron occupying the same HOMO in both structures, and, therefore, the anionic and neutral structures have very close geometries.

The PES spectrum of B_{11}^- at 266 nm is vibrationally well resolved, which is surprising for a cluster with so many atoms (Fig. 43). This is readily rationalized on the basis of the identified ground state structures for the neutral and anion. As we mentioned above, the structural changes from the ground state of B_{11}^- to that of B_{11} are relatively minor and they both have the same C_{2v} symmetry, explaining why only two vibrational modes are active during photodetachment and responsible for the relatively simple vibrational progressions observed in the 266 nm spectrum (Fig. 43).

In Table 28, we summarize the experimental VDEs and ADE of B_{11}^-, and compare them with theoretical values.

One can see that the two features, X and A, corresponding to electron detachment from HOMO ($6b_2$) and HOMO-1 ($2b_1$), and the next five electron detachment channels correspond to the broad features at higher binding energies. Because both the anionic and neutral structures have the same symmetry, only totally symmetric vibrational modes can be active during photodetachment. The high frequency mode observed in the 266 nm spectrum of B_{11}^- has a frequency of 1040 ± 50 cm^{-1}, and it agrees well with the calculated frequency 1092 cm^{-1} corresponding primarily to the B–B stretching of the inner two atoms. The lower frequency mode has an observed frequency of 480 ± 40 cm^{-1}, and it also agrees well with the calculated frequency, 481 cm^{-1}, that corresponds primarily to the stretch-

ing of the peripheral atoms relative to the two inner atoms. Excellent agreement found for VDEs, ADE, and the vibrational frequencies provides solid evidence for the theoretically predicted structures of C_{2v}, $^2B_2$ (B_{11}), and C_{2v}, $^1A_1$ (B_{11}^-).

The B_{11}^- cluster was found to be π-aromatic [71] on the basis of the presence of three doubly occupied π-MOs (Fig. 42) resulting in the presence of six π-electrons similar to that in the prototypical π-aromatic benzene molecule. The chemical bonding description in B_{11}^- has been extended by analyzing also the σ-MOs [169]. It is shown that NBO analysis revealed nine 2c-2e peripheral B–B bonds and one 2c-2e B–B bond corresponding to bonding between the two central atoms. Four other σ-MOs are responsible for the global bonding between the two central boron atoms and the nine peripheral boron atoms. Thus, B_{11}^- is a cluster with conflicting aromaticity (π-aromatic and σ-antiaromatic). However, σ-antiaromaticity in B_{11}^- could also be interpreted as island aromaticity (see Ref. [169] for details).

3.11. The 12-atomic clusters B_{12}^+, B_{12}, B_{12}^-

3.11.1. B_{12}^+

The B_{12}^+ cluster has a C_1 ^2A convex global minimum structure (at B3LYP/6-31G*) consisting of three hexagonal pyramids as subunits (Fig. 44) according to Ricca and Bausclisher [61].

Boustani [127] reported a similar structure but with higher C_{3v} symmetry at LSD/[621/321]. Because the B_{12} icosahedron is a structural unit that dominates several allotropic forms of boron, the icosahedron B_{12}^+ structure has also been calculated by Ricca and Bauschlicher [61]. They found that it is more than 70 kcal/mol higher in energy.

3.11.2. B_{12}

The PES spectra of the B_{12}^- anion indicate that indeed the B_{12} cluster represents a very unique chemical species among all boron clusters, i.e., it has a large HOMO–LUMO gap (2.0 eV) [71]. The large HOMO–LUMO gap revealed in the PES spectra of B_{12}^- indicates that B_{12} must be electronically extremely stable and should be chemically inert. At first glance, it would be tempting to associate this high stability of the B_{12} cluster to the icosahedral B_{12} unit so prevalent in bulk boron crystals and compounds. However, an extensive computational search for the structures of B_{12} performed by Zhai et al. [71] revealed
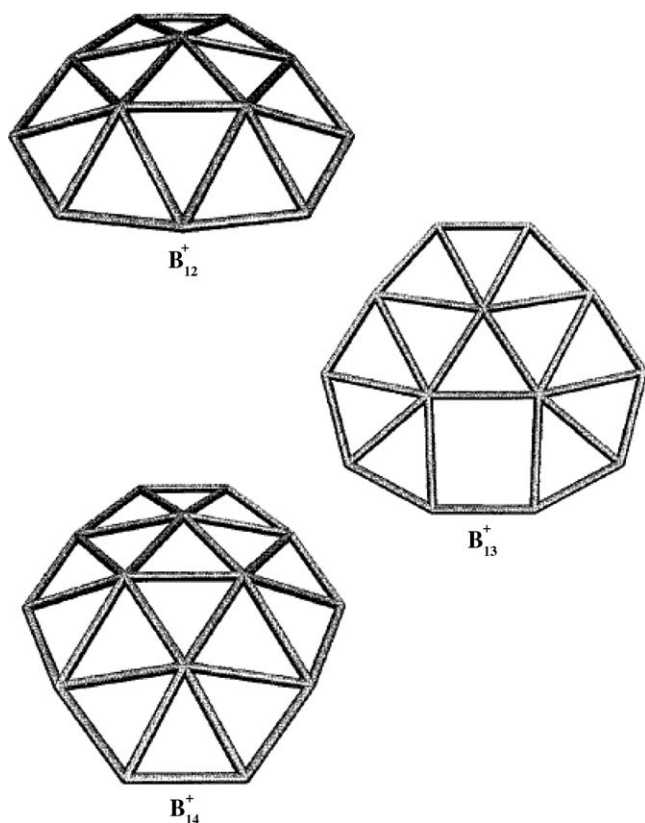
Fig. 44. The optimized B3LYP/6-31G* geometries for B_{12}^+ to B_{14}^+. (Reprinted with permission from Ref. [61]. Copyright 1996 Elsevier.)

that the icosahedron-like structure is about 70 kcal/mol higher than the global minimum quasi-planar convex structure C_{3v} $^1A'$ (Fig. 45).

The same global minimum structure for B_{12} was also reported by Boustani [127] at LSD/[621/321].

Zhai et al. have shown that B_{12} is a π-aromatic system because it has six π-electrons occupying three globally delo-

calized MOs (Fig. 42) similar to the prototypical π-aromatic benzene molecule. It has been further shown that B_{12} is not only π-aromatic, but it is also a σ-aromatic system [169]. Out of the 18 valence MOs 9 σ-MOs are responsible for 9 2c-2e B–B peripheral bonds, and 3 σ-MOs are responsible for 3 2c-2e B–B bonds between the 3 central boron atoms (see Ref. [169] for an alternative explanation). The remaining three σ-MOs are responsible for delocalized global bonding between the three central boron atoms and the nine peripheral boron atoms. Thus, if we ignore a small deviation from planarity in the B_{12} cluster, it is a doubly (σ- and π-) aromatic system which explains its round shape and large HOMO–LUMO gap experimentally observed in the PES spectra of B_{12}^-.

3.11.3. B_{12}^- and its photoelectron spectra

The global minimum structure C_s $^2A'$ (Fig. 45) for B_{12}^- reported by Zhai et al. [71] at PW91/TZ2P is similar to the global minimum structure of B_{12} with the additional electron occupying the doubly degenerate LUMO, which leads to a modest distortion of the C_{3v} structure of B_{12} to the C_s structure of B_{12}^-.

The photoelectron spectra of B_{12}^- were obtained by Zhai et al. [71] at 266 nm and 193 nm (Fig. 43), and they revealed an unusually large difference between the VDEs of X and A, corresponding to a large HOMO–LUMO gap (2.0 eV) in the neutral B_{12} cluster, as we mentioned above. In Table 29, we summarize the experimental VDEs and ADE of B_{12}^-, and compare them with the theoretical values.

The characteristic PES pattern for B_{12}^- was perfectly reproduced, thus firmly establishing the quasi-planarity in B_{12}^- and B_{12}.

3.12. The 13-atomic clusters B_{13}^+, B_{13}, B_{13}^-

3.12.1. B_{13}^+

The B_{13}^+ cationic cluster attracted a lot of attention since Anderson and co-workers [53–59] reported that it has anoma-
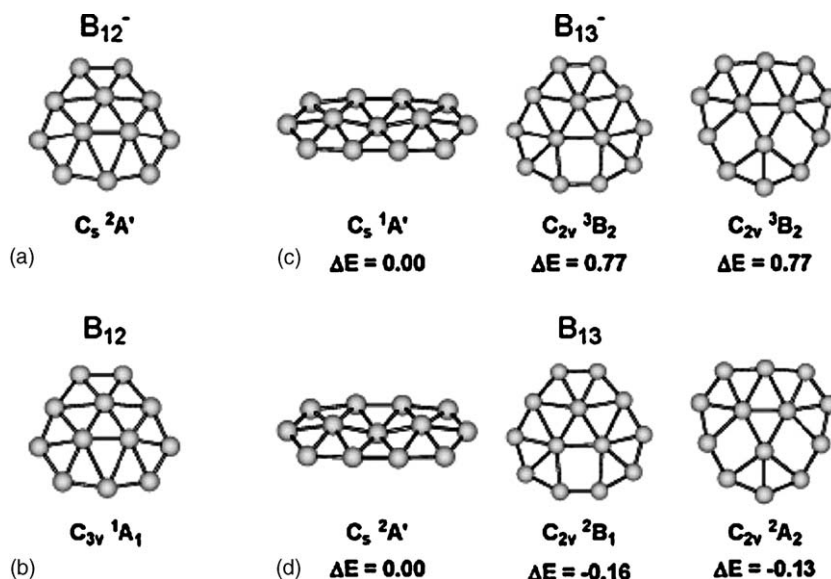

Fig. 45. (a–d) The low-lying structures of B_{12}^- and B_{13}^- and their neutrals. The relative energies are in eV. (Reprinted with permission from Ref. [71]. Copyright 2003 Nature Publishing Group.)

Table 29
Experimental and theoretical adiabatic (ADE) and vertical (VDE) detachment energies of B_{12}^-

Feature	Experimental		Theoretical[a]		
	ADE	VDE	MO	ADE	VDE
B_{12}^- X	2.21 ± 0.04	2.26 ± 0.04	$12a'$	2.25	2.38
A		4.31 ± 0.05	$11a'$		4.25
			$7a''$		4.36
			$10a'$		5.13
			$6a''$		5.29
			$9a'$		5.50
			$5a''$		6.21

All energies are in eV [71].
[a] VDE and ADE calculated at the PW91/TZ2P level of theory.

lously high stability and low reactivity compared to other cationic boron clusters. Initially this high stability was attributed to B_{13}^+ having a filled icosahedron structure [56]. Kawai and Weare [170] investigated the anomalous stability of B_{13}^+ using Car–Parrinello ab initio molecular dynamics simulations. They found that a filled icosahedral is not even a minimum on the potential energy surface. They predicted that the two most stable isomers have C_{3v} and C_s three-dimensional structures, with the C_{3v} structure being the most stable. Ricca and Bauschlicher predicted the planar C_{2v} $^1A_1$ structure (Fig. 44) as the global minimum at B3LYP/6-31G* [61]. The geometry of the global minimum structure consisted of one distorted centered hexagon and two distorted centered heptagons. They also recalculated the C_{3v} and C_s structures reported by Kawai and Weare and found that these 3D structures are appreciably (by 45 kcal/mol) higher in energy than the global minimum C_{2v} ($^1A_1$) 2D structure. Boustani [127] reported a different C_{2v} global minimum structure, which consisted of three hexagonal pyramids adjacent to one another in a longitudinal arrangement. However, Ricca and Bauschlicher found that this structure is about 28 kcal/mol higher in energy. Schleyer and co-workers [171] characterized 19 various structures of B_{13}^+ also using B3LYP/6-31G* level of theory. They concluded that the C_{2v} $^1A_1$ structure proposed by Ricca and Bauschlicher is indeed the most stable structure. Fowler and Ugalde [172] arrived to the same conclusion using the B3LYP/6-311+G(2df) level of theory. Thus, we believe that the C_{2v} $^1A_1$ structure found by Ricca and Bauschliccher is the true global minimum structure on the basis of available data in the literature.

Fowler and Ugalde were the first to propose that exceptional stability and low reactivity of B_{13}^+ is related to its aromatic character [172]. They plotted doubly occupied π-molecular orbitals for B_{13}^+, which were similar to those shown in Fig. 42. Fowler and Ugalde concluded that three doubly filled π-MOs give six π-electrons in a round system, a situation reminiscent of benzene and Hückel aromaticity. Aihara [173] evaluated the topological resonance energy (TRE) for π-electrons using graph theory. He found that the TRE of B_{13}^+ is positive in sign and very large in magnitude: TRE = $2.959|\beta_{BB}|$. This number can be compared to aromatic hydrocarbons with similar size, such as the phenalenium ($C_{13}H_9^+$) TRE = $0.410|\beta_{BB}|$,

anthracene ($C_{14}H_{10}$) TRE = $0.475|\beta_{BB}|$, and phenanthrene ($C_{14}H_{10}$) TRE = $0.576|\beta_{BB}|$. On the basis of the TRE value, B_{13}^+ is much more aromatic than polycyclic aromatic hydrocarbons of similar molecular sizes.

However, like in case of other large boron clusters, the σ-bonding was not discussed. According to our σ-bonding analysis [169] the B_{13}^+ cation is also a σ-aromatic system. Indeed, we have shown that, out of the 19 MOs, 10 σ-MOs are responsible for 10 2c-2e B–B peripheral bonds, 3 σ-MOs are responsible for 3 2c-2e B–B bonds between central boron atoms, and 3 σ-MOs are responsible for global delocalized bonding between the 3 central boron atoms and the 10 peripheral boron atoms. Like B_{12}, B_{13}^+ was a doubly (σ- and π-) aromatic system. Thus, it is its double aromaticity that is responsible for its rather round shape, extra stability, and low reactivity.

3.12.2. B_{13}

Zhai et al. [71] reported the quasi-planar C_s, $^2A'$ structure (Fig. 44) for B_{13} at PW91/TZ2P, which is built out of 10 peripheral boron atoms with 3 additional atoms forming a linear chain at the center of a distorted 10-atom circle. This structure is geometrically similar to the global minimum structure of B_{13}^+. Boustani [62] reported a different convex C_{2v}, $^2A_1$ structure, which was built out of 10 peripheral boron atoms with 3 boron atoms forming a linear chain at the center of the cluster.

3.12.3. B_{13}^- and its photoelectron spectra

The global minimum structure of B_{13}^- is a singlet elongated quasi-planar structure C_s ^1A (Fig. 45) according to Zhai et al. [71]. Two degenerate low-lying isomers were found for B_{13}^-, which are both triplet with more circular shapes and slightly different atomic connectivity.

The photoelectron spectra of B_{13}^- were obtained by Zhai et al. [71] at 266 nm and 193 nm (Fig. 43). The observation of a weak low binding energy feature (X') in the spectra of B_{13}^- indicates the coexistence of a low-lying isomer. The calculated ADE/VDE (3.69/3.81 eV) for the main isomer C_s, $^1A'$, and 2.77/2.82 eV for isomer C_{2v}, $^3B_2$ are in excellent agreement with the experimental observation. In Table 30, we summarize the experimental VDEs and ADE of B_{13}^-, and compare them with the theoretical values.

Table 30
Experimental and theoretical adiabatic (ADE) and vertical (VDE) detachment energies of B_{13}^-

Feature	Experimental		Theoretical[a]		
	ADE	VDE	MO	ADE	VDE
B_{13}^- X	3.78 ± 0.02	3.78 ± 0.02	$7a_1$	3.69	3.81
A		4.38 ± 0.06	$5b_1$		4.32
			$3a_2$		4.41
			$6a_1$		5.16
			$5b_2$		5.25
			$4b_1$		6.00
			$3b_1$		6.34

All energies are in eV [71].
[a] VDE and ADE calculated at the PW91/TZ2P level of theory.

The characteristic PES pattern for B_{13}^- was perfectly reproduced, thus firmly establishing the structure of B_{13}^-. The B_{13}^- cluster possesses eight π electrons, and is thus π antiaromatic according to the Hückel's rule, in agreement with its elongated shape [71].

3.13. The 14-atomic clusters B_{14}^+, B_{14}, B_{14}^-

3.13.1. B_{14}^+

The B_{14}^+ cluster has a C_{2v} $^2A_1$ convex global minimum structure (at B3LYP/6-31G*) consisting of four hexagonal pyramids as subunits (Fig. 44), according to Ricca and Bausclisher [61]. These results agree with the LSD calculations by Boustani [127].

3.13.2. B_{14}

Zhai et al. [71] reported a planar C_s $^1A'$ structure (Fig. 41) for B_{14} at PW91/TZ2P, which is built out of 10 peripheral boron atoms with 4 additional atoms forming a rhombus at the center of the 10-atom circle. Boustani [62] reported a convex C_{2v}, $^1A_1$ structure, which is built out of 10 peripheral boron atoms with 4 boron atoms forming a rhombus at the center of the cluster, except that the 4 inner atoms are out of plane.

There is another near isoenergetic isomer for B_{14}, which can be viewed by inserting an atom into the peripheral of the B_{13} ground state elongated structure. This isomer becomes the ground state structure for B_{14}^- (see below). Zhai et al. [71] performed molecular orbital analyses (Fig. 42) and concluded that this elongated B_{14} cluster possesses eight π-electrons and thus it is π-antiaromatic system, similar to B_{13}^- and consistent with its elongated shape.

3.13.3. B_{14}^- and its photoelectron spectra

Zhai et al. [71] reported a planar C_{2v} $^2A_2$ structure (Fig. 41) for B_{14}^- at PW91/TZ2P, which is built out of 11 peripheral boron atoms with 3 additional atoms forming a chain at the center of a distorted circle. This structure is similar to the antiaromatic low-lying isomer of the neutral B_{14} (see above), whereas the lowest isomer C_s $^2A''$ (Fig. 41) is 0.25 eV higher in energy and is similar to the global minimum structure of B_{14}.

The photoelectron spectra of B_{14}^- were measured by Zhai et al. [71] at 266 nm and 193 nm (Fig. 43). Weak features at the low binding energy part due to low-lying isomers were also observed in the PES spectra of B_{14}^- (X', Fig. 43). In Table 31 we summarize the experimental VDEs and ADE of B_{13}^- and compare them with theoretical VDEs and ADE.

The characteristic PES pattern for B_{14}^- was well reproduced, thus firmly establishing the structure of B_{14}^-.

3.14. The 15-atom clusters B_{15}, B_{15}^-

3.14.1. B_{15}

To the best of our knowledge, there have been no calculations on B_{15}^+. Zhai et al. [71] reported a planar C_1 ^2A structure (Fig. 41) for B_{15} at PW91/TZ2P, which is built out of 11 peripheral boron atoms with 4 additional atoms forming a rhombus at the center of the 11-atom circle. MO analysis showed that B_{15}

Table 31
Experimental and theoretical adiabatic (ADE) and vertical (VDE) detachment energies of B_{14}^-

Feature	Experimental		Theoretical[a]		
	ADE	VDE	MO	ADE	VDE
B_{14}^- X	3.102 ± 0.010	3.102 ± 0.010	$2a_2$	3.14	3.17
A		3.984 ± 0.010	$3b_1$		4.08
			$1a_2$		4.40
			$7b_2$		4.71
			$10a_1$		5.16
			$9a_1$		5.95
			$2b_1$		6.23

All energies are in eV [71].
[a] VDE and ADE calculated at the PW91/TZ2P level of theory.

possesses 10 π electrons and is thus aromatic, consistent with its relatively round shape [71].

3.14.2. B_{15}^- and its photoelectron spectra

Zhai et al. [71] reported a planar C_1 ^1A structure (Fig. 41) for B_{15}^- at PW91/TZ2P, which is similar to the ground state of B_{15}. The lowest isomer C_s $^1A'$ (Fig. 41) has an elongated structure composed out of two seven-member rings sharing one peripheral atom, which is about 0.13 eV higher in energy (Fig. 41).

The photoelectron spectra of B_{15}^- were obtained by Zhai et al. [71] at 266 nm and 193 nm (Fig. 43). In Table 32 we summarize the experimental VDEs and ADE of B_{13}^- and compare them with theoretical VDEs and ADE.

The characteristic PES pattern for B_{15}^- was well reproduced, thus firmly establishing the structure of B_{15}^-.

From B_{10} to B_{15}, the number of π electrons varies from 6 (B_{10}, B_{11}^-, B_{12}) to 8 (B_{13}^-, B_{14}) to 10 (B_{15}). According to the Hückel's rules, these form a series of aromatic and antiaromatic systems. The π-aromaticity or antiaromaticity seems to govern the global shape of the clusters, similar to that found in cyclic hydrocarbon molecules. Based on these observations, Zhai et al. [71] proposed the concept of hydrocarbon analogies in pure boron clusters. For example, the very special B_{12} cluster can be viewed as the "benzene analog" of boron clusters, whereas B_{11}^- can be compared to $C_5H_5^-$. The elongated antiaromatic B_{13}^- or B_{14} can be compared with C_4H_4 or C_8H_8.

Table 32
Experimental and theoretical adiabatic (ADE) and vertical (VDE) detachment energies of B_{15}^-

Feature	Experimental		Theoretical[a]		
	ADE	VDE	MO	ADE	VDE
B_{15}^- X	3.34 ± 0.04	3.43 ± 0.04	23a	3.24	3.37
A		4.08 ± 0.06	22a		4.05
			21a		4.69
			20a		5.25
			19a		5.47
			18a		6.09
			17a		6.13

All energies are in eV [71].
[a] VDE and ADE calculated at the PW91/TZ2P level of theory.

3.15. Planar-to-tubular structural transition at B_{20}

The establishment of planarity for pure boron clusters up to as large as 15 atoms [66–71] is highly remarkable in boron chemistry, as well as in cluster science [174]. However, it is still of interest to determine the critical size for 2D-to-3D structural transition in boron clusters. This becomes a huge challenge because of the complexity of large cluster systems and the existence of a large number of isomers. Kiran et al. [72] have shown recently, from a concerted PES and global geometry optimization theoretical study, that the transition occurs at the size of 20 atoms. Their conclusions were confirmed shortly by a follow-up theoretical work [175].

In the global minimum search, Kiran et al. [72] employed the basin-hopping global optimization method [176,177] coupled with ab initio DFT technique. More than 200 low-energy minima (with energy difference less than 0.1 hartree from the global minimum) were identified for B_{20}. For the top 10 lowest-energy isomers further optimization and vibrational frequency calculations were performed using all-electron DFT methods. The four lowest energy isomers are shown in Fig. 46, along with their relative energies at the B3LYP/6-311+G* level of theory.

The same search methods were used for both the anion and neutral clusters. However, the two potential energy surfaces are different, though both are dominated by 2D structures. In the anion potential energy surface, there exist several isomers that are close in energy. The double-ring tubular structure **1** is the most stable, followed by the elongated 2D structure **2** and the quasi-planar bowl-like structures **3** and **4**. To include entropy and temperature effects, Kiran et al. also carried out free-energy calculations at room-temperature (298 K). After this correction, both the tubular and elongated isomers become virtually equal in energy, closely followed by the bowl isomers. Under the theoretical methods employed, all these anion isomers should be considered isoenergetic. It should be noted that structures **3** and **4** are nearly identical except for the displacement of a single boron atom. Therefore, most of the properties of these two isomers are nearly identical.

However, in the neutral potential energy surface, the most stable isomer is the double-ring tubular structure **5**, and it is favored by ∼20 kcal/mol relative to the lowest energy 2D structures **6–8**. The current observations that the B_{20}^- anion favors 2D structures and the B_{20} neutral favors the tubular structure suggest that the extra electron destabilizes the double-ring tubular isomer, whereas it stabilizes the 2D isomers. Kiran et al. [72] also calculated the most stable structures for the 16–19-atom boron clusters and found that they all preferred 2D structures in both their anions and neutrals, which are experimentally confirmed by PES data (L.S. Wang, H.J. Zhai, unpublished data). It should be noted, however, that it is difficult to locate the tubular B_{20} structure, which appears as a deep and narrow well in the potential energy surface separated by huge energy barriers from the vast majority of easily accessible 2D structures. To gain further confidence, Kiran et al. [72] also performed ab initio simulated annealing with PBE96 exchange-correlational functional on B_{20}^- starting with random geometries. They found that the lowest energy structures were dominated by the 2D isomers.

To confirm computational predictions, Kiran et al. [72] also obtained B_{20}^- PES spectra and compared them with the calculations. Fig. 47 shows the PES spectra of B_{20}^- at two photon energies.
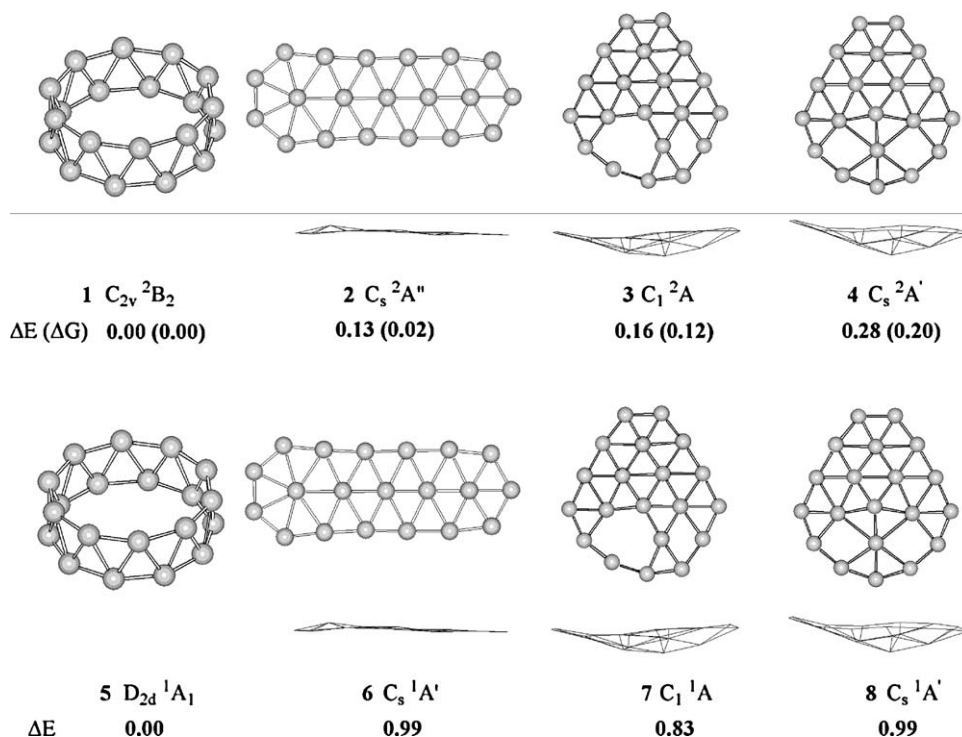

Fig. 46. Low-lying structures of B_{20}^- (**1–4**) and B_{20} (**5–8**) along with their relative energies (in eV) at B3LYP/6-311+G* level of theory. (Reprinted with permission from Ref. [72]. Copyright 2005 National Academy of Sciences.)
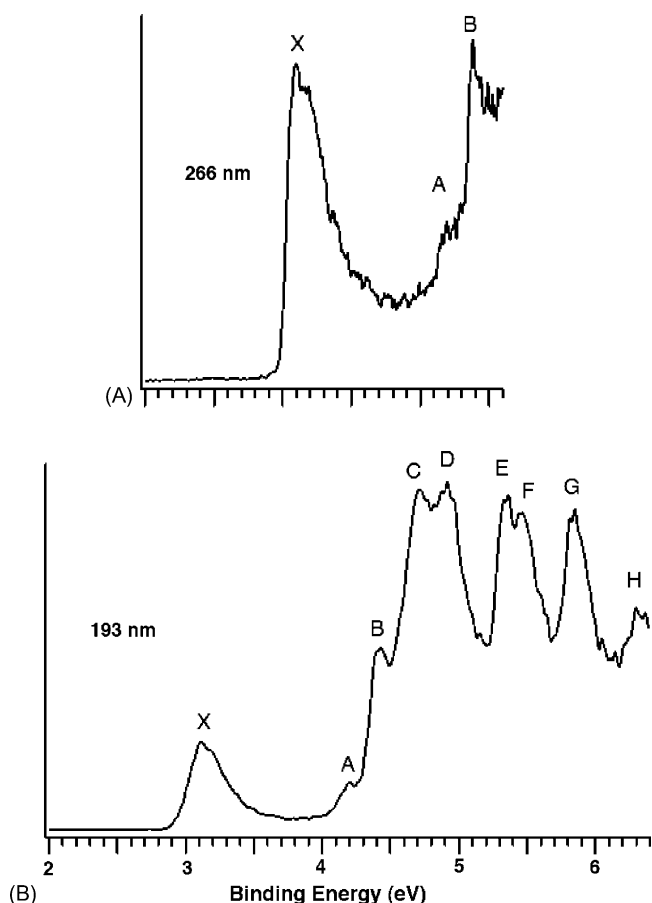
Fig. 47. Photoelectron spectra of B_{20}^- at 266 nm (A) and 193 nm (B). (Reprinted with permission from Ref. [72]. Copyright 2005 National Academy of Sciences.)

Numerous well-resolved electronic transitions (X, A–H) were observed and their electron binding energies are given in Table 33, where they are also compared with theoretical data.

The vertical detachment energy of feature X was measured from the peak maximum to be 3.11 eV. The electron affinity of neutral B_{20}, evaluated from the well-defined sharp onset of band X, is 3.02 eV. The intensity of feature A was much weaker, implying that it was likely due to a weakly populated isomer of B_{20}^- in the cluster beam. A large energy separation of $\sim$1.3 eV was observed between features X and B. This spectral pattern

suggested that neutral B_{20} is a closed-shell molecule with a large gap between its HOMO and LUMO. The current observation of B_{20} with the large HOMO–LUMO gap stimulated additional interest for a thorough investigation of its structural and electronic properties.

To confirm the computational results and facilitate comparison with the experimental data, Kiran et al. [72] calculated the VDEs and EA (Table 33). The energy difference between the anion and neutral at the anion geometry gives the first VDE and relaxing the neutral geometry to its equilibrium defines the EA. Only the 2D isomers compare favorably with the experimental values. The VDE and EA of both the elongated structure (**2**, VDE 3.15 eV, EA 3.03 eV) and the bowl isomer (**3**, VDE 2.97 eV, EA 2.88 eV; **4**, VDE 3.04 eV, EA 2.89 eV) agree well with the experimental values of 3.11 eV and 3.02 eV, respectively. However, the tubular structure **1** gives binding energies (VDE 2.32 eV, EA 2.17 eV) much lower than the experiment. Closer comparison between the experimental and theoretical data (Table 33) clearly shows that isomer **3** agrees best with the experiment: the simulated spectrum of isomer **3** has a remarkable one-to-one correspondence to the experimental spectrum. Isomer **2** gives a smaller HOMO–LUMO gap and is likely to be the minor isomer responsible for the weak feature A; the remaining electronic transitions of isomer **2** were buried in the spectra of the dominant isomer **3**. Isomer **1** did not appear to be populated at all in the B_{20}^- beam, which would have yielded a characteristic transition at lower binding energies ($\sim$2.3 eV) in the experimental spectrum. The absence of isomer **1** was likely due to the kinetic control of cluster formation. Since clusters smaller than B_{20} all have planar structures in their ground state, the planar B_{20} cluster is expected to form with the highest probability. For example, the bowl isomers **3** and **4** can be derived from B_{12} by adding seven boron atoms to the rim and one in the middle. Similarly, the elongated isomer **2** can be directly constructed by adding six additional boron atoms to one end of B_{14}. The situation of B_{20}^- is remarkably similar to the case of C_{20}^-, where the bowl and fullerene isomers cannot be produced by laser vaporization of graphite [178]. The latter method can only produce the ring isomer, which is similar to the structures of smaller carbon clusters [179–181].

Kiran et al. [72] established that the tubular isomer is almost isoenergetic to the lowest energy 2D isomers for the B_{20}^-

Table 33

Observed VDEs from photoelectron spectra of B_{20}^- and comparison with theoretical data for the three lowest-energy isomers of B_{20}^- (see Fig. 46) [72]

Feature	Experimental		Theoretical[a]		
	ADE	VDE	Structure **1**	Structure **2**	Structure **3**
X	3.02 ± 0.02	3.11 ± 0.02	2.32	3.15	2.97
A		4.20 ± 0.03	3.49	4.04	
B		4.40 ± 0.03	4.52	4.49	4.22
C		4.71 ± 0.04		4.66	4.59
D		4.92 ± 0.04		5.03	4.70
E		5.35 ± 0.04			5.21
F		5.46 ± 0.04			5.23
G		5.84 ± 0.03	5.65	5.79	5.66
H		6.33 ± 0.03	6.33	6.12	6.17

[a] VDE calculated at the B3LYP/6-311+G* level of theory.

anion, whereas it is clearly the global minimum for the B_{20} neutral. Since they have confirmed all smaller clusters prefer 2D structures, the tubular B_{20} cluster represents exactly the onset of 3D structures for the boron clusters, analogous to the onset of the fullerene structure at C_{20}. The B_{20} tubular structure can be viewed as rolling up a two-row strip of 20 B atoms: it is stabilized by the strong sp^2 hybridized σ-bonds within the wall and further enhanced by delocalized π-bonds covering the inner and outer surfaces of the wall. As a result the tubular structures are also highly aromatic, analogous to the aromaticity in the planar boron clusters [66–71]. The preference of tubular over 2D isomers is governed by the extra σ-bonding gained when rolling up the 2D boron strip and the enhanced π-bonding due to the compactness of the tubular structures, which overcome the strain energy due to the curvature. In fact, previous work on B_{10}–B_{15} already revealed evidence of fragmentation of the delocalized π-orbitals in different parts of the 2D structures (island aromaticity) in the larger planar clusters [71], which hinted possible 2D-to-3D transitions with increasing cluster sizes, because the stability derived from the 2D delocalization weakens. The tubular B_{20} suggests a mechanism for forming the thinnest boron nanotube by extending the B_{20} structure along the five-fold axis. In fact, larger diameter double-ring and multiple-ring tubular boron structures (such as B_{24} and B_{36}), among a variety of other chosen structures, have been explored computationally [182–185]. Very interestingly, a successful synthesis of single-walled boron nanotubes with a diameter of 3 nm has been reported recently [186]. The B_{20} work by Kiran et al. [72] represents the first systematic experimental and theoretical search for the smallest stable 3D boron clusters. The high stability of the tube-like B_{20} suggests the existence of a whole new class of nanotubes made of boron atoms. Indeed, the tubular B_{20} cluster may be viewed as the embryo of the thinnest boron nanotube, with a diameter of 5.2 Å.

3.16. Are all planar boron clusters highly aromatic?

A recent paper by Aihara et al. [187] claimed that all boron B_3–B_{15} clusters are highly aromatic on the basis of topological resonance energies. The calculated TREs (in terms of the resonance integral between two bonded atoms $|\beta_{BB}|$) for planar clusters and their molecular ions in the singlet electronic state are summarized in Table 34. Indeed, according to Aihara et al. all, neutral and charged boron clusters have large positive TREs. In fact, they are significantly higher than TREs for prototypical polycyclic hydrocarbons such as benzene ($0.273|\beta_{CC}|$), naphthalene ($0.389|\beta_{CC}|$), anthracene ($0.475|\beta_{CC}|$), and pyrene ($0.598|\beta_{CC}|$). In particular, they point out that B_6^{2-} with four π-electrons, several isomers of B_{13}^- with eight π-electrons, and two isomers of B_{14} with eight π-electrons are antiaromatic, according to the $4n + 2$ Hückel's rule for singlet species, but they all have large positive TREs. On the basis of the TREs, they claimed that the Hückel's rule does not hold for boron clusters. We believe this requires some clarification, and it seems that these authors did not understand our application of the Hückel's rule to boron clusters.

Table 34
TREs for planar boron clusters and their molecular ions in the singlet electronic states [187]

Species	Number of π-electrons	TRE/$|\beta_{BB}|$
B_3^-	2	0.536
B_4	2	0.852
B_5^-	2	1.052
B_6^{2-}	4	0.549
B_8^{2-}	6	0.634
B_9^-	6	0.855
B_{10}	6	1.568
B_{11}^-	6	1.798
B_{12}	6	2.605
B_{13}^+ (I)	6	2.959
B_{13}^- (III)	8	1.793
B_{14} (II)	8	2.050
B_{15}^- (I)	10	1.631

First, we would like to point out that we applied the $4n + 2$ rule for the π-electrons in order to predict the structure of boron clusters and interpret the PES spectra of these species, in particular the large HOMO–LUMO gap in some neutral boron clusters. We believe that aromaticity/antiaromaticity should be able to predict the high (aromaticity) or low (antiaromaticity) symmetry for the global minimum structure of a boron cluster. The resonance energy is only one criterion for aromaticity. One cannot rely solely on the resonance energy for making a judgment on a cluster's aromaticity or antiaromaticity. Second, we want to stress that σ-electrons are as important in explaining structure and stability of boron clusters as π-electrons. For example, the B_5^+ and B_5^- clusters both have 2π-electrons, and thus are both π-aromatic systems. However, B_5^+ has a global minimum structure, which is only slightly geometrically distorted from the high D_{5h} symmetry, and in fact, after ZPE corrections the vibrationally averaged structure has the high D_{5h} symmetry as one would expect for an aromatic molecule. Thus, π-aromaticity can explain the high symmetry structure of B_5^+. However, B_5^- which is also a π-aromatic system with 2π-electrons has a highly distorted C_{2v} structure. We proposed an explanation that B_5^+ has a high symmetry structure, because this system is π- and σ-aromatic (it has two delocalized π-electrons and two delocalized σ-electrons, see Section 3.4), while B_5^- has a low symmetry structure because although it is a π-aromatic system, it is σ-antiaromatic system (it has two delocalized π-electrons and four delocalized σ-electrons, see Section 3.4 for details). These two clusters clearly demonstrate that including σ-electrons into consideration is as important as π-electrons in order to achieve a complete understanding about how chemical bonding affects cluster structures. Many other examples can be found throughout this review article.

Going back to nonapplicability of the Hückel's rule to boron clusters on the basis of large TRE values for all boron clusters, we would like to point out that our application of the Hückel's rule enables us to explain why some clusters have high symmetry structure and other have low symmetry structure. The statement that all boron clusters are aromatic completely ignores the fact that some clusters have high symmetry, high HOMO–LUMO gaps, and their anions have low VDEs, while other have low

symmetry, low HOMO–LUMO gaps, and their anions may have high VDEs. We found that the Hückel's rule is extremely useful in explaining and most importantly in predicting structure, stability, reactivity, and photoelectron spectra of boron clusters. On the other hand, we stress that there are differences between boron clusters and aromatic polycyclic hydrocarbons, because for boron clusters we must consider aromaticity in the π-system, as well as in the σ-system. Boron clusters offer a richer variety of aromaticity than hydrocarbons, because they may be doubly (σ- and π-) aromatic, may have conflicting aromaticity (σ-aromatic and π-antiaromatic, or σ-antiaromatic and π-aromatic), or may be doubly (σ-and π-) antiaromatic.

We also believe that there is no contradiction between the findings of Aihara et al. [187] that all boron clusters have positive TRE and our conclusions that certain boron clusters are antiaromatic. Let us consider the B_6^{2-} cluster, which is antiaromatic (in fact it is doubly σ- and π-antiaromatic) according to our analysis, but which has a positive TRE and thus is aromatic according to Aihara et al. [187]. Our assignment of B_6^{2-} as a π-antiaromatic system is based on the presence of four π-electrons, its highly distorted (D_{2h}) structure, and paratropic ring currents [68,151,154]. We view this cluster as being antiaromatic *globally*. It does not, however, mean that this cluster cannot have positive resonance energy. In fact, according to our MO analysis, the π-system in B_6^{2-} can be split into two subunits, with two π-electrons localized over each of the two triangles (see Section 3.5.5). Thus, the globally antiaromatic B_6^{2-} system can be considered as having two separate aromatic subunits ("island aromaticity"). The island aromaticity is responsible for the positive TRE in B_6^{2-}. Indeed, Aihara et al. themselves stated that out of four circuit currents, three circuit currents, including the a_4 circuit current, are paratropic indicating antiaromaticity, and that the a_1 circuit currents, which are highly diatropic and which are located over the triangles, overwhelm the antiaromatic contributions from a_2–a_4. That result clearly supports the presence of island aromaticity in B_6^{2-}. We also have shown that in the Li_2B_6 gas phase molecule, the global minimum structure has the C_{2h} ($^1A_1$) structure with two Li^+ ions located above and below the B_3^- triangular areas in B_6^{2-} (Fig. 21, Section 3.5.5). These results confirmed the presence of the π-island aromaticity in the overall doubly antiaromatic system. The same explanation can be done for other π-antiaromatic systems with positive TREs. Another interesting observation that can be made from Table 34 is that the TRE in B_6^{2-} is almost two times smaller than TRE in the neighboring π-aromatic B_5^- with two π-electrons, in complete agreement with the Hückel's rule prediction. Our conclusion is that the Hückel's rule is indeed a powerful tool for predicting and interpreting structure, stability, reactivity, magnetic properties, and spectroscopic properties of boron clusters if both σ- and π-aromaticity are considered and if island aromaticity in globally antiaromatic molecules is taken into account.

4. Conclusions

The discovery that pure boron clusters are planar (up to 20 atoms) is a big surprise for the chemical community, because solid boron is built out of 3D icosohedral structural units, MB_6 solids are built out of regular octahedra of boron atoms, and boranes are known to have deltahedral structures. Thomas P. Fehlner of the University of Notre Dame has commented that the confirmation that all-boron clusters form planar wheel- and raft-like shapes rather than closed, nearly spherical clusters the way boranes do "is an important landmark in chemistry. It's reminiscent of the discovery when I was a graduate student that the inert gases are not inert. Discoveries such as these change our thinking in a major way" [174]. While the planarity of all-boron clusters is now firmly established through joint experimental and theoretical works [66–72], these clusters have not yet been found in condensed phase. Whenever that happens, the planar boron clusters will indeed change our thinking in a major way and would lead potentially to many new and unexpected chemistries.

That goal may indeed be achievable since it has already been demonstrated that salt-like clusters, such as $Li^+[B_6^{2-}]$ [154] and $Li^+[B_8^{2-}]$ [165] can be made in molecular beams, and the structures of the planar doubly charged B_6^{2-} and B_8^{2-} clusters are preserved in such complexes. We hope that this review will stimulate renewed interests in boron chemistry, and lead to the synthesis of new compounds with unprecedented planar all-boron ligands and all-boron building blocks. We expect that all-boron clusters will have a tendency toward catenation in the condense phase. Therefore, they must be protected in coordination compounds from forming bonds between individual boron clusters. In the solid state, we think that in order to prevent catenation between all-boron clusters, one should either look for highly charged boron clusters as building blocks such as those found in the Zintl phase or use ligand protections.

In a series of articles [66–72] we demonstrated that the Hückel's rule, which was initially developed for cyclic aromatic hydrocarbons, could also be a powerful tool in predicting and explaining structure, stability, magnetic properties, reactivity, and other molecular properties of all-boron clusters if one takes into account that aromaticity should be applied to both σ- and π-electrons, and that global antiaromaticity could lead to island aromaticity. We believe that the Hückel's rule will continue to be a powerful tool in understanding and predicting new all-boron ligands and all-boron building blocks. However, we cannot solely rely on electronic factors in deciphering the relation between the structure and chemical bonding in clusters. We need to have a good geometric fit too. For example, although the cyclic D_{8h}, $^1A_{1g}$ and D_{8h}, $^5A_{1g}$ B_8 structures are doubly aromatic, they are less stable than the doubly aromatic centered D_{7h}, $^3A_2'$ global minimum structure. This occurs because the additional stability to the delocalized density comes from the central atom in the D_{7h}, $^3A_2'$ structure, while in the D_{8h}, $^1A_{1g}$ and D_{8h}, $^5A_{1g}$ B_8 structures the delocalized density at the center of the cluster does not have enough stabilization from the screened boron nuclei. In the B_{10} cluster, the central cavity in the single centered D_{9h} $^1A_1'$ cluster is too big for one boron atom, and as a result, the C_{2h}, ^1A_g structure with two centered boron atoms is more stable. As the size of the cycle increases more and more atoms are more favorably located at the center of the planar or quasi-planar all-boron clusters in the most stable structures.

Pure boron clusters represent today a class of species, which are well understood. We can quite reliably explain, and even predict the structure of small boron clusters, and thus recommend which clusters may have a potential to be new building blocks and ligands. We hope that boron chemistry will experience a renaissance and new materials can be prepared with all-boron clusters as ligands and building blocks.

Acknowledgements

References

[1] N.N. Greenwood, A. Earnshaw, Chemistry of the Elements, second ed., Butterworth-Heinemann, Oxford/Auckland/Boston/Johannesburg/Melbourne/New Delhi, 2001.

[2] F.A. Cotton, G. Wilkinson, C.A. Murillo, M. Bochmann, Advanced Inorganic Chemistry, sixth ed., John Wiley & Sons, New York, 1999.

[3] (a) A. Stock, C. Massanez, Chem. Ber. 45 (1912) 3539;
(b) A. Stock, Hydrides of Boron and Silicon, Cornell University Press, Ithaca, NY, 1933.

[4] W. Dilthey, Z. Angew. Chem. 34 (1921) 596.

[5] W.C. Price, J. Chem. Phys. 15 (1947) 614.

[6] W.C. Price, J. Chem. Phys. 16 (1948) 894.

[7] R.P. Bell, H.C. Longuet-Higgins, Proc. R. Soc. (Lond.) A 183 (1945) 357.

[8] K. Hedberg, V. Schomaker, J. Am. Chem. Soc. 73 (1951) 1482.

[9] W.N. Lipscomb, Boron Hydrides, W.A. Benjamin, New York, 1963.

[10] K.S. Pitzer, J. Am. Chem. Soc. 67 (1945) 1126.

[11] W.H. Eberhardt, B. Crawford, W.N. Lipscomb, J. Chem. Phys. 22 (1954) 989.

[12] G. Allard, Bull. Soc. Chim. Fr. 51 (1932) 1213.

[13] L. Pauling, S. Weinbaum, Z. Kristallogr. 87 (1934) 181.

[14] H.C. Longuet-Higgins, M.deV. Roberts, Proc. R. Soc. (Lond.) 224A (1954) 336.

[15] H.C. Longuet-Higgins, M.deV. Roberts, Proc. R. Soc. (Lond.) 230A (1955) 110.

[16] J.L. Hoard, S. Geller, R.E. Hughes, J. Am. Chem. Soc. 73 (1951) 1892.

[17] W.N. Lipscomb, M.F. Hawthorn, A.R. Pitochelli, J. Am. Chem. Soc. 81 (1959) 5833.

[18] M.F. Hawthorn, A.R. Pitochelli, J. Am. Chem. Soc. 81 (1959) 5519.

[19] J.A. Wunderlich, W.N. Lipscomb, J. Am. Chem. Soc. 82 (1960) 4427.

[20] (a) A. Kaczmarczyk, R.D. Dobrott, W.N. Lipscomb, Proc. Natl. Acad. Sci. U.S.A. 48 (1962) 729;
(b) R.D. Dobrott, W.N. Lipscomb, J. Chem. Phys. 37 (1962) 1779.

[21] F. Klanberg, E.L. Muetterties, Inorg. Chem. 5 (1966) 1955.

[22] F. Klanberg, D.R. Eaton, L.J. Guggenberger, E.L. Muetterties, Inorg. Chem. 6 (1967) 1271.

[23] J.E. Boone, J. Am. Chem. Soc. 86 (1964) 5036.

[24] W.N. Lipscomb, Boron Hydride Chemistry, Academic Press, New York, 1975.

[25] R.E. Dickerson, W.N. Lipscomb, J. Chem. Phys. 27 (1957) 212.

[26] E.D. Jemmis, M.M. Balakrishnarajan, P.D. Pancharatna, Chem. Rev. 102 (2002) 93.

[27] (a) E.D. Jemmis, P.v.R. Schleyer, J. Am. Chem. Soc. 104 (1982) 4781;
(b) E.D. Jemmis, P.N.V. Pavankumar, Proc. Indian Acad. Sci. (Chem. Sci.) 93 (1984) 479;
(c) E.D. Jemmis, J. Am. Chem. Soc. 104 (1982) 7017.

[28] Z.-X. Wang, P.v.R. Schleyer, J. Am. Chem. Soc. 125 (2003) 10484.

[29] D.A. Dixon, D.A. Kleier, T.A. Halgren, J.H. Hall, W.N. Lipscomb, J. Am. Chem. Soc. 99 (1977) 6226.

[30] R.E. Williams, Inorg. Chem. 10 (1971) 210.

[31] K. Wade, Chem. Commun. (1971) 792.

[32] R.J. Gillespie, W.W. Porterfield, K. Wade, Polyhedron 6 (1987) 2129.

[33] E.L. Muetterties (Ed.), Boron Hydride Chemistry, Academic Press, New York, 1975.

[34] W.N. Lipscomb, A.R. Pitochelli, M.F. Hawthorne, J. Am. Chem. Soc. 81 (1959) 5833.

[35] Z. Chen, R.B. King, Chem. Rev. 105 (2005) 3613.

[36] J. Aihara, J. Am. Chem. Soc. 100 (1978) 3339.

[37] R.B. King, D.H. Rouvray, J. Am. Chem. Soc. 99 (1977) 7834.

[38] R.N. Grimes, Carboranes, Academic Press, New York, 1970.

[39] P.v.R. Schleyer, K. Najafian, Inorg. Chem. 37 (1998) 3454.

[40] E.D. Jemmis, E.G. Jayasree, Acc. Chem. Res. 36 (2003) 816.

[41] (a) A.N. Alexandrova, K.A. Birch, A.I. Boldyrev, J. Am. Chem. Soc. 125 (2003) 10786;
(b) A.N. Alexandrova, A.I. Boldyrev, Inorg. Chem. 43 (2004) 3588;
(c) S.K. Ritter, Chem. Eng. News 82 (2004) 09.

[42] (a) J. Namatsu, N. Nakagawa, T. Muranaka, Y. Zenitani, J. Akimitsu, Nature 410 (2001) 63;
(b) C. Day, Phys. Today, (April) (2001) 17;
(c) M. Monteverde, M. Núñez-Regueiro, N. Rogado, K.A. Regan, M.A. Hayward, T. He, S.M. Loureiro, R.J. Cava, Science 292 (6) (2001) 75.

[43] (a) B. Le Guennic, H. Jiao, S. Kahlal, J.-Y. Saillard, J.-F. Halet, S. Ghosh, M. Shang, A.M. Beatty, A.L. Rheingold, T.P. Fehlner, J. Am. Chem. Soc. 126 (2004) 3203;
(b) S. Ghosh, A.M. Beatty, T.P. Fehlner, J. Am. Chem. Soc. 123 (2001) 9188.

[44] W. Siebert (Ed.), Advances in Boron Chemistry, The Royal Society of Chemistry, Cambridge, 1997.

[45] M.F. Hawthorne, J.I. Zink, J.M. Skelton, M.J. Bayer, C. Liu, E. Livshits, R. Baer, D. Neuhauser, Science 303 (2004) 1849.

[46] C.E. Housecroft, Coord. Chem. Rev. 143 (1995) 297.

[47] C.E. Housecroft, Metal Clusters in Chemistry, Wiley/VCH, 1999, p. 10.

[48] Z.L. Wang, Characterization of Nanophase Materials, Wiley/VCH, Weinhein, NY, 2000.

[49] S. Yoshimura, R.P.H. Chang, Supercarbon: Synthesis, Properties, and Applications, Springer, Berlin, Germany, 1998.

[50] Science and Technology of Fullerene Materials: Symposium held November 28–December 2, 1994, Boston, MA, USA, Materials Research Society, Pittsburgh, PA, 1995.

[51] H.O. Pierson, Handbook of Carbon, Graphite, Diamond, and Fullerenes: Properties, Processing, and Applications, Noyes Publications, Park Ridge, NJ, 1993.

[52] G.S. Hammond, V.J. Kuck (Eds.), Fullerenes: Synthesis, Properties, and Chemistry Large Carbon Clusters, American Chemical Society, Washington, DC, 1992.

[53] L. Hanley, S.L. Anderson, J. Phys. Chem. 91 (1987) 5161.

[54] L. Hanley, S.L. Anderson, J. Chem. Phys. 89 (1988) 2848.
[55] L. Hanley, J.L. Whitten, S.L. Anderson, J. Phys. Chem. 92 (1988) 5803.
[56] P.A. Hintz, S.A. Ruatta, S.L. Anderson, J. Chem. Phys. 92 (1990) 292.
[57] S.A. Ruatta, P.A. Hintz, S.L. Anderson, J. Chem. Phys. 94 (1991) 2833.
[58] P.A. Hintz, M.B. Sowa, S.A. Ruatta, S.L. Anderson, J. Chem. Phys. 94 (1991) 6446.
[59] M.B. Sowa-Resat, J. Smolanoff, A. Lapicki, S.L. Anderson, J. Chem. Phys. 106 (1997) 9511.
[60] I. Boustani, Chem. Phys. Lett. 240 (1995) 135.
[61] A. Ricca, C.W. Bauschlicher Jr., Chem. Phys. 208 (1996) 233.
[62] I. Boustani, Phys. Rev. B 55 (1997) 16426.
[63] F.L. Gu, X. Yang, A.C. Tang, H. Jiao, P.v.R. Schleyer, J. Comput. Chem. 19 (1998) 203.
[64] J.E. Fowler, J.M. Ugalde, J. Phys. Chem. A 104 (2000) 397.
[65] S.J. La Placa, P.A. Roland, J.J. Wynne, Chem. Phys. Lett. 190 (1992) 163.
[66] H.-J. Zhai, L.S. Wang, A.N. Alexandrova, A.I. Boldyrev, V.G. Zakrzewski, J. Phys. Chem. A 107 (2003) 9319.
[67] H.-J. Zhai, L.S. Wang, A.N. Alexandrova, A.I. Boldyrev, J. Chem. Phys. A 117 (2002) 7917.
[68] A.N. Alexandrova, A.I. Boldyrev, H.-J. Zhai, L.S. Wang, E. Steiner, P.W. Fowler, J. Phys. Chem. A 107 (2003) 1359.
[69] A.N. Alexandrova, A.I. Boldyrev, H.-J. Zhai, L.S. Wang, J. Phys. Chem. A 108 (2004) 3509.
[70] H.-J. Zhai, A.N. Alexandrova, K.A. Birch, A.I. Boldyrev, L.S. Wang, Angew. Chem. Int. Ed. Engl. 42 (2003) 6004.
[71] H.-J. Zhai, B. Kiran, J. Li, L.S. Wang, Nat. Mater. 2 (2003) 827.
[72] B. Kiran, S. Bulusu, H.-J. Zhai, S. Yoo, X.C. Zeng, L.S. Wang, Proc. Natl. Acad. Sci. USA 102 (2005) 961.
[73] S.-J. Xu, J.M. Nilles, D. Radisic, W.-J. Zheng, S. Stokes, K.H. Bowen, R.C. Becker, I. Boustani, Chem. Phys. Lett. 379 (2003) 282.
[74] D.E. Bergeron, A.W. Castleman Jr., Int. J. Mass Spectrom. 230 (2003) 71.
[75] M. Wyss, E. Riaplov, A. Batalov, J.P. Maier, T. Weber, W. Meyer, P. Rosmus, J. Chem. Phys. 119 (2003) 9703.
[76] P. Cias, M. Araki, A. Denisov, J.P. Maier, J. Chem. Phys. 121 (2004) 6776.
[77] A. Batalov, J. Fulara, I. Shnitko, J.P. Maier, Chem. Phys. Lett. 404 (2005) 315.
[78] A.N. Alexandrova, A.I. Boldyrev, Y.-J. Fu, X. Yang, X.-B. Wang, L.S. Wang, J. Chem. Phys. 121 (2004) 5709.
[79] A.N. Alexandrova, A.I. Boldyrev, J. Chem. Theory Comput. 1 (2005) 566.
[80] R.G. Parr, W. Yang, Density-Functional Theory of Atoms and Molecules, Oxford University Press, Oxford, UK, 1989.
[81] A.D. Becke, J. Chem. Phys. 98 (1993) 5648.
[82] J.P. Perdew, J.A. Chevary, S.H. Vosko, K.A. Jackson, M.R. Pederson, D.J. Singh, C Fiolhais, Phys. Rev. B 46 (1992) 6671.
[83] M.J. Frisch, G.W. Trucks, H.B. Schlegel, G.E. Scuseria, M.A. Robb, J.R. Cheeseman, J.A. Montgomery Jr., T. Vreven, K.N. Kudin, J.C. Burant, J.M. Millam, S.S. Iyengar, J. Tomasi, V. Barone, B. Mennucci, M. Cossi, G. Scalmani, N. Rega, G.A. Petersson, H. Nakatsuji, M. Hada, M. Ehara, K. Toyota, R. Fukuda, J. Hasegawa, M. Ishida, T. Nakajima, Y. Honda, O. Kitao, H. Nakai, M. Klene, X. Li, J.E. Knox, H.P. Hratchian, J.B. Cross, V. Bakken, C. Adamo, J. Jaramillo, R. Gomperts, R.E. Stratmann, O. Yazyev, A.J. Austin, R. Cammi, C. Pomelli, J.W. Ochterski, P.Y. Ayala, K. Morokuma, G.A. Voth, P. Salvador, J.J. Dannenberg, V.G. Zakrzewski, S. Dapprich, A.D. Daniels, M.C. Strain, O. Farkas, D.K. Malick, A.D. Rabuck, K. Raghavachari, J.B. Foresman, J.V. Ortiz, Q. Cui, A.G. Baboul, S. Clifford, J. Cioslowski, B.B. Stefanov, G. Liu, A. Liashenko, P. Piskorz, I. Komaromi, R.L. Martin, D.J. Fox, T. Keith, M.A. Al-Laham, C.Y. Peng, A. Nanayakkara, M. Challacombe, P.M.W. Gill, B. Johnson, W. Chen, M.W. Wong, C. Gonzalez, J.A. Pople, Gaussian 03, Revision C.02, Gaussian, Inc., Wallingford, CT, 2004.
[84] J. Cizek, J. Adv. Chem. Phys. 14 (1969) 35.
[85] P.J. Knowles, C. Hampel, H.-J. Werner, J. Chem. Phys. 99 (1993) 5219.
[86] K. Raghavachari, G.W. Trucks, J.A. Pople, M. Head-Gordon, Chem. Phys. Lett. 157 (1989) 479.
[87] A.D. McLean, G.S. Chandler, J. Chem. Phys. 72 (1980) 5639.
[88] T. Clark, J. Chandrasekhar, G.W. Spitznagel, P.v.R. Schleyer, J. Comput. Chem. 4 (1983) 294.
[89] M.J. Frisch, J.A. Pople, J.S. Binkley, J. Chem. Phys. 80 (1984) 3265.
[90] F. Bernardi, A. Bottini, J.J.W. McDougall, M.A. Robb, H.B. Schlegel, Faraday Symp. Chem. Soc. 19 (1984) 137.
[91] M.J. Frisch, I.N. Ragazos, M.A. Robb, H.B. Schlegel, Chem. Phys. Lett. 189 (1992) 524.
[92] (a) L.S. Cederbaum, J. Phys. B 8 (1975) 290;
(b) W. von Niessen, J. Shirmer, L.S. Cederbaum, Comput. Phys. Rep. 1 (1984) 57.
[93] V.G. Zakrzewski, W. von Niessen, J. Comput. Chem. 14 (1993) 13.
[94] (a) J.V. Ortiz, Int. J. Quant. Chem., Quant. Chem. Symp. 23 (1989) 321;
(b) J.S. Lin, J.V. Ortiz, Chem. Phys. Lett. 171 (1990) 197.
[95] V.G. Zakrzewski, J.V. Ortiz, J.A. Nichols, D. Heryadi, D.L. Yeager, J.T. Golab, Int. J. Quant. Chem. 60 (1996) 29.
[96] R. Bauernshmitt, R. Ahlrichs, Chem. Phys. Lett. 256 (1996) 454.
[97] M.E. Casida, C. Jamorski, K.C. Casida, D.R. Salahub, J. Chem. Phys. 108 (1998) 4439.
[98] A.E. Reed, L.A. Curtiss, F. Weinhold, Chem. Rev. 88 (1988) 899.
[99] E. Aprà, T.L. Windus, T.P. Straatsma, E.J. Bylaska, W. de Jong, S. Hirata, M. Valiev, M. Hackler, L. Pollack, K. Kowalski, R. Harrison, M. Dupuis, D.M.A. Smith, J. Nieplocha, V. Tipparaju, M. Krishnan, A.A. Auer, E. Brown, G. Cisneros, G. Fann, H. Fruchtl, J. Garza, K. Hirao, R. Kendall, J. Nichols, K. Tsemekhman, K. Wolinski, J. Anchell, D. Bernholdt, P. Borowski, T. Clark, D. Clerc, H. Dachsel, M. Deegan, K. Dyall, D. Elwood, E. Glendening, M. Gutowski, A. Hess, J. Jaffe, B. Johnson, J. Ju, R. Kobayashi, R. Kutteh, Z. Lin, R. Littlefield, X. Long, B. Meng, T. Nakajima, S. Niu, M. Rosing, G. Sandrone, M. Stave, H. Taylor, G. Thomas, J. van Lenthe, A. Wong, Z. Zhang, NWChem 4.7, NWChem, A Computational Chemistry Package for Parallel Computers, Version 4.7, Pacific Northwest National Laboratory, Richland, WA 99352-0999, USA, 2005.
[100] G. Schaftenaar, MOLDEN3.4, CAOS/CAMM Center, The Netherlands, 1998.
[101] L.S. Wang, H.-S. Cheng, J. Fan, J. Chem. Phys. 102 (1995) 9480.
[102] L.S. Wang, H. Wu, in: M.A. Duncan (Ed.), Advances in Metal and Semiconductor Clusters. IV. Cluster Materials, JAI Press, Greenwich, CT, 1998, p. 299.
[103] L.S. Wang, X. Li, in: P. Jena, S.N. Khanna, B.K. Rao (Eds.), Clusters and Nanostructure Interfaces, World Scientific, New Jersey, 2000, p. 293.
[104] X. Li, H. Wu, X.B. Wang, L.S. Wang, Phys. Rev. Lett. 81 (1998) 1909.
[105] J. Akola, M. Manninen, H. Hakkinen, U. Landman, X. Li, L.S. Wang, Phys. Rev. B 60 (1999) R11297.
[106] K.P. Huber, G. Herzberg, Molecular Spectra and Molecular Structure. IV. Constants of Diatomic Molecules, Van Nostrand Reinhold, New York, 1979.
[107] A.I. Boldyrev, J. Simons, Periodic Table of Diatomic Molecules, Wiley & Sons, UK, 1997.
[108] P.J. Bruna, J.S. Wright, J. Mol. Struct. Theochem. 210 (1990) 243.
[109] R.A. Whiteside, Ph.D. Thesis, Carnegie Mellon University, Pittsburgh, PA, 1981.
[110] R. Hernandez, J. Simons, J. Chem. Phys. 94 (1991) 2961.
[111] Y.M. Hamrick, R.J. Van Zee, W. Weltner Jr., J. Chem. Phys. 96 (1992) 1767.
[112] S. Li, R.J. Van Zee, W. Weltner Jr., Chem. Phys. Lett. 262 (1996) 298.
[113] R. Hernandez, J. Simons, J. Chem. Phys. 96 (1992) 8251.
[114] K. Sato, N. Kanda, T. Ogata, Y. Kumashiro, Chem. Phys. Lett. 325 (2000) 453.
[115] J.M.L. Martin, J.P. François, R. Gijbels, J. Chem. Phys. 90 (1989) 6469.
[116] A.K. Ray, I.A. Howard, K.M. Kanal, Phys. Rev. B 45 (1992) 14247.
[117] B. Fernández, P. Jorgensen, J. Simons, J. Chem. Phys. 98 (1993) 3060.
[118] H. Reis, M.G. Papadopoulos, I. Boustani, Int. J. Quant. Chem. 78 (2000) 131.
[119] A. Pellegatti, F. Marinelli, M. Roche, D. Maynau, J.P. Malrieu, J. Phys. 48 (1987) 29.
[120] Z.X. Cao, A.M. Tian, G.M. Liang, G.S. Yan, Chin. Chem. Lett. 4 (1993) 75.

[121] Y.M. Hamrick, R.J. Van Zee, W. Weltner Jr., J. Chem. Phys. 95 (1991) 3009.
[122] H. Kato, K. Yamashita, K. Morokuma, Chem. Phys. Lett. 190 (1992) 361.
[123] A. Meden, J. Mavri, M. Bele, S. Pejovnik, J. Phys. Chem. 99 (1995) 4252.
[124] J. Niu, B.K. Rao, P. Jena, J. Chem. Phys. 107 (1997) 132.
[125] V. Bonacic-Koutecky, P. Fantucci, J. Koutecky, Chem. Rev. 91 (1991) 1035.
[126] R. Garcia-Molina, S. Heredia-Avalos, I. Abril, J. Phys.: Condens. Matter 12 (2000) 5519.
[127] I. Boustani, Int. J. Quant. Chem. 52 (1994) 1081.
[128] A. Ricca, C.W. Bauschlicher Jr., J. Chem. Phys. 106 (1997) 2317.
[129] D.N. Bernardo, G.H. Morrison, Surf. Sci. 223 (1989) L913.
[130] A.E. Kuznetsov, A.I. Boldyrev, Struct. Chem. 13 (2002) 141.
[131] B. Averkiev, A.I. Boldyrev, unpublished results.
[132] (a) P.v.R. Schleyer, C. Maerker, A. Dransfeld, H. Jiao, N.J.R.v. Hommes, J. Am. Chem. Soc. 118 (1996) 6317;
(b) Z. Chen, C.S. Wannere, C. Corminboeuf, R. Puchta, P.V.R. Schleyer, Chem. Rev. 105 (2005) 3842.
[133] A.I. Boldyrev, L.S. Wang, Chem. Rev. 105 (2005) 3716.
[134] J.M.L. Martin, J.P. François, R. Gijbels, Chem. Phys. Lett. 189 (1992) 529.
[135] A.N. Alexandrova, A.I. Boldyrev, unpublished results.
[136] H. Reis, M.G. Papadopoulos, J. Comput. Chem. 20 (1999) 679.
[137] (a) H.W. Jin, Q.S. Li, Phys. Chem. Chem. Phys. 5 (2003) 1110;
(b) Q.S. Li, H.W. Jin, J. Chin. Chem. Soc. 50 (2003) 1115.
[138] C. Gillery, R. Linguerri, P. Rosmus, J.P. Maier, Z. Phys. Chem. 219 (2005) 467.
[139] A. Abdurahman, A. Shukla, G. Seifert, Phys. Rev. B 66 (2002) 155423.
[140] H. Kato, E. Tanaka, J. Comput. Chem. 12 (1991) 1097.
[141] R. Linguerri, I. Navizet, P. Rosmus, S. Carter, J.P. Maier, J. Chem. Phys. 122 (2005) 034301.
[142] M. Zhou, Q. Xu, Z.-X. Wang, P.v.R. Schleyer, J. Am. Chem. Soc. 124 (2002) 14854.
[143] J. Juselius, M. Straka, D. Sundholm, J. Phys. Chem. A 105 (2001) 9939.
[144] X. Li, A.E. Kuznetsov, H.F. Zhang, A.I. Boldyrev, L.S. Wang, Science 291 (2001) 859.
[145] Q.S. Li, H.W. Jin, J. Phys. Chem. A 106 (2002) 7042.
[146] Q.S. Li, Q. Jin, J. Phys. Chem. A 108 (2004) 855.
[147] S. Guerini, P. Piquini, Eur. Phys. J. D 16 (2001) 17.
[148] Q.S. Li, Q. Jin, Q. Luo, A.C. Tang, J.K. Yu, H.X. Zhang, Int. J. Quant. Chem. 94 (2003) 269.
[149] J. Ma, Z. Li, K. Fan, M. Zhou, Chem. Phys. Lett. 372 (2003) 708.
[150] S. Guerini, P. Piquini, Int. J. Quant. Chem. 95 (2003) 329.
[151] R.W.A. Havenith, P.W. Fowler, E. Steiner, Chem. Eur. J. 8 (2002) 1068.
[152] E. Steiner, P.W. Fowler, J. Phys. Chem. A 105 (2001) 9553.
[153] E. Steiner, P.W. Fowler, R.W.A. Havenith, J. Phys. Chem. A 106 (2002) 7048.
[154] A.N. Alexandrova, A.I. Boldyrev, H.-J. Zhai, L.S. Wang, J. Chem. Phys. 122 (2005) 054313.
[155] Q.S. Li, Q. Jin, J. Phys. Chem. A 107 (2003) 7869.
[156] R.B. King, I. Silaghi-Dumitrescu, A. Kun, Inorg. Chem. 40 (2001) 2450.
[157] Q.S. Li, L.F. Gong, Z.M. Gao, Chem. Phys. Lett. 390 (2004) 220.
[158] P.-l. Cao, W. Zhao, B.-x. Li, B. Song, X.-y. Zhou, J. Phys.: Condens. Matter 13 (2001) 5065.
[159] Q.S. Li, L.F. Gong, J. Phys. Chem. A 108 (2004) 4322.
[160] A.N. Alexandrova, E. Koyle, A.I. Boldyrev, J. Mol. Model., in press.
[161] H.-J. Zhai, L.S. Wang, D.Yu. Zubarev, A.I. Boldyrev, J. Phys. Chem. A 110 (2006) 1689.
[162] B. Kiran, X. Li, H.-J. Zhai, L.-F. Cui, L.S. Wang, Angew. Chem. Int. Ed. 43 (2004) 2125.
[163] X. Li, B. Kiran, L.S. Wang, J. Phys. Chem. A 109 (2005) 4366.
[164] Q.S. Li, Y. Zhao, W. Xu, N. Li, Int. J. Quant. Chem. 101 (2005) 219.
[165] A.N. Alexandrova, H.-J. Zhai, L.S. Wang, A.I. Boldyrev, Inorg. Chem. 43 (2004) 3552.
[166] S.D. Li, J.C. Guo, C.Q. Miao, G.M. Ren, Angew. Chem. Int. Ed. 44 (2005) 2158.
[167] V.I. Minkin, R.M. Minyaev, Mendeleev Commun. 14 (2004) 43.
[168] R.M. Minyaev, T.N. Gribanova, A.G. Starikov, V.I. Minkin, Mendeleev Commun. 11 (2001) 213.
[169] D.Yu. Zubarev, A.I. Boldyrev, J. Comput. Chem., in press.
[170] R. Kawai, J.H. Weare, Chem. Phys. Lett. 191 (1992) 311.
[171] F.L. Gu, X. Yang, A.C. Tang, H.J. Jiao, P.v.R. Schleyer, J. Comput. Chem. 19 (1998) 203.
[172] J.E. Fowler, J.M. Ugalde, J. Phys. Chem. A 104 (2000) 397.
[173] J.-i. Aihara, J. Phys. Chem. A 105 (2001) 5486.
[174] S.K. Ritter, Chem. Eng. News 82 (9) (2004) 28.
[175] M.A.L. Marques, S. Botti, J. Chem. Phys. 123 (2005) 014310.
[176] D.J. Wales, M.A. Miller, T.R. Walsh, Nature 394 (1998) 758.
[177] S. Yoo, X.C. Zeng, X. Zhu, J. Bai, J. Am. Chem. Soc. 125 (2003) 13318.
[178] H. Prinzbach, A. Weiler, P. Landenberger, F. Wahl, J. Worth, L.T. Scott, M. Gelmont, D. Olevano, B. Issendorff, Nature 407 (2000) 60.
[179] S. Yang, K.J. Taylor, M.J. Craycraft, J. Conceicao, C.L. Pettiette, O. Cheshnovsky, R.E. Smalley, Chem. Phys. Lett. 144 (1988) 431.
[180] G.v. Heldon, P.R. Kemper, N.G. Gotts, M.T. Bowers, Science 259 (1993) 1300.
[181] H. Handschuh, G. Gantefor, B. Kessler, P.S. Bechthold, W. Eberhardt, Phys. Rev. Lett. 74 (1995) 1095.
[182] S. Chacko, D.G. Kanhere, I. Boustani, Phys. Rev. B 68 (2003) 035414.
[183] I. Boustani, A. Quandt, Europhys. Lett. 39 (1997) 527.
[184] I. Boustani, A. Quandt, E. Hernandez, A. Rubio, J. Chem. Phys. 110 (1999) 3176.
[185] A. Gindulyte, N. Krishnamachari, W.N. Lipscomb, L. Massa, Inorg. Chem. 37 (1998) 6546.
[186] A. Quandt, I. Boustani, ChemPhysChem 6 (2005) 2001.
[187] J.-i. Aihara, H. Kanno, T. Ishida, J. Am. Chem. Soc. 127 (2005) 13324.